Fundamental Flux Enhancement Modelling of Membrane Microfiltration

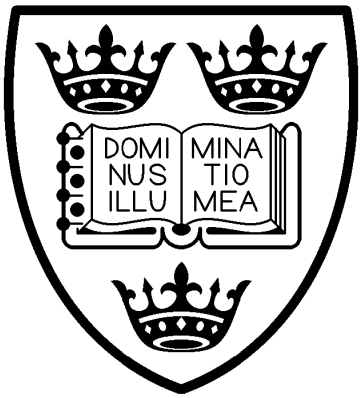

Mark Valentine

Hertford College, Oxford

Trinity Term, 2011

A thesis submitted for the degree of

Doctor of Philosophy

Department of Engineering Science

University of Oxford

Abstract

Membrane filtration is used in a variety of industries, including water treatment and the food industry. Membrane systems include microfiltration and reverse osmosis processes. Membranes used in reverse osmosis are nonporous or pores at 0.2-2 A. This work will focus on mechanical microfiltration. These filtration systems suffer from an accumulation of the rejected material near the membrane surface. This causes additional resistance to the flow through the membrane (flux), resulting in a decline in the performance of the system.

Sparging gas bubbles into the mixture has been shown to improve performance. The flow field promotes the transport of material away from the membrane surface and into the bulk. The goal is to predict the sparging that will achieve the maximum flux. Existing flux prediction models often assume steady shear at the membrane surface but in bubbling regimes the shear stresses are unsteady.

In this thesis a model is developed to calculate the flux based not solely on shear but on the behaviour and resistance of suspended particles in a gas-liquid flow field. The bubble shape and flow field is calculated using computation fluid dynamics (CFD). The flow around a bubble in gap between two parallel flat sheet membranes is investigated. The calculated bubble shape correlates well with the results seen in experiments. The bubble rise velocity with respect to gap width is shown to transition between that expected in the literature for extended flow for large gap widths and that for a two dimensional case for smaller gap widths. The transitional region however, does not behave as may be expected. The rise velocity does not monotonically decrease as the gap width is reduced.

The particle concentration is found by the solution of the convection-diffusion equation, where the convection velocity terms are given by the results of the CFD calculation. The permeate flux is then calculated using a resistance model giving the enhancement due to the bubble. The model is also applied to single phase crossflow. As the shear stresses are steady in this single-phase flow regime, established membrane shear linked mass-transfer coefficient methods can be employed. Good agreement is found between the model and theory.

The flux results obtained when the model is applied to the flow around the bubble show a peak in performance with respect to the gap between the membranes for a given bubble volume. The optimal flux enhancement is found to correlate well with the bubble size compared to the flow area. The results show a bubble width of around 60% of the flow width provides the best flux performance.

for my Mother and Father

Acknowledgements

Firstly and most importantly I would like to thank my supervisors Prof. Cui and Dr Field for their excellent technical and practical advice. Especially to Dr Field for becoming my supervisor whilst I was already underway.

I also must thank the Engineering and Physical Sciences Research Council (EPSRC) for the doctoral training account that provided the funds to make this work possible.

I would like to thank Hertford College for their pastoral support and its middle common room for providing many social distractions. Thanks also to the Hertford College Boat Club for keeping me active and giving me a healthy diversion from work.

Within the Department of Engineering Science I would also like to thank Anja Drews and Alex Lubansky for their technical support and the willingness to give up time to help.

Finally thanks to my family for their constant support.

Contents

Abstract **i**

Acknowledgements **iii**

List of Figures **vii**

Nomenclature **xv**

1 Introduction **1**

1.1 Membrane Bioreactors 1

1.1.1 Membrane Types 2

1.1.2 Submerged and Sidestream Comparison 4

1.1.3 Airlift 4

1.2 Concentration Polarisation Model 5

1.3 Permeate flux prediction in membrane separation 8

1.3.1 Mass transfer coefficient 8

1.3.2 Osmotic Pressure 10

1.3.3 Resistance in series model 12

1.3.4 Resistance of suspended particles 14

1.3.5 Fouling and Concentration Polarisation Control Methods 17

1.4 Gas–Liquid Two–Phase Flow 18

1.4.1 Bubble Behaviour in confined space 18

1.5 Computational Fluid Dynamics 20

1.5.1 Eulerian Method 21

1.5.2 Lagrangian Method 21

1.5.3 Turbulence Modelling 21

1.6 Control of Bubble Behaviour in Fluidised Beds 22

1.7 Thesis Outline 22

2 Development of Particle - Flux Models **26**

2.1 Introduction 26

2.2 Simplifications and Assumptions 27

2.3 Convection-Diffusion Equation 27

2.4 Diffusivity . . . 27
2.5 Numerical Method . . . 28
2.5.1 Time Step Convergence . . . 29
2.5.2 Numerical Dispersion . . . 29
2.5.3 Mesh Refinement Near Membrane . . . 30
2.5.4 General Solution . . . 31
2.5.5 Boundary Conditions . . . 31
2.6 Flux Resistance Model . . . 32
2.6.1 Carmen-Kozeny Equation . . . 32
2.7 Cake Layer Resistance . . . 34
2.8 Converging The Solution . . . 34
2.9 Results - Single Phase Crossflow . . . 35
2.9.1 Crossflow Velocity . . . 37
2.9.2 Transmembrane Pressure . . . 37
2.9.3 Concentration Polarisation . . . 46
2.9.4 Particle Size . . . 47
2.9.5 Convergence . . . 53
2.10 Summary . . . 55

3 CFD Modelling of Gas-Liquid Flow Between Two Parallel Flat Plates 58

3.1 Introduction . . . 58
3.2 Governing Equations . . . 61
3.3 Multiphase Volume Of Fluid (VOF) Method . . . 62
3.4 Surface Tension . . . 63
3.5 Boundary Conditions . . . 63
3.6 Initial Conditions . . . 64
3.7 2D Results – Bubble Dynamics . . . 64
3.7.1 Bubble Shape and Rise Velocity . . . 64
3.7.2 Bubble Interaction . . . 69
3.7.3 Sparging Frequency . . . 70
3.8 2D Results – Induced Flow Against Membrane . . . 77
3.8.1 Bubble Shape . . . 77

3.8.2 Wall Shear . . . 77
3.9 3D Results . . . 85
3.9.1 Convergence . . . 85
3.9.2 Bubble Shape . . . 85
3.9.3 Wall Shear . . . 91
3.9.4 Bubble Rise Velocity . . . 96
3.10 Summary . . . 102

4 Flux Enhancement for Bubbling Membrane Filtration 103
4.1 Introduction . . . 103
4.2 Particle Concentration . . . 104
4.3 Flux . . . 104
4.4 Flux Optimisation Design . . . 118

5 Conclusions and Future Work 122
5.1 Conclusions . . . 122
5.1.1 Particle and Flux Model . . . 122
5.1.2 Gas-Liquid Flow Between Two Parallel Flat Sheets . . . 122
5.1.3 Flux Enhancement for Bubbling Membrane Filtration . . . 124
5.2 Future Work . . . 124

References 126

List of Figures

1.1 Submerged (a) and sidestream (b) configuration of a membrane bioreactor. Taken from Zhao [1]. 3

1.2 Kubota Submerged Flat Sheet Membrane Bioreactor with Gas Sparging [2]. . 5

1.3 Flow induced between a sparged and non-sparged liquid plane. 6

1.4 Schematic of concentration polarization boundary layer. Adapted from Baker [3]. 7

1.5 Schematic of flow regimes about a slug bubble. In this image three distinct zones are classified from top to bottom: falling film between the bubble and the membrane, wake just below the bubble and liquid slug in the region between the bubbles. Taken from Ghosh [4]. 11

1.6 This figure shows the result of an increase in resistance with respect to trans-membrane pressure for dead-end filtration. In the low TMP region the flux is proportional to the applied pressure, indicating membrane resistance only, with no significant additional resistance. As the TMP is increased the flux does not increase proportionately indicating additional resistance. The resistance is directly proportional to applied pressure as is the dominant resistance. The onset flux at which significant additional resistance forms is the critical flux. At high pressure regions a cake layer has formed which grows proportionately with the applied TMP. This results in no additional flux in this regime. This is known as the limiting flux. Enhancement methods are concerned with increasing this limiting flux. 13

1.7 The dimensionless pressure drop with respect to particle volume fraction in the cake layer. 16

1.8 Experimental data [5] for fixed flux TMP with respect to time. 17

1.9 Flow regimes with respect to increasing gas volume fraction. Taken from Whalley [6]. 19

1.10 Frequency control method for bubbling conditions which have highly volatile responses in the time domain. 23

1.11 Submerged Flat Sheet Membrane Bioreactor with Gas Sparging schematic [7]. The flow to be modelled is gas-liquid between the parallel membranes. 24

2.1 Illustration of the different particle resistance regimes near the membrane. From the bulk region there is a concentration polarisation build up to the membrane, where a cake layer of maximal concentration forms. The resistance of the boundary layer and the cake layer are calculated as the change with time and are added to the membrane resistance. 33
2.2 This figure shows the build up in concentration from the inlet at the top. . . 36
2.3 Values used to obtain results, except where stated. 37
2.4 The variation in flux with respect to the mean crossflow velocity is shown. The results show the comparison between the two flux calculation methods. To attain steady state the model is run until negligible changes in flux are seen, as shown in Figure 2.19 38
2.5 Flux with respect to transmembrane pressure for each method. The three regions of constant membrane resistance only, critical flux onset and limiting flux are well captured. 39
2.6 Concentration polarisation boundary layer with respect to transmembrane pressure. The concentration is given as the particle volume fraction, the depth is in mm. When the transmembrane pressure exceeds 40kPa the change in the boundary layer is negligible, hence the curves for these higher pressures appear overlaid and indistinct. 40
2.7 Boundary layer resistance with respect to transmembrane pressure. 42
2.8 The resistance gradient of the boundary layer with respect to transmembrane pressure. 43
2.9 Cake layer resistance with respect to transmembrane pressure. 44
2.10 The resistance gradient of the cake layer with respect to transmembrane pressure. 45
2.11 Gradient of flux with respect to transmembrane pressure. Note the zeroes indicating stationary points. 46
2.12 This graph shows the steady state particle concentration increase towards the membrane (depth 4mm), half way up the membrane. This illustrates the concentration polarisation. 48
2.13 Boundary layer development with respect to the simulation time. 49
2.14 Steady state flux variation with respect to particle size. Excellent correlation is found in the ultrafiltration regime, deteriorating for larger particles. 50

2.15 Boundary layer development for different particle sizes, no cake layer development. 51
2.16 When the cake layer has formed the boundary layer development for different particle diameters has a different nature. It undergoes a thickening after the max concentration has been reached. It can be seen that the smaller particle sizes have a higher concentration in the boundary layer. 52
2.17 Resistance of the membrane, the boundary and cake layers with respect to particle size. 53
2.18 The convergence of the results are checked against the mesh. As the cell size decreases and the number of cells increases the flux converges to an asymptotic value. 54
2.19 The decline in flux with respect to time. Here the flux reaches steady state after 6 seconds with the flux settling at 19.4 LMH. Although for low flux high resistance calculations the steady state flux is not found so quickly. Hence in the subsequent multiphase chapter the flux enhancement is used as this describes both the increase in performance and converges more readily. 56
3.1 Schematic showing the modelled flows in 2D. The shear calculation on the left, which is a plane through the centre of the bubble shown right which is used for the dynamics calculation. The modelled domain is width x height, 12mm x 300mm and 100mm x 200mm, for the side and front calculation respectively. 59
3.2 Schematic of a single bubble slugged between two flat sheet membranes modelled in 3D. The permeate flux is indicated. Presence of particles shown for illustration purposes. 60
3.3 Motion of diameter, $d_e = 14.1$mm, bubble up the bed at time increments of 0.1 seconds. As the bubble is accelerating vertically, its Reynolds number will increase; the associated transition in bubble shape is well captured. The bubble has a steady state rise velocity of $u_b = 0.196$m/s, giving a Reynolds number of $Re = 2772$. 65
3.4 Image of single spherical cap bubble moving in a narrow gap between two parallel plates. Taken from Essemiani et. al. [8]. 66
3.5 Chart showing bubble characteristics with respect to the dimensionless Eotvos, Morton and Reynolds numbers. Taken from Clift et. al. [9]. 68

3.6 Method for determining the bubble rise velocity up the bed. Bubble equivalent diameter, $d_e = 33$mm. 69
3.7 Comparison of simulated rise velocities with experimental results. 70
3.8 The interaction of two vertically inline bubbles of equivalent diameter, $d_e =$ 14.1mm. The lower bubble is drawn into the low pressure wake behind the lead bubble, whereupon they coalesce into one larger bubble. 71
3.9 Smaller bubbles torn from main bubble with Eotvos number, $Eo = 61.2$. Note how these bubbles encircle and describe the wake region below the main bubble. 72
3.10 The bubble nose and tail paths up the centre line of the bed are plotted at a sparging frequency of 5 bubbles per second. The effects of the bubble interactions appear to reach a steady state. The attraction of a given bubble to its lead bubble is matched by that bubbles own attraction to its leader. The steady state bubble rise velocity exceeds the single bubble rise velocity. 73
3.11 Bubble nose and tail positions with respect to time at a sparging frequency of 2.5 bubbles per second. 74
3.12 Bubble nose and tail positions with respect to time in a taller bed (400mm) at a sparging frequency of 5 bubbles per second. 75
3.13 These images show the progress of bubbles at time steps of 0.1 seconds up a taller (400mm) bed at a sparging frequency of 5 bubbles per second. The shedding of smaller bubbles from the main bubbles leads to considerable instability in the phases. This is difficult to control and might require a period where no gas is introduced to return the bed to stable conditions. 76
3.14 Weak interaction between horizontally aligned bubbles. 77
3.15 Bubble shape for increasing gas volumes. The length of the bubbles relative to the channel width (12mm) are 1.25, 2.08, 3.75 and 7.08 respectively. 78
3.16 The pathlines of the liquid entering the top of the domain are shown for each bubble size at a given time. 79
3.17 Shear profiles for the different bubble lengths of 15, 25, 45 and 85 mm respectively. In the main bubble region all profiles share a smooth increase in shear, directly corresponding to the thinning of the film. In the wake region, the mean shear decreases in the absence of the bubble. However, considerable local fluctuations in the flow yield oscillations in shear at much higher frequency. 81

3.18 Oscillations in the bubble tail shown at a 0.12 second time increment. Note how the flow travels in a wave pattern down the domain. Also we see the alternation in which side of the film penetrates the central region most, this results in the downward motion of a given wake peak. 82
3.19 Shear profile as may been seen in a chain of bubbles with the same gas volume. If the bubbles are considered to be acting independently the shear profile from one bubble may be used to build up the complete picture. 83
3.20 Measured response at a point to a passing bubble using the electrochemical method for shear measurement. Taken from Zhang [10, 11]. 84
3.21 Grid convergence for the rise velocity of a 3.075 mL bubble. Domain width $X = 80$mm, height $Y = 120$mm and gap $Z = 8$mm. 86
3.22 Bubble volume, $V = 3.075$mL. Membrane width $X = 80$mm, height $Y = 120$mm and gap $Z = 8$mm. 87
3.23 The shape factor indicates how similar the bubble shape is to a hemisphere or hemicylcinder. It is the ratio of the diameter of a perfect hemisphere or hemicylinder to the calculated bubble diameter. Where the ratio of bubble depth to gap depth is small, the shape is similar to a hemisphere. When the bubble depth is greater than 0.9 of the gap depth, a hemicylinder is a much better approximation of the shape. 89
3.24 This figure indicates the strong correlation between the width and depth of the bubble (the aspect ratio) against the bubble depth to gap depth ratio. . . 90
3.25 Bubble shape in x-y plane by gap depth for gas volumes of 3.075mL and 7.032 mL. 91
3.26 Bubble shape in y-z plane by gap depth for gas volumes of 3.075mL and 7.032 mL. The influence of gap width on bubble shape for a given gas volume. From left to right the gap widths are, 80mm, 40mm, 28mm, 20mm, 16mm, 12mm, 10mm, 9mm, 8mm respectively. Note the limiting minimum of the liquid film between the membrane and the bubble. 92
3.27 Bubble shape in x-z plane by gap width for gas volumes of 3.075mL and 7.032 mL. 92

3.28 The mean shear magnitude increasing with the reduction of the gap. The mean shear magnitude is plotted, instead of maximum shear, as this is more representative of the predicted flux enhancement using shear based methods. 93

3.29 The flow of the liquid phase around the 3.075 mL bubble in a 8mm gap, the black line shows the position of the bubble. The boundary condition at the top is an inlet defined at the velocity found to hold the bubble stationary (the bubble rise velocity). This is in the central plane parallel to the membrane. There are regions of upward flow in the recirculatory regions of the bubble and the wake. However, the main feature is the acceleration of the flow to the side of the bubble caused by the constriction of flow area by the bubble. 94

3.30 The shear on the membrane due to the 3.075 mL bubble in a 8mm gap, the black line shows the position of the bubble. There are high shear regions adjacent to the bubble caused by the small film between bubble and wall. There is also increased shear in the wake region below the bubble. 95

3.31 The bubble rise velocity for each bubble volume for a given gap depth. Each bubble shares three flow types. For larger gaps the bubble is largely unconstrained by the walls so has a higher velocity. As the gap is reduced the drag on the walls creates a reduction in the rise velocity. However, as the film region is formed and is largely constant there appears an increase in bubble velocity. The shape of the bubble is streamlined by the constriction. Further gap reduction brings a decrease in velocity as the width of the bubble becomes significant to the side walls resulting in additional drag as the flow is no longer free in that direction. 97

3.32 The bubble rise velocity is given dimensionless form for the gap depth Z. There is good correlation between this and the aspect ratio of the flow area. The value $Z/X = 1$ represents a square flow region. For the flow regions with small depth, Z, the correlation is less clear as in this region the size of the bubble in the x direction becomes more significant. 98

3.33 The top lines are the unconstrained dimensionless rise velocities for each bubble volume. The bottom line is the dimensionless rise velocity for a 2-dimensional simulation [12]. The data shows the transition between the two flow regimes and which is more significant. When the width of the bubble is small compared to the domain width, the velocity is similar to the inconstrained case. However, as the relative bubble width increases the 2 dimensional approximation is more representative. 100

3.34 The dimensionless velocity compared to the sphericity of the bubble shape. This indicates the correlation between bubble shape and the region where the bubble has a peak in velocity, in the region where the ratio is around 1.7. . . 101

4.1 Particle volume fraction on the membrane in the presence a 3.075mL bubble in a 8mm gap, the black line shows the position of the bubble. Transmembrane pressure, $TMP = 100kPa$. Particle diameter $d_p = 0.2\mu m$. Clean water resistance $R_m = 2.5\text{x}10^{12}m^{-1}$. Bulk concentration $c_b = 15g/L$ 105

4.2 Particle volume fraction perpendicular to membrane within 10 microns in the presence a 3.075mL bubble in a 8mm gap, the black line shows the position of the bubble. Transmembrane pressure, $TMP = 100kPa$. Particle diameter $d_p = 0.2\mu m$. Clean water resistance $R_m = 2.5\text{x}10^{12}m^{-1}$. Bulk concentration $c_b = 15g/L$ 106

4.3 The flux through the membrane. Transmembrane pressure, $TMP = 100kPa$. Particle diameter $d_p = 0.2\mu m$. Clean water resistance $R_m = 2.5\text{x}10^{12}m^{-1}$. Bulk concentration $c_b = 15g/L$. High flux regions include the bubble film and wake, whilst the region where particles are deposited to the side as they pass the bubble suffers from low flux as a result. 107

4.4 Convergence of the flux enhancement for the 3.075mL bubble in a 8 mm gap. 108

4.5 The flux enhancement for each bubble volume with respect to gap. The three larger bubbles suffer a reduction in flux as the bubble size compared to the flow area becomes too large and causes flow constriction and particle build up. When the bubble size is smaller the flux increases with shear as would be expected. 109

4.6 Particle concentration at the membrane surface with a 8mm gap in the presence a 7.035mL bubble, the black line shows the position of the bubble. Note the extra build up of particles by the side wall due to the constriction of the bubble, resulting in reduced flux. 111
4.7 Particle concentration at the membrane surface with a 12mm gap in the presence a 7.035mL bubble, the black line shows the position of the bubble. . . . 112
4.8 In the low shear region, where the bubble width is sufficiently small compare to the flow width, there is strong correlation with flux. However, in the higher mean shear region, the flow constriction become more significant and there is no correlation. 113
4.9 The particle concentration on the membrane for a 3.075 mL bubble by gap depth. 114
4.10 The particle concentration on the membrane for a 7.032 mL bubble by gap depth. 115
4.11 The flux enhancement (%) through the membrane for a 3.075 mL bubble by gap depth. 116
4.12 The flux enhancement (%) through the membrane for a 7.032 mL bubble by gap depth. 117
4.13 For each bubble volume, the peak in flux enhancement is grouped around the region where the bubble width is 60% of the flow width (b_x/X). Experimental results for flat sheet filtration focus on bubble volume and sparging frequency without recording the bubble width. As such no experimental confirmation of this result currently exists. 118
4.14 Notable flux enhancement only occurs, for each bubble volume, after the depth of the bubble exceeds 85% of the gap (b_z/z). 119
4.15 A strong correlation occurs between the peaks in flux and the region where the product of the relative bubble depths and widths, $\frac{b_x b_z}{XZ}$, is 55%. 120

Nomenclature

α	particle volume fraction
α_{cake}	cake layer volume fraction
α_G	volume fraction of the gas phase
α_L	volume fraction of the liquid phase
$\bar{v}(0)$	mean inlet velocity in y
Δp	transmembrane pressure
Δt	time step
Δx	cell width in x-direction
Δy	cell width in y-direction
Δz	cell width in z-direction
δ	concentration polarisation boundary layer thickness
$\Delta\Pi$	osmotic pressure
δ_{cake}	cake layer thickness
ϵ	voidage
γ	shear rate
κ	curvature of the interface between phases
λ	dimensionless z
μ	permeate viscosity
$\overline{\gamma}$	mean shear rate
ρ	permeate density
ρ_p	particle density
σ	surface tension
$\underline{\underline{\tau}}$	stress tensor

$\underline{v}$	velocity vector
a	particle radius
b_x	calculated bubble width in x-direction
b_z	calculated bubble width in z-direction
c	particle concentration
c_b	bulk concentration
c_{cake}	cake layer concentration
c_p	permeate concentration
c_w	wall concentration
D	diffusion coefficient
d_e	equivalent spherical diameter
d_h	hydraulic diameter
d_p	particle diameter
d_t	capillary diameter
d_x	cylindrical equivalent diameter
g	gravitational acceleration
i	counter in x-direction
J	flux through the membrane
j	counter in y-direction
k	counter in z-direction
k	mass transfer coefficient
L	flow length
l_b	bubble length
N	number of capillaries per unit area

n	time counter
P	number of nodes in z-direction
p	fluid pressure
p_{bl}	pressure drop in the concentration polarisation boundary layer
Q	volumetric flow rate
R_{bl}	boundary layer resistance
R_{cake}	cake layer resistance
R_f	internal membrane fouling
R_m	membrane resistance
Re	Reynolds Number
Sc	SchmidtNumber
Sh	Sherwood Number
T	temperature
t	time
u	flow velocity in the x-direction
u_b	bubble rise velocity
V	bubble gas volume
v	flow velocity in the y-direction
w	flow velocity in the z-direction
X	width of the flat sheet membranes
x	horizontal direction perpendicular to gravity and parallel to membrane
Y	height of the flat sheet membranes
y	vertical direction parallel to gravitational acceleration membrane
Z	gap width between the two flat sheet membranes
z	direction perpendicular to membrane

1 Introduction

1.1 Membrane Bioreactors

One of the principal applications for membrane filtration is in the treatment of water using Membrane Bioreactors (MBR). Wastewater treatment includes physical, chemical and biological methods. Physical methods include clarification (sedimentation), where gravitational action on suspended solids causes the separation between clarified liquid and heavier solids, and filtration where wastewater is passed through a separating medium. Biological methods employ microorganisms (bacteria) which help convert the waste into useful end products. This can occur aerobically or anaerobically. Aerobic systems have higher energy costs in adding the gas, but aid bacterial growth rate. Membrane bioreactors combine biological methods with physical (membrane filtration). This has the advantage of combining the benefits of the microorganisms in the bioreactor with the separating membrane which can be more effective than clarifiers. The aerobic membrane bioreactors bubbling has been shown to enhance the filtration properties when the membrane is submerged in the bioreactor. The bubbling satisfies both aeration requirements and aids fouling reduction. However, control of this method requires quantitative work to optimise the design to increase efficiency and save energy costs.

Membrane bioreactors suffer from a reduction in permeate flux due to the influence of the separated material at the membrane surface [13, 14]. The are two mechanisms to consider, concentration polarisation and fouling. Fouling is the process where the separated material interferes with the filtration properties of the membrane, changing its charecteristics by, for example, pore blocking which causes a reduction in flux. Concentration polarisation is the difference in concentration between the permeate and feed side. In this work concentration polarisation refers to the build up of the particle phase between the bulk and the membrane. This causes an increase in resistance due to the drag the particle phase exerts on the flow towards the membrane. To maintain a given flux therefore requires a higher applied pressure across the membrane which increases the energy demand of the system. Gas-liquid two-phase flow at the membrane surface has been shown to reduce the loss of flux due to these impediments [15, 16]. The induced secondary flow disrupts the concentration polarisation boundary layer and fouling. Other methods of fouling control include using spacers to promote heat and mass transfer due to mixing as the liquid flows around them [17, 18]. Changing

the direction of applied pressure by backwashing and pulsatile flow creates fluctuations which disrupt the concentration polarisation, aiding flux.

Methods to explain the hydrodynamic effect of the bubbling include experimental, numerical, and theoretical. Computational Fluid Dynamics (CFD) provides a rigorous numerical top down method using the governing equations for the flow. This enables the collection of quantitative data which informs the system design. The key properties to be measured from the bubbling are the shear at the membrane surface and the flow field around the bubble. Difficulties in using a shear based method include connecting the flow conditions to the flux and correlating this with experimental data. The resultant wall shear calculated by this method has been linked to the flux by use of the mass transfer to heat transfer analogy.

1.1.1 Membrane Types

Membranes can be classed by their geometry, operating method and the material they are separating. The principal membrane shapes are flat-sheet plate and frame, and hollow fibre, employing planar and cylindrical geometries respectively. Judd [19] compares flat sheet and hollow fibre types of submerged membrane bioreactors. The hydrodynamic conditions are less easily controlled in hollow fibre systems which leads to more fouling compared to flat sheet membranes. The Kubota flat sheet membranes are more expensive and cannot be backflushed, requiring low transmembrane pressure to stay below the critical flux [19]. The backflushing of the hollow fibre membranes requires 25% of the product water. Flat sheets can also be wound into cylindrical shapes creating spiral–wound membranes, but this type is not used for waste water treatment.

Membranes are also classified by the size of material they are separating. Microfiltration membranes are used to separate relatively large particles using pore sizes of 80–10,000 nm. Nanofiltration membranes separate solutes of diameter 5–100 nm. These smaller particles diffuse away from the membrane surface more slowly resulting in higher concentration build-up at the wall, making these membranes more susceptible to concentration polarisation. Unlike nanofiltration which only rejects multivalent ions, reverse osmosis membranes can reject both mono-valent and mulitvalent ions. The applied TMP must exceed the osmotic pressure resulting from the concentration imbalance [20, 3].

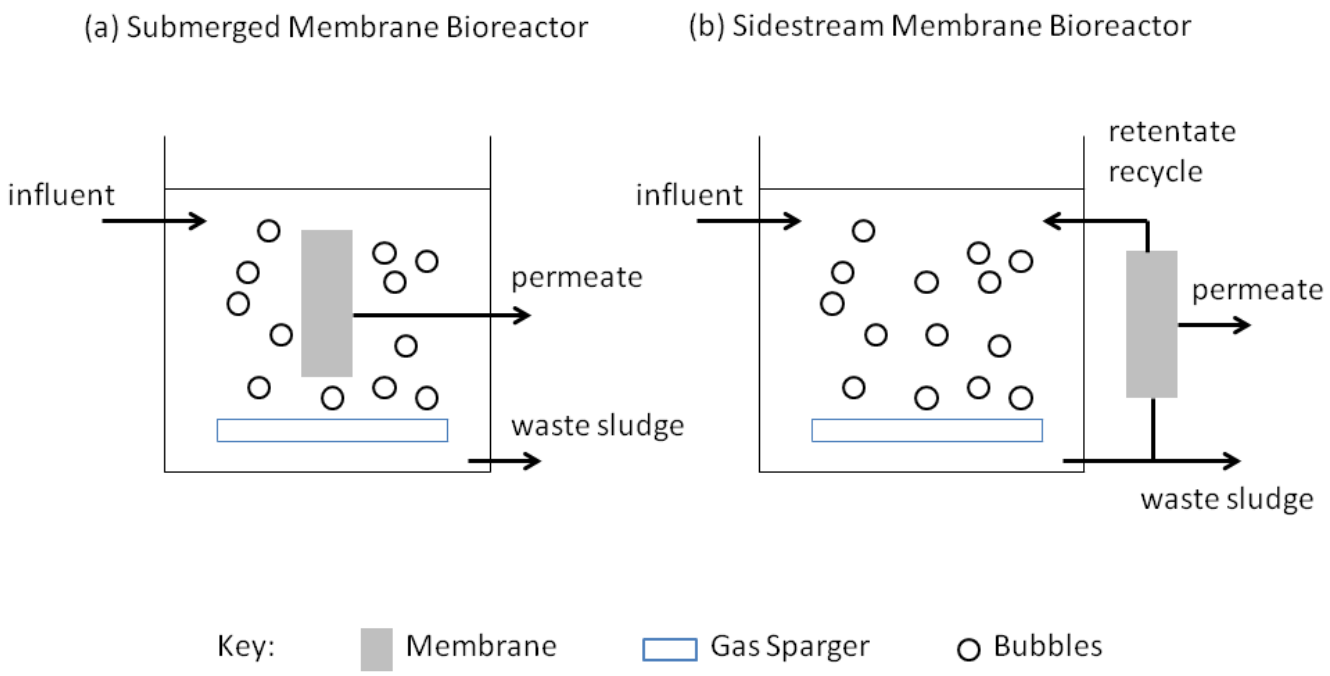

Figure 1.1: Submerged (a) and sidestream (b) configuration of a membrane bioreactor. Taken from Zhao [1].

1.1.2 Submerged and Sidestream Comparison

Membranes are employed in unison with bioreactors to separate material more effectively than the previously used clarifiers [21, 22] and they are essential if water is to be recycled for potable use. Initial designs employed a sidestream allowing the membrane to be housed outside the bioreactor. It was believed that the external housing of the membrane would help to reduce fouling effects from the material inside the bioreactor. The pumping of the fluid out also created a cross flow regime which enhances the filtration. However, considerable energy costs are associated with this pumping.

Yamamoto et. al. [23] instead submerged the membrane within the bioreactor eliminating the additional loop, as shown in Figure 1.1. Submerged systems, where the membrane is inside the bioreactor, remove the need for an energy consuming fluid recirculation loop. However control of concentration polarisation and fouling affects becomes more difficult in these systems [24]. Figure 1.2 shows the submerged flat sheet bioreactor by Kubota. The driving pressure in the liquid in the planes between the flat sheet membrane results from the gravitational head. Suction is applied to the membranes to create the transmembrane pressure to remove the filtered liquid. The bubbling inside an aerobic bioreactor now also acts as an anti-fouling mechanism [25] by disturbing the cake layer on the membrane surface. Submerged hollow fibres are also shaken by the bubbling induced turbulence, aiding cake removal [26].

1.1.3 Airlift

Airlift is the term used to describe the induced flow circulation caused by the addition of a gas phase to liquid. Cui et. al. [27] describe the benefits for ultrafiltration of the airlift effect. The airlift creates a crossflow regime across the membrane in addition to the other benefits of bubbling. In the employed tubular membrane a 30% enhancement, compared to single phase flow with the same liquid velocity, was found. The airlift effect also eliminates the need for a liquid recirculation pump to create the single phase crossflow, reducing the energy demand. Airlift efficiency is discussed in Morrison [28].

In the submerged system the flat sheets do not span the height of the bed. In this way the liquid is not separated at the bottom of the bed allowing flow from one liquid plane to another. If the separated planes have different gas volume fractions then the liquid pressures

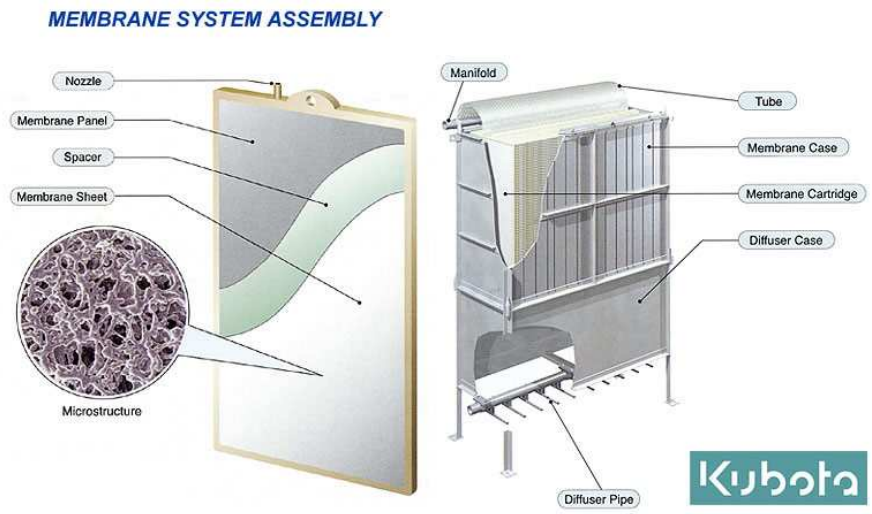

Figure 1.2: Kubota Submerged Flat Sheet Membrane Bioreactor with Gas Sparging [2].

at the base of the planes will also be different. If the gas volume fraction in planes 1 and 2 is ϵ_1 and ϵ_2 respectively then the static pressure below a column of height h and density ρ will be $p_1 = \rho g h\,(1 - \epsilon_1)$ and $p_2 = \rho g h\,(1 - \epsilon_2)$ respectively.

This will result in a pressure drop, $\Delta p = \rho g h\,(\epsilon_1 - \epsilon_2)$. This is more significant where selective sparging is used and one gas volume fraction is very small, e.g. $\epsilon_2 = 0$ giving $\Delta p = \rho g h \epsilon_1$. In this case the pressure drop will drive liquid from the second plane to the first. Therefore, there will also be a non-negligible co-current liquid flow up the first plane with the bubbles and an induced liqwuid downflow in the not aerated section. The water is no longer stagnant. Figure 1.3 shows this effect.

1.2 Concentration Polarisation Model

Concentration polarisation is one of the principal causes of a reduction in flux through the membrane, due to increased flow resistance and osmotic pressures. Figure 1.4 shows the build up of retained solute particles at the membrane wall. At steady state particles deposited at the wall by convective flux will equal those diffused away from the wall by Fick's law, $D\frac{dc}{dz}$,

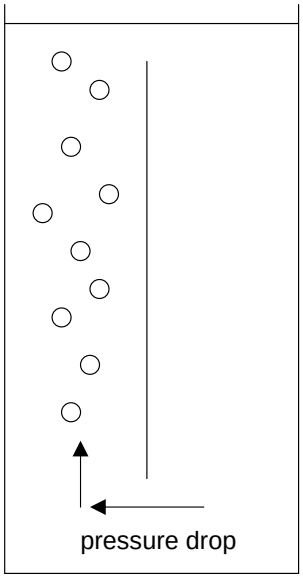

Figure 1.3: Flow induced between a sparged and non-sparged liquid plane.

minus those which permeate the membrane, c_p. Therefore, by mass balance, where D is the diffusivity, c the concentration and J the total volumetric flux, we have

$$Jc - D\frac{dc}{dz} = Jc_p. \tag{1.1}$$

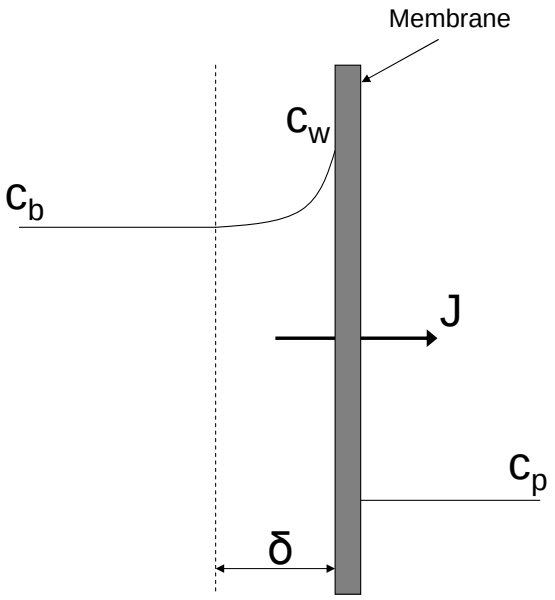

Figure 1.4: Schematic of concentration polarization boundary layer. Adapted from Baker [3].

Integrating equation 1.1 subject to the bulk concentration, $c = c_b$ at $z = 0$, boundary condition gives

$$c = (c_b - c_p)\, e^{\frac{J}{D}z} + c_p. \tag{1.2}$$

Equation 1.2 gives the concentration profile within the boundary layer as a function of position, $0 \leq z \leq \delta$. Applying the wall concentration, $c = c_w$ at $z = \delta$, boundary condition gives equation 1.3.

$$\frac{c_w - c_p}{c_b - c_p} = e^{\frac{J\delta}{D}}. \tag{1.3}$$

If we assume total rejection, $c_p = 0$, then equations 1.2 and 1.3 become equations 1.4 and 1.5 respectively.

$$c = c_b e^{\frac{J}{D}z} \tag{1.4}$$

$$\frac{c_w}{c_b} = e^{\frac{J\delta}{D}} \tag{1.5}$$

Fundamental work has also been undertaken to model the relationship between the hydrodynamic and concentration boundary layers. Lee et. al. [29, 30] develop an iterative method for solving the governing equations of the colloidal concentrations coupled with the hydrodynamic conditions in 2D crossflow ultrafiltration. This requires linking the flux with the concentration profile. The flux will affect the overall flow and the concentration profile will affect the flux requiring an iterative method to satisfy the two conditions.

Similarly Davis et. al. [31] develop a set of relations for the flow of a particle layer along a porous wall, applied in particular to larger particles as may be found in microfiltration mechanisms. They develop the concept of shear-induced hydrodynamic diffusion in a boundary layer of particles away from the wall. At these larger particle volume fractions, it is believed that when a boundary layer of particles is agitated there will be an average net force from the higher concentration side due to collisions, resulting in a diffusion away from the higher concentration side, or wall. This mechanism is distinct from the established Stokes-Einstein diffusion relevant to much smaller particles found in ultrafiltration. Belfort [32] discusses shear induced tubular pinch effect (see Segre et. al. [33]) where larger particles are moved into the central bulk as an explanation of this 'flux paradox'(see Green et. al. [34]) where much larger than expected fluxes are found for larger particles and colloids.

1.3 Permeate flux prediction in membrane separation

1.3.1 Mass transfer coefficient

Instead of modelling the physical flow, a mass transfer coefficient method based on the concentration profile is often employed. Equation 1.5 may be written as equation 1.6 or by equation 1.7 where $k \equiv \frac{D}{\delta}$ is defined as the mass transfer coefficient [35].

$$J = \frac{D}{\delta} \ln\left(\frac{c_w}{c_b}\right) \tag{1.6}$$

$$J = k \ln\left(\frac{c_w}{c_b}\right) \tag{1.7}$$

An analogy between heat and mass transfer using the semi-empirical Sherwood correlation [36] is given by equation 1.8. Where Sh, Re and Sc are the Sherwood, Reynolds and Schmidt numbers respectively. a, b, c, and d are constants based on the flow regime. d_h is the hydraulic diameter and L is the length of the flow. The definitions of these dimensionless numbers are given below, where v is the fluid velocity. Note this is structurally similar to the Dittus-Boelter equation [37] for heat transfer, $Nu = 0.023Re^{0.8}Pr^n$, where Nu, Re and Pr are the Nusselt, Reynolds and Prandtl numbers respectively.

$$Sh = a.Re^b.Sc^c.\left(\frac{d_h}{L}\right)^d \tag{1.8}$$

$$Sh = \frac{kd_h}{D}, \quad Re = \frac{\rho v d_h}{\mu}, \quad Sc = \frac{\mu}{D\rho} \tag{1.9}$$

The hydraulic diameter is used for the length scale in calculating dimensionless numbers within non-circular flow geometries. It may be defined as $d_h = \frac{4A}{U}$ where A is the cross-sectional area of the flow and U is the wetted perimeter. For the flow between two parallel plates of channel thickness Z and width X we have $d_h = \frac{4ZX}{2X} = 2Z$, noting the width of Z does not affect the wetted perimeter. Where the flow is considered to have a laminar velocity boundary layer profile at the wall we have [35], $a = 1.62$ and $b = c = d = 0.33$ for equation 1.8 giving

$$k\frac{d_h}{D} = 1.62\left(\frac{vd_h^2}{DL}\right)^{0.33} \tag{1.10}$$

given $d_h = 2Z$ and $0.33 \approx 1/3$ we have

$$k = 1.62\left(\frac{vD^2}{2ZL}\right)^{0.33} \tag{1.11}$$

For laminar flow between two flat plates the shear at the wall is given by $\gamma = \frac{6v}{Z}$, substituting this into equation 1.11 gives

$$k = 0.713 \left(\gamma \frac{D^2}{L} \right)^{0.33} \tag{1.12}$$

Work by Taha et. al. [38, 39, 40, 41] attempts to link the mass transfer to slug flow induced shear in tubular geometries using this method. They calculate the average shear in the domain and employ relations analogous to equation 1.12. The mass transfer coefficient responds very rapidly to hydrodynamic conditions [42], so it may be more rigorous to simply integrate over the domain. In the above equation, this would involve using $\overline{\gamma^{0.33}}$ instead of $\overline{\gamma}^{0.33}$. Vasan et. al. [43] discuss the limitations of methods based on defining the mass transfer coefficient, $k = D/\delta$, as this only holds when the flux is zero.

Ghosh [4] characterises the flow about the bubble into three regimes: falling film, wake and liquid slug zones, as shown in Figure 1.5. These regimes are then assigned distinct mass transfer coefficients based on the hydrodynamic conditions. Each region is assumed to have uniform mass transfer. In the film region, this will be characterised by the shear generated in the thin region between bubble and membrane. In the wake the mass transfer will be promoted by the mixing effect of the recirculation.

1.3.2 Osmotic Pressure

Osmotic pressure describes the pressure drop driving flow across a semipermeable barrier from a region of low concentration to a region of high concentration. In this way osmotic pressure tries to balance the difference in concentrations either side of the membrane. Except in the case of forward osmosis, osmotic pressure is often undesirable in membrane filtration processes as it causes a reduction in the effective pressure gradient driving the flow. Typically this is expressed by equation 1.13 where $\Delta\Pi = f(c_w)$ is the osmotic pressure, a function of wall concentration.

$$J = \frac{\Delta p - \Delta\Pi}{\mu R_m} \tag{1.13}$$

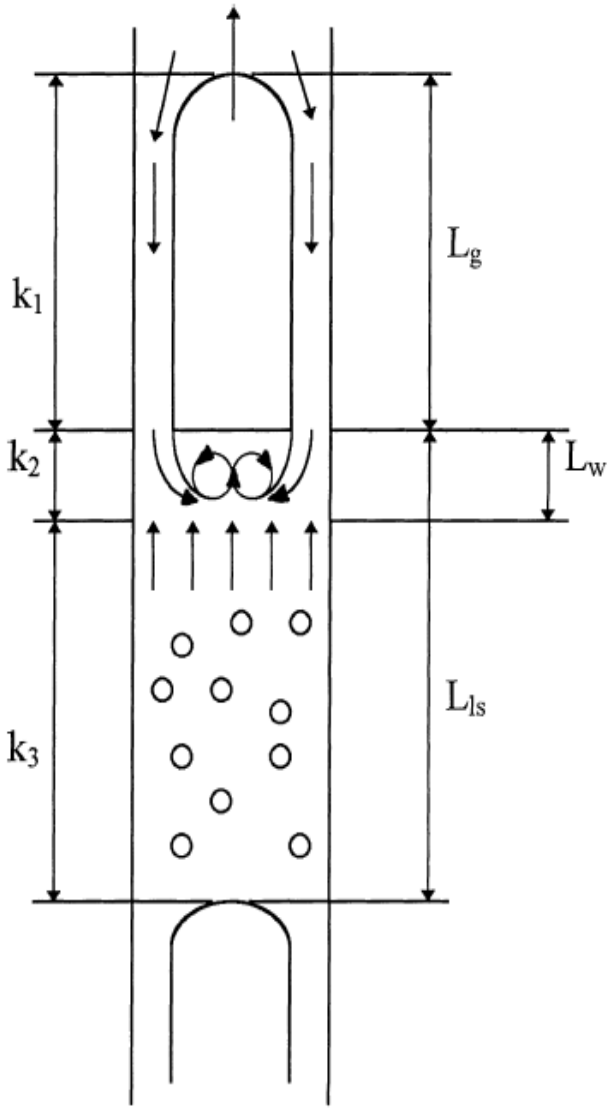

Figure 1.5: Schematic of flow regimes about a slug bubble. In this image three distinct zones are classified from top to bottom: falling film between the bubble and the membrane, wake just below the bubble and liquid slug in the region between the bubbles. Taken from Ghosh [4].

1.3.3 Resistance in series model

The resistance in series model is used to describe flux decline in terms of additional resistance terms. If the total pressure drop across the boundary layer, cake layer and membrane is Δp then we have

$$J = \frac{\Delta p}{\mu \left(R_{bl} + R_{cake} + R_m + R_f \right)} \tag{1.14}$$

using the resistance terms ,R_{bl} for the boundary layer resistance, R_{cake} for the cake layer resistance and R_m, the membrane resistance. In this thesis the boundary layer resistance is defined as the resistance to flux due to drag on the particles in the boundary layer. The boundary layer is the region of increased particle concentration from the bulk concentration up to the membrane wall.

The term R_f is also often employed to account for the resistance due to fouling of the membrane. It may be preferable to incorporate this term within R_m, as the fouling is within the membrane so cannot be considered in series with it. Employing this model over the shear model requires a link between the hydrodynamic conditions and the resistance values.

Figure 1.6 shows a typical flux response with respect to to applied pressure. At low pressures the increase in flux is linear with respect to pressure. Here there is negligible osmotic pressure and the resistance to flow comes only from the membrane resistance, R_m. The gradient of this line is $1/\mu R_m$. At p_1 the curve starts to deflect, J_1 is the critical flux. In this region a concentration boundary layer forms resulting in high wall concentrations and significant osmotic pressure. Boundary layer and fouling resistances may also become significant. As a result resistance is increased and effective driving pressure is reduced.

Approaching p_2 a cake layer will form. This cake will have fixed concentration at the wall and further increases in pressure will result in little wall concentration increase. Additional pressure increases are resisted by a thickening of the cake layer, resulting in little additional flux.

At p_2 the limiting flux J_2 is reached. At this point increases in applied pressure do not yield higher flux. In this region the cake layer will be the dominant resistance and will be directly proportional to the applied pressure. Additional applied pressure will merely cause a thickening of the cake layer and no increase in flux will be enjoyed. If Δp_2, $R_{cake,2}$ and δ_2 are

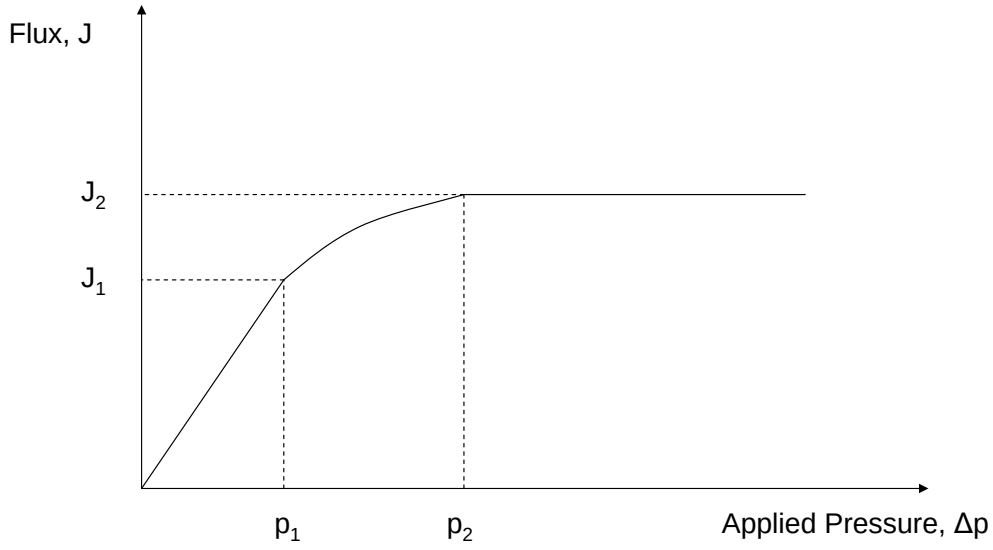

Figure 1.6: This figure shows the result of an increase in resistance with respect to transmembrane pressure for dead-end filtration. In the low TMP region the flux is proportional to the applied pressure, indicating membrane resistance only, with no significant additional resistance. As the TMP is increased the flux does not increase proportionately indicating additional resistance. The resistance is directly proportional to applied pressure as is the dominant resistance. The onset flux at which significant additional resistance forms is the critical flux. At high pressure regions a cake layer has formed which grows proportionately with the applied TMP. This results in no additional flux in this regime. This is known as the limiting flux. Enhancement methods are concerned with increasing this limiting flux.

the applied pressure, resistance and cake layer thickness at incipient max flux respectively we have,

$$\lim_{\Delta p\to\infty} J = \lim_{\Delta p\to\infty} \frac{\Delta p}{\mu\left(R_{bl}+R_{cake}+R_m+R_f\right)} = \frac{\Delta p}{\mu R_{cake}} = \frac{\Delta p_2 \delta/\delta_2}{\mu R_{cake,2}\delta/\delta_2} = \frac{\Delta p_2}{\mu R_{cake,2}} = J_2 \tag{1.15}$$

noting, $\frac{\Delta p}{\Delta p_2} = \frac{R_{cake}}{R_{cake,2}} = \frac{\delta}{\delta_2}$.

Given this limiting flux value, the energy consumed in increasing the applied pressure above p_2 will be wasted reducing the efficiency of the system. However, at higher applied pressures gas sparging has been shown to increase this limiting flux, improving efficiency.

This work focuses on the reduction of reversible resistances external to the membrane by gas sparging. Flux decline resulting from internal fouling is discussed by Field et. al. [44]. A review of the different aspects of flux decline is given by Bacchin et. al. [45].

1.3.4 Resistance of suspended particles

When considering convective flow through a porous medium, Darcy's law is often applied. Darcy's law states that the flow rate per unit area is proportional to the pressure gradient driving the flow, $q = \kappa\frac{dp}{dz}$, when κ is determined by the conditions of the flow and the porous medium. Carmen-Kozeny applied Darcy's law by modelling the flow through suspended particles as equivalent to the flow through many circular capillaries. The total flux is given by the Poiseuille equation 1.16, where N is the number of capillaries per unit area, d_t is the diameter of the capillaries and μ is the liquid viscosity.

$$J = -\frac{\pi d_t^4}{128\mu}\frac{dp}{dx}N \tag{1.16}$$

Conserving the liquid volume fraction of the flow and the particle surface area, equation 1.17 gives the pressure gradient in terms of material properties, where d_p is the particle diameter, and $\alpha = \frac{c}{\rho_p}$ is the particle volume fraction.

$$-\frac{dp}{dx} = \frac{72\mu}{d_p^2} J \frac{\alpha^2}{(1-\alpha)^3} \tag{1.17}$$

Equation 1.17 assumes the flow travels through straight capillaries. However, the flow will have to pass the particles leading to a tortuous path. As a result the flow will have to travel a greater distance. The ratio between the actual length of flow and the straight line distance is considered to be about 2.5. The greater flow length will result in an increase in viscous drag

from the particles giving equation 1.18, noting $72 * 2.5 = 180$. This is the Carmen-Kozeny equation.

$$-\frac{dp}{dx} = \frac{180\mu}{d_p^2} J \frac{\alpha^2}{(1-\alpha)^3} \tag{1.18}$$

Therefore the total pressure drop in the boundary layer is given by equation 1.19, where $\alpha = \frac{c}{\rho_p}$ is given by c from equation 1.4. This pressure drop may be significant in the absence of a high, fixed concentration cake layer at the membrane surface, or if this layer is small as discussed later in section 2.9.

$$\Delta p_{bl} = \frac{180\mu}{d_p^2} J \int_0^{\delta} \frac{\alpha(x)^2}{(1-\alpha(x))^3} dx \tag{1.19}$$

If the flux is given by $J = \frac{\Delta p}{\mu R}$, where R is the resistance to flow then $R_{bl} = \frac{\Delta p_{bl}}{\mu J}$. Then the resistance to flow in the boundary layer is

$$R_{bl} = \frac{180}{d_p^2} \int_0^{\delta} \frac{\alpha(x)^2}{(1-\alpha(x))^3} dx \tag{1.20}$$

At increased applied pressures a cake layer of constant concentration forms at the membrane wall. This layer contributes considerable resistance to flow. A point is reached where additional applied pressure merely increases the cake layer thickness and no increase in flux is seen. The concentration of this cake layer is the bulk concentration at which the flux falls to zero, 60-70% for colloidal suspensions and 25-45% for protein solutions [35]. One notes the cake concentration for colloidal suspensions is similar to that of close-packed spheres. As the cake concentration is constant the resistance to flow R_{cake} is easily calculated. The resistance is given by equation 1.21, where $\alpha_{cake} = \frac{c_{cake}}{\rho_p}$ is the cake volume fraction and δ_{cake} is the thickness of the cake layer.

$$R_{cake} = \frac{180}{d_p^2} \frac{\alpha_{cake}^2}{(1-\alpha_{cake})^3} \delta_{cake} \tag{1.21}$$

Under constant flux operating conditions the required transmembrane pressure (TMP) increases with time to overcome the increased resistance due to fouling. Many researchers [46, 47, 5] have identified a TMP jump, where after a given time the required TMP increases at a much greater rate. At high flux, compression of the cake layer, resulting in higher concentrations, has been proposed to explain the TMP jump [48]. Equation 1.21 can be used

to qualitatively investigate this. Equation 1.22 defines a dimensionless pressure drop, $\Delta p'$, across the cake layer where α_p is the particle volume fraction.

$$\Delta p' = \frac{\Delta p d_p^2}{180 \mu J \delta} = \frac{R d_p^2}{180 \delta} = \frac{\alpha_{cake}^2}{(1 - \alpha_{cake})^3} \tag{1.22}$$

Figure 1.7 shows the increase in dimensionless pressure drop with respect to particle volume fraction in the cake layer. The pressure drop is plotted up to a particle volume fraction of 80%. Given for close-packed spheres the maximum volume fraction is about 74%, we may expect the maximum volume fraction to be less than this. Typical experimental data for the increase in TMP at a given flux is shown in Figure 1.8 for comparison. We see how a small increase in particle concentration can yield a large increase in resistance.

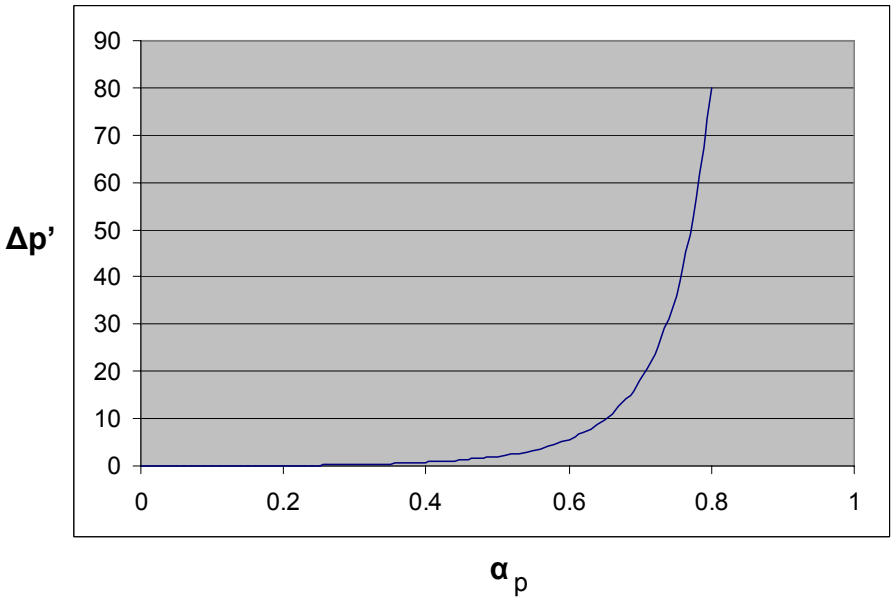

Figure 1.7: The dimensionless pressure drop with respect to particle volume fraction in the cake layer.

The cake layer compression model generates undesired positive feedback which will increase the required TMP very rapidly once a critical point is reached. As the layer starts to compress an increase in applied pressure will increase the compression of the cake layer. This in turn will increase the resistance of the cake which will require a higher pressure creating a vicous cycle until the rate of compression slows as the maximum volume fraction is neared.

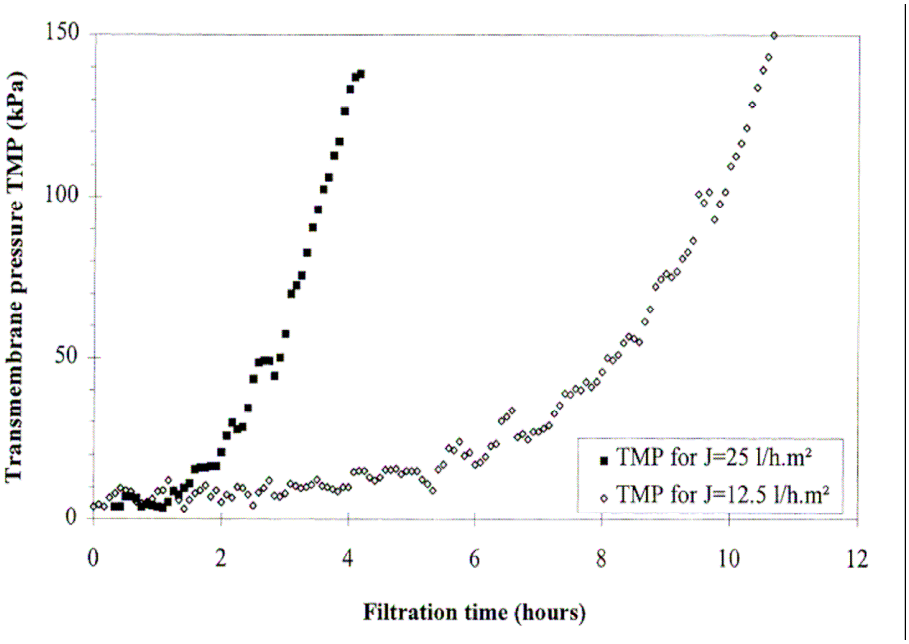

Figure 1.8: Experimental data [5] for fixed flux TMP with respect to time.

However, the TMP may have become intolerably high before this point is reached.

1.3.5 Fouling and Concentration Polarisation Control Methods

The methods employed to reduce flux decline from fouling and concentration polarisation comprise those which allow the process to operate continuously and those which require a pause in operation. Cleaning the membrane often requires the membrane to be out of use for this period. Chemical cleaning can solve otherwise irreversible effects such as the absorption of solutes onto the membrane which increase resistance and reduce flux [49, 50]. Intermittent backflushing, changing the direction of operation, removes foulants from the membrane allowing higher fluxes [51], although the concentration polarisation boundary layer will return in seconds. Aeration without suction [52] can achieve similar benefits and like backflushing does not require removal of the membrane unit. These activities will need to be repeated at a given frequency to have long term benefit to operation [53].

Incorporating secondary flow mechanisms into the system can allow the enhancement of flux whilst maintaining continuous operation. The secondary flow disrupts the concentration polarisation boundary layer, enhancing flux. These mechanisms include pressure variations

resulting from pulsatile flow [54], turbulence generation by inserts [55, 56] and shear and turbulence enhancement by the addition of a gas phase.

1.4 Gas–Liquid Two–Phase Flow

1.4.1 Bubble Behaviour in confined space

Gas–liquid two–phase flow is common in many processes including gas–liquid reactors, fluidised beds, membrane bioreactors and fermentation processes. Cui et. al. [7] provide a review of the enhancement by bubbling of membrane processes. The majority of the literature concerns the enhancement of performance due to gas-sparging in tubular membranes [57, 58, 59, 60]. In this case it has been shown that a slug flow regime provides superior flux enhancement over, say, bubbly or annular flow. It is proposed that the enhancement results from the dynamic nature of the conditions at the membrane wall, in particular the pressure and wall shear stress fluctuations [16, 61, 62]. In addition, a turbulent bubble wake is believed to disrupt the high concentration cake layer that forms at higher pressures resulting in a thinning of this layer reducing the resistance to flow [3]. Figure 1.9 shows the gas-liquid flow regimes in a pipe with respect to gas volume fraction, or voidage. At low voidage many small spherical bubbles exist throughout the pipe. As the voidage is increased large bubbles spanning the width of the pipe are seen. These bubbles are known as slugs or Taylor bubbles. In this flow regime small bubbles are often found between the slug bubbles. Fabre and Line [63] provide an overview of modelling methods for Taylor slugs in vertical tubes. The effect of inclined tubes has also been considered. The velocities and behaviour of bubbles in inclined tubes is discussed in Weber [64] and Spedding [65].

Within this slug flow regime it is of considerable importance, particularly with respect to the energy consumption involved, to consider the effect of bubble size and frequency. Li [66] found that the enhancement of permeate flux increases with respect to bubble frequency for the range of their investigation. Enhancement was also found to be improved as bubble size is increased until a plateau region is reached for larger slugs occupying the whole cross-section of the membrane tube.

Li et. al.[67] investigate the enhancement due to gas sparging in flat sheet membranes. However, their experiment was limited to the flow rate of the gas. The size and frequency of the resultant bubbles was not specified. Experimental work is required to quantify the

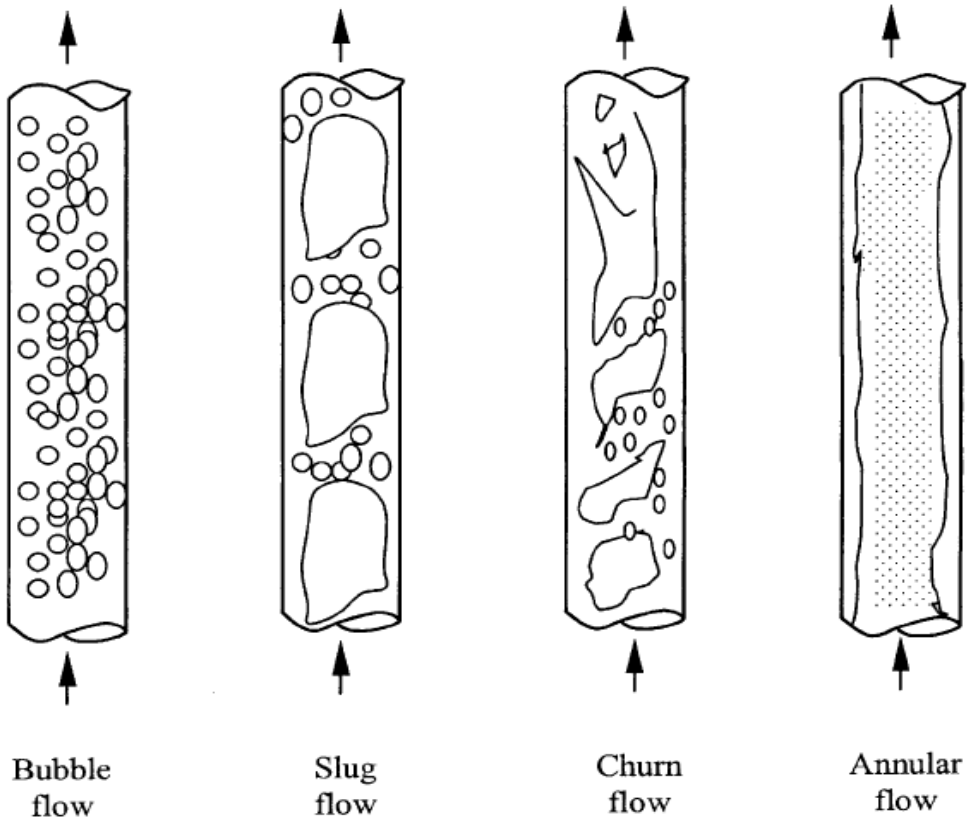

Figure 1.9: Flow regimes with respect to increasing gas volume fraction. Taken from Whalley [6].

enhancement in flat sheet processes where the bubble size and frequency are well defined. This will require greater control of the sparging mechanism than is necessary in a tubular geometry as the bubble motion will not be laterally constrained in planes parallel to the flat sheet.

The nature of the wake behind a bubble is of considerable importance when considering the flux enhancement resultant from gas sparging in submerged membrane bioreactors. Davies and Taylor [68] images showed a closed turbulent wake region behind spherical cap bubbles. Coppus et. al. [69] discuss wakes in detail broadly classifying them into three distinct types: closed turbulent, open turbulent and closed laminar. Closed laminar wakes have been well described mathematically by Hills [70] using potential flow models. Hills found the wake behind a bubble rising between two narrow plates was elliptical rather than circular. Bubbles rising in a thin planar gap have cylindrical rather than spherical caps owing to the near constant cross section of the bubble in the plane of the walls. Turbulent wakes are harder to quantify owing to their non-linear behaviour. A more recent fundamental study is given by Fan & Tsuchiya [71]. One method for obtaining effective imagery of the flow behaviour is Particle Image Velocimetry (PIV) [72, 73, 74]. This employs seed particles which must well match the properties of the fluid being investigated. As such they become entrained in the flow and recording their movement with camera equipment over time provides insight into flow paths velocities.

1.5 Computational Fluid Dynamics

Computational Fluid Dynamics (CFD) is the branch of science and engineering which focuses on providing numerical solutions to the governing equations for a given flow. Typically the governing equations for these flows will not have an analytical solution. A numerical approach is the only alternative to experimental work. The CFD approach is particularly valuable for investigating conditions which would be much more expensive to explore experimentally. This allows for much more design and optimisation work to be done computationally without having to build many experimental apparatus, reducing cost. To provide a numerical solution using CFD requires the flow field to be broken into small cells using a grid of nodes. This allows for the calculation of the local gradients for the governing equations within each cell.

1.5.1 Eulerian Method

Ndinisa et. al. [75, 76] developed Eulerian CFD simulations of bubble swarms between two flat plates. These were used to calculate the bubble behaviour and the resultant shear across the plate. They also employed baffles to segregate the flow in an attempt to improve the overall enhancement properties across the plate. The Eulerian method is limited by requiring a constant bubble size for all bubbles. In addition, the grid mesh perpendicular to the membrane surface wall was coarse rendering the calculated shear values questionable. As a result the overall picture is somewhat qualitative.

1.5.2 Lagrangian Method

Krishna et. al. [12] employed computational fluid dynamics (CFD) [77] techniques to develop semi-empirical relations for the rise velocity of single 2D planar bubbles in beds of powders and liquids. They discuss the influence of bed width on the rise velocity. As the bed becomes narrower the downward liquid film around the bubble exerts more drag on the bubble decreasing the rise velocity. A set of equations for different bed width conditions are presented. For smaller bubbles, diameter less than 20mm, they also find the same techniques reveal the lateral sinuous bubble motion seen in experiment [78].

Essemiani et al. [8] use similar methods to determine the rise velocity of single 2D planar bubbles in liquid. The influence of grid size is discussed, the rise velocity as a function of grid refinement is provided for a given bubble. In addition, they show that non physical break up of bubbles occurs at coarse grid sizes due to inaccurate local curvature of the gas-liquid interface. However, their claim that the oscillatory gyration of these bubbles well describes the gyrations seen in experiment is questionable. These oscillations are not shown for bubbles that do not break up. As a result, we may conclude that the oscillations found in the CFD modelling were linked to the break up of the bubbles.

1.5.3 Turbulence Modelling

The advancement of computational fluid dynamics has developed the possibility to calculate the highly non-linear turbulent effects at higher Reynolds numbers. Direct numerical simulations (DNS) involve solving the Navier-Stokes equations directly. If sufficiently small grid mesh and time steps are used then turbulent effects can be seen. However, as a re-

sult this can require considerable computational resources. Specific turbulence models have been developed in addition to the Navier-Stokes equations to try to capture turbulent effects with less computational demand. The principle models can be grouped as Reynolds-averaged Navier-Stokes equations (RANS) or Large-eddy Simulations (LES) [79]. RANS methods involve adding a calculated time averaged velocity fluctuation component which reflects the turbulent flow. LES models are more computationally demanding than RANS but provide more detail. Larger length scale eddies are calculated directly, then additional equations are employed to try to model the influence of smaller eddies on the overall flow. These models can also be classified by the number of transport equations for turbulence characteristics they employ.

1.6 Control of Bubble Behaviour in Fluidised Beds

The conditions in a bed with multiple bubbles can be highly unstable with respect to time. For example both the gas volume fraction and pressure at a point will change quickly when a bubble leaves/enters the bed or passes the point leading to highly non-linear behaviour. In the time domain the behaviour of the bed is very hard to quantify. However, analysis of the data in the frequency domain by use of a Fourier transform can reveal the characteristics of the bed. For example, to enhance mixing and heat transfer in the bed high frequency events may be implemented. Lim et. al. [80, 81] and Croxford et. al. [82] have developed techniques for the control of bubble distribution and pressure respectively in bubbling fluidised beds. Their method involves determining the plant transfer functions for the response and applying a negative feedback loop with use of a controller to meet some reference demand, as shown in Figure 1.10. In this way specific conditions may be obtained for the behaviour of the bed.

1.7 Thesis Outline

In this thesis the goal is to provide a method to predict the permeate flux enhancement due to the gas phase in a flat sheet membrane filtration set up. In Chapter 2, a fundamental model is developed to allow the permeate flux to be calculated for any given flow field. This is based on the simple principles of convection and diffusion governing the behaviour of a suspended solute. This numerical method also includes an approach for dealing with the very different hydrodynamic and particle boundary layer sizes. The generality of the solution method allows

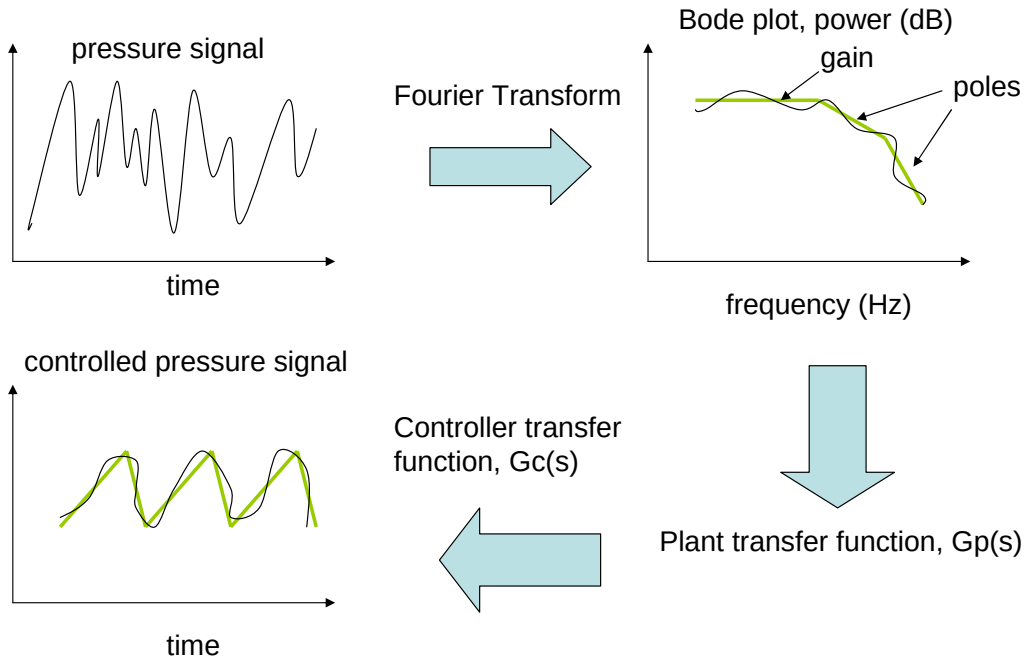

Figure 1.10: Frequency control method for bubbling conditions which have highly volatile responses in the time domain.

it to be applied to any hydrodynamic conditions. This model is tested against results for single phase crossflow, where theory is well established, for the purpose of validation.

In Chapter 3 a computational fluid dynamics solution is developed to calculate the bubble shape and its surrounding flow field between two parallel flat plates. This employs the volume of fluid method which deals with multiphase flows and in particular the interface between the phases to provide the bubble shape. Different bubble volumes are investigated against different gap widths between the two plates. Whilst traditionally the flow geometry will be constant and the gas volume varied, here the analysis will focus on the effects of changes in flow geometry on a given gas volume. Methods are developed to analyse these results in this constant gas volume approach. The bubble shape and rise velocity are validated against known results.

The key elements for the flow model are shown in Figure 1.11. Gas is introduced in the liquid-filled narrow channels between the flat sheet membranes. The permeate is drawn out of these membranes. The gas-liquid flow between one pair of these flat sheet membranes is to be modelled.

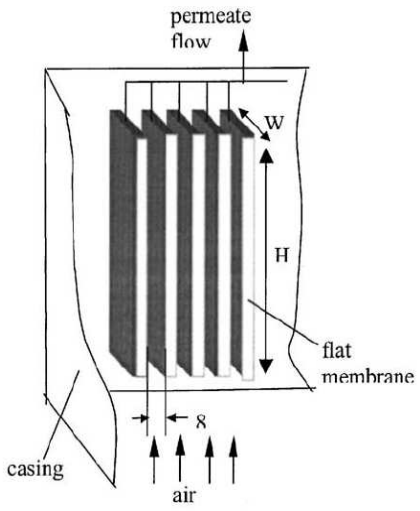

Figure 1.11: Submerged Flat Sheet Membrane Bioreactor with Gas Sparging schematic [7]. The flow to be modelled is gas-liquid between the parallel membranes.

Chapter 4 brings together the two previous chapters to provide a general solution for flux

enhancement for a gas bubble between two flat sheet membranes. The hydrodynamics are taken from the CFD calculation and used as the input for the convection terms of the flux model. The solutions for different gap widths and gas volumes are then compared to find the optimal conditions for flux enhancement. A metric based on the bubble size is composed. To be able to achieve the desired bubble size, shape correlations established in Chapter 3 are used to provide a method for generating the desired bubble to maximise performance. Finally Chapter 5 incorporates both the concluding remarks and offers suggestions for further work to build upon the methods and analysis presented here.

2 Development of Particle - Flux Models

2.1 Introduction

Modelling the particle and flux behaviour in membrane filtration systems encounters difficulty due to the different length scales of the participant phases. In crossflow filtration, the hydrodynamic boundary layer of the liquid phase may be of the order of magnitude of millimetres whereas the boundary layer size of the suspended particles is of the order of microns. The length scales differ by a factor of one thousand. The cell size for the particle phase will need to be much smaller than if only the liquid phase was being considered. Without refinement and simplification this will lead to an excessive computational burden when solving numerically on a mesh.

Traditionally this obstacle has been overcome using mass transfer correlations based on the shear on the surface of the membrane, as discussed in the literature review. The actual particle behaviour is not calculated. These correlations assume the particle boundary layer size to determine the mass transfer coefficient, 'k'.

The model presented here makes no such assumption and calculates the particle behaviour directly. To overcome the obstacle described above it is necessary to decouple the particle and fluid behaviour. It is assumed that the particle concentration does not significantly influence the fluid behaviour. The fluid flow governs the convection of the particles but the particle concentration does not influence the fluid flow. The fluid velocities are determined from literature for crossflow along a porous boundary and from CFD for more complicated multiphase flow systems. These are then use to calculate the particle and flux behaviour.

In addition to the decoupling of the phases, another method is employed to deal with the difference in length scales. The mesh which is used to calculate the particle behaviour is refined in the direction of the membrane. As such the cell size in the bulk will be suited for representing the liquid boundary layer and the cell size near the membrane will be much smaller to represent the particle boundary layer. This is done by successively refining the cells next to the membrane by a factor of two, until the cell size is of the order of less than one micron. This requires more sophistication in setting up the numerical model as the cell size is a function of displacement and many normal simplifications will not apply.

2.2 Simplifications and Assumptions

The particle behaviour is assumed to obey the convection diffusion equation. This ignores other particle interaction effects. The particles are assumed to be entrained in the liquid. Hence the fluid velocity terms govern the convective behaviour of the suspended particles. The diffusivity will result from a combination of both molecular diffusivity and shear induced diffusivity.

The resistance to the permeate flux through the membrane from the particle phase is assumed to be solely in the form of drag on the particle surface. Effects like pore blocking are not considered. The decline in flux in such systems due to concentration polarisation is assumed to be in the form of an increase of resistance from the particles.

2.3 Convection-Diffusion Equation

The particle concentration, c, in the system is found by the solution of the convection-diffusion, equation 2.1.

$$\frac{\partial c}{\partial t} + u\frac{\partial c}{\partial x} + v\frac{\partial c}{\partial y} + w\frac{\partial c}{\partial z} = D\left(\frac{\partial^2 c}{\partial x^2} + \frac{\partial^2 c}{\partial y^2} + \frac{\partial^2 c}{\partial z^2}\right) \tag{2.1}$$

On the left is the time dependent term and the convection terms. The velocity matrices, u, v, and w, are the flow terms for the hydrodynamics. The velocity matrix normal to the membrane, w, has the flux through the membrane added to it.

2.4 Diffusivity

The Diffusivity is influenced by two different mechnisms, the molecular diffusion, which will be dominant for smaller particle sizes (less than $0.1\mu m$) and hydrodynamically induced behaviour which is significant for larger particles as they have a greater influence on the flow. The Stokes-Einstein equation 2.2 gives the diffusivity of a single spherical solute moving through a liquid, where k is the Boltzmann constant, T is the temperature in Kelvin, a is the solute radius and μ is the solution viscosity. n depends on the radii of the solutes. For larger solutes, greater than 10Å, no slip may be assumed, giving $n = 6$ (drag on a sphere). However, for smaller solutes the interaction becomes more complex and the no slip condition may no longer be

assumed. A loss in drag will result in higher diffusivities. Hence a smaller value for n is required [83]. To represent both these mechanisms the diffusivity, D, is taken as the sum of the Stokes-Einstein molecular diffusion and the shear induced diffusion [84].

$$D = \frac{kT}{n\pi a\mu} \tag{2.2}$$

The shear induced diffusion is given by equation 2.3, where, a, is the particle radius and, γ, is the shear rate normal to the membrane.

$$D = 0.03a^2\gamma \tag{2.3}$$

Hence the total diffusion is given by equation 2.4, this is used isotropically.

$$D = \frac{kT}{n\pi a\mu} + 0.03a^2\gamma \tag{2.4}$$

2.5 Numerical Method

The convection-diffusion equation 2.1 is to be solved numerically using an explicit finite differences method. The first gradients for the convection terms are shown below. For convergence backward differences are required when the velocity coefficient is positive, equation 2.5, and forward differences are required when the velocity coefficient is negative, equation 2.6. The other first gradients in the y direction are similarly found.

If $u_{i,j,k} > 0$,

$$\frac{\partial c}{\partial x}|_{i,j,k} = \frac{c_{i,j,k} - c_{i-1,j,k}}{\Delta x} \tag{2.5}$$

If $u_{i,j,k} < 0$,

$$\frac{\partial c}{\partial x}|_{i,j,k} = \frac{c_{i+1,j,k} - c_{i,j,k}}{\Delta x} \tag{2.6}$$

The second gradients for the the diffusion terms are found using Maclaurin and central differencing. This is shown in equation 2.7, the second gradient in the y direction is found similarly.

$$\frac{\partial^2 c}{\partial x^2}|_{i,j,k} = \frac{c_{i+1,j,k} - 2c_{i,j,k} + c_{i-1,j,k}}{\Delta x^2} \tag{2.7}$$

2.5.1 Time Step Convergence

The unsteady term $\frac{\partial c}{\partial t}$ is given by the first order explicit equation 2.8. Where n is the time counter and Δt is the time step. An explicit scheme is used as for a 3-dimensional simulation the required memory was too great. This scheme performed satisfactorily and is simpler to implement, so a 4th order Runge-Kutta scheme was not used.

$$\frac{\partial c}{\partial t} = \frac{c_{i,j,k}^{n+1} - c_{i,j,k}^{n}}{\Delta t} \tag{2.8}$$

The three dimensional convergence criteria for the time step is given by equation 2.9, taken from Roache [77]. In order to satisfy convergence, the time step has to be sufficiently small to ensure the magnitude of the growth term is less than 1. A time step of 0.4 milliseconds was found to be satisfactory.

$$\Delta t \leq \left[\frac{|u|}{\Delta x} + \frac{|v|}{\Delta y} + \frac{|w|}{\Delta z} + 2D \left(\frac{1}{(\Delta x)^2} + \frac{1}{(\Delta y)^2} + \frac{1}{(\Delta z)^2} \right) \right]^{-1} \tag{2.9}$$

2.5.2 Numerical Dispersion

In addition to stability and convergence, it is also important there is no significant distortion by the numerical scheme of the wave propagation in the solution of the convection-diffusion equation.

If $u > 0$ we have in the x-direction

$$\frac{c_i^{n+1} - c_i^n}{\Delta t} + |u| \frac{c_i - c_{i-1}}{\Delta x} = D \frac{c_{i+1,j,k} - 2c_{i,j,k} + c_{i-1,j,k}}{\Delta x^2} \tag{2.10}$$

$$c_i^{n+1} = c_i + \Delta t \left[c_{i+1} \left(\frac{D}{\Delta x^2} \right) - c_i \left(\frac{2D}{\Delta x^2} + \frac{|u|}{\Delta x} \right) + c_{i+1} \left(\frac{D}{\Delta x^2} + \frac{|u|}{\Delta x} \right) \right] \tag{2.11}$$

substituting $c = \tilde{c} e^{j(kx - \omega t)}$ where k is the wave number and ω the corresponding frequency we get

$$e^{-j\omega \Delta t} = 1 + \Delta t \left[e^{jk\Delta x} \left(\frac{D}{\Delta x^2} \right) - \left(\frac{2D}{\Delta x^2} + \frac{|u|}{\Delta x} \right) + e^{-jk\Delta x} \left(\frac{D}{\Delta x^2} + \frac{|u|}{\Delta x} \right) \right] \tag{2.12}$$

equating real terms

$$\cos(\omega\Delta t) = 1 + (\cos(k\Delta x)) - 1)\left(\frac{2D\Delta t}{\Delta x^2} + \frac{|u|\Delta t}{\Delta x}\right) \tag{2.13}$$

given for small x, $\cos(x) \simeq 1 - x^2/2$

$$\frac{w}{k} = \sqrt{\frac{2D}{\Delta t} + \frac{|u|\Delta x}{\Delta t}} \tag{2.14}$$

therefore

$$\frac{\partial w}{\partial k} = \sqrt{\frac{2D}{\Delta t} + \frac{|u|\Delta x}{\Delta t}} \tag{2.15}$$

Given the phase speed, $C_p = \frac{w}{k}$, and the group velocity, $C_g = \frac{\partial w}{\partial k}$, are the same, the system is non-dispersive. Similarly if $u < 0$

$$C_p = C_g = \sqrt{\frac{2D}{\Delta t} - \frac{|u|\Delta x}{\Delta t}} \tag{2.16}$$

2.5.3 Mesh Refinement Near Membrane

In the direction normal to the membrane we are interested in the concentration very close to the membrane, less than a micron order of magnitude. In order to solve the whole system together a variable mesh is used in the z direction. For the z terms the grid size is variable, decreasing nearer the membrane. If there are k nodes in the z direction there will be $k-1$ cells in that direction. We will define the width of the k_{th} cell as Δz_k. Therefore using the same convergence conditions as above we have

If $w_{i,j,k} > 0$,

$$\frac{\partial c}{\partial z}|_{i,j,k} = \frac{c_{i,j,k} - c_{i,j,k-1}}{\Delta z_{k-1}} \tag{2.17}$$

If $w_{i,j,k} < 0$,

$$\frac{\partial c}{\partial z}|_{i,j,k} = \frac{c_{i,j,k+1} - c_{i,j,k}}{\Delta z_k} \tag{2.18}$$

In the z direction where the mesh is variable the second gradients are more complicated as fewer terms cancel out.

$$c_{i,j,k+1} = c_{i,j,k} + \Delta z_k \frac{\partial c}{\partial z}|_{i,j,k} + \frac{\Delta z_k^2}{2!}\frac{\partial^2 c}{\partial z^2}|_{i,j,k} + \bigcirc\left(\Delta z_k^3\right) \tag{2.19}$$

$$c_{i,j,k-1} = c_{i,j,k} - \Delta z_{k-1} \frac{\partial c}{\partial z}|_{i,j,k} + \frac{\Delta z_{k-1}^2}{2!}\frac{\partial^2 c}{\partial z^2}|_{i,j,k} + \bigcirc\left(\Delta z_k^3\right) \tag{2.20}$$

Adding the above equations and neglecting third order terms gives:

$$c_{i,j,k+1} + c_{i,j,k-1} = 2c_{i,j,k} + \frac{\partial c}{\partial z}\left(\Delta z_k - \Delta z_{k-1}\right) + \frac{\partial^2 c}{\partial z^2}\frac{\Delta z_k^2 + \Delta z_{k-1}^2}{2} \tag{2.21}$$

Rearranging:

$$\frac{\partial^2 c}{\partial z^2} = \frac{2}{\Delta z_k^2 + \Delta z_{k-1}^2}\left[c_{i,j,k+1} - 2c_{i,j,k} + c_{i,j,k-1} + \frac{\partial c}{\partial z}\left(\Delta z_{k-1} - \Delta z_k\right)\right] \tag{2.22}$$

Note how equation 2.22 reduces to the form of equation 2.7 when $\Delta z_k = \Delta z_{k-1}$.

2.5.4 General Solution

The complete finite differences solution of equation 2.1 is given by equation 2.23, where the gradient terms are defined above. The particle concentration at a given point for the next time step, $c_{i,j,k}^{n+1}$, is found based on the previous concentration. The initial concentration is uniform with value equal to the bulk concentration, c_b. The solution to the finite differences are found using code written in Matlab.

$$c_{i,j,k}^{n+1} = c_{i,j,k}^{n} - \Delta t\left[u_{i,j,k}\frac{\partial c}{\partial x}|_{i,j,k} + v_{i,j,k}\frac{\partial c}{\partial y}|_{i,j,k} + w_{i,j,k}\frac{\partial c}{\partial z}|_{i,j,k} - D\left(\frac{\partial^2 c}{\partial x^2}|_{i,j,k} + \frac{\partial^2 c}{\partial y^2}|_{i,j,k} + \frac{\partial^2 c}{\partial z^2}|_{i,j,k}\right)\right] \tag{2.23}$$

2.5.5 Boundary Conditions

The membrane wall flux boundary condition is given by equation 2.24, where J is the flux. It is assumed the permeate concentration is zero. In the case of cake build up on the membrane wall, strictly this equation applies at the edge of the cake layer. However, as the width of the cake layer is negligible compared to the width between the membranes, this effect is ignored and the results are found from the membrane wall, with an additional resistance term in the flux calculation to represent the presence of the cake layer.

$$Jc - D\frac{\partial c}{\partial z} = 0 \tag{2.24}$$

Equation 2.24 is solved using the following finite difference method. Noting there are P nodes in the z direction, i.e. $c_{i,j,P}$ is the concentration on the membrane.

$$J_{i,j}c_{i,j,P-1} = \frac{D_z}{\Delta z_{P-1}}\left(c_{i,j,P} - c_{i,j,P-1}\right) \tag{2.25}$$

which yields

$$c_{i,j,P} = c_{i,j,P-1}\left(\frac{J_{i,j}\Delta z_{P-1}}{D_z} + 1\right) \tag{2.26}$$

Only a half the domain is modelled. Symmetry at the plane halfway between each membrane wall is assumed to provide the boundary condition. At the top of the domain is the inlet for the crossflow, the concentration here is fixed at the bulk concentration, c_b. The crossflow is from top to bottom in the Y direction, although gravitational acceleration is not included in the single phase calculation. This is done to provide better comparison with the bubble case. In the bubble case, gravity causes the rise of the bubble in the vertical Y direction which induces a downward flow around the bubble. At the bottom, symmetry is also assumed, i.e. the build up has reached equilibrium and will not develop over any greater length. Figure 2.2 illustrates this.

2.6 Flux Resistance Model

The resistance model is used to calculate the flux. A fixed trans-membrane pressure (TMP) is used. The initial flux is found taking the clean water membrane resistance, R_m. $J_{initial} = \frac{TMP}{\mu R_m}$.

As particles are driven toward the membrane wall by convection, concentration polarisation occurs. The additional resistance in this boundary layer is modelled as $R_f = R_{bl} + R_{cake}$. The flux is calculated at each point on the membrane surface, then averaged as below. The subscripts i, j denotes the nodes in the x and y direction respectively.

$$J_{i,j} = \frac{TMP}{\mu\left(R_m + R_{f(i,j)}\right)}$$

$$J = mean_{x,y}\left[J_{i,j}\right]$$

2.6.1 Carmen-Kozeny Equation

The resistance to flow due to the particle concentration is calculated using Carmen-Kozeny. Equation 1.20 is discretised by equation 2.27 to calculate the boundary layer resistance, where $\alpha = \frac{c}{\rho_p}$ is the particle volume fraction

$$R_{bl(i,j)} = \frac{180}{d_p^2}\sum_{k=1}^{P-1}\frac{\alpha_{i,j,k}^2}{\left(1-\alpha_{i,j,k}\right)^3}\Delta z(k) \tag{2.27}$$

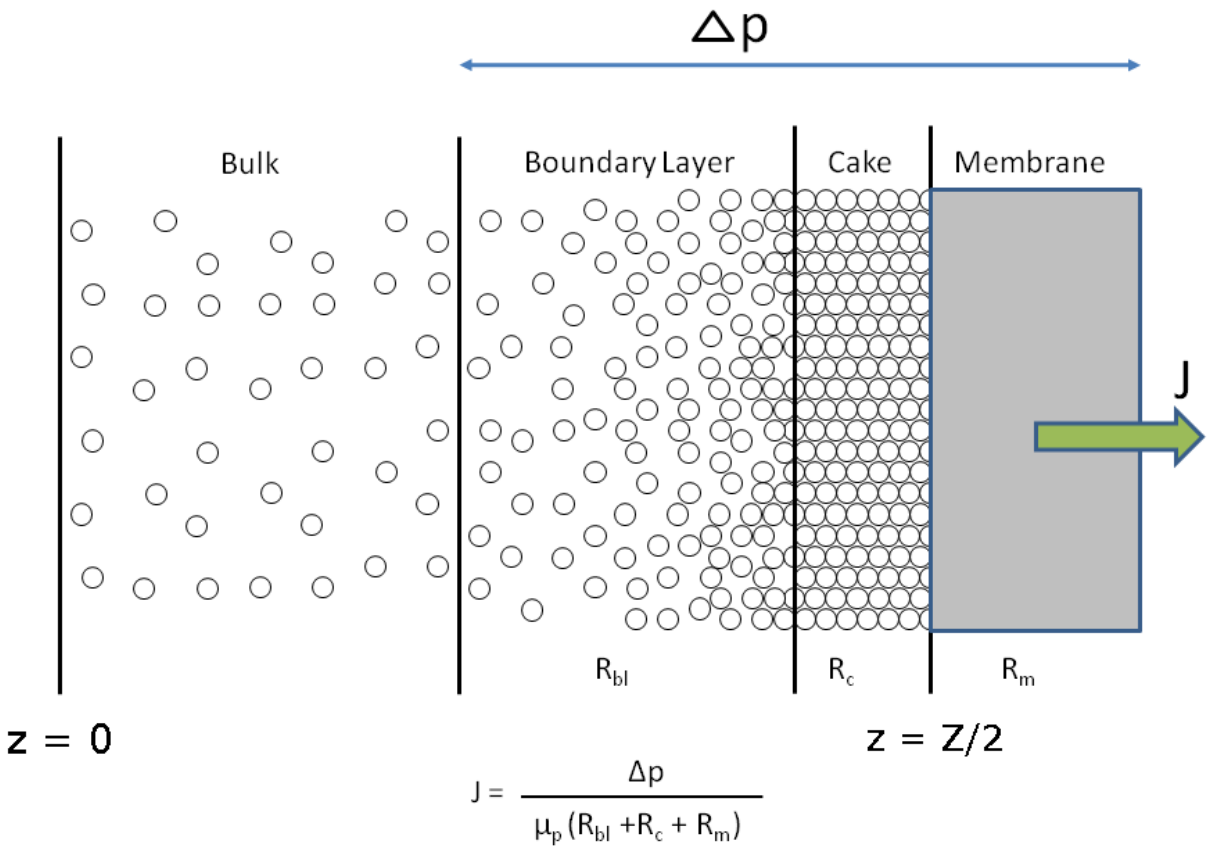

Figure 2.1: Illustration of the different particle resistance regimes near the membrane. From the bulk region there is a concentration polarisation build up to the membrane, where a cake layer of maximal concentration forms. The resistance of the boundary layer and the cake layer are calculated as the change with time and are added to the membrane resistance.

2.7 Cake Layer Resistance

The resistance due to the cake layer on the membrane, equation 1.21, is calculated at each node by equation 2.28.

$$R_{cake(i,j)} = \frac{180}{d_p^2} \frac{\alpha_{cake}^2}{(1-\alpha_{cake})^3} \delta_{cake(i,j)} \tag{2.28}$$

The total resistance is therefore calculated as below.

$$R_{f(i,j)} = R_{bl(i,j)} + R_{cake(i,j)}$$

2.8 Converging The Solution

The flux and the particulate behaviour are interdependent. An increase in flux will increase the transport of particles toward the membrane. This will increase the resistance, reducing the flux. N.B. The velocity normal to the membrane, w, is, *at the wall*, equal to the flux, J.

1. Calculate the hydrodynamic flow.
2. Export the velocity terms.
3. Calculate the initial clean water flux.
4. Solve conv-diff equation for next time step using the calculated velocity terms and the new flux.
5. If maximum concentration is reached at the membrane increase the cake thickness to bring the membrane concentration back to the permitted maximum.
6. Calculate new resistance and update flux.
7. Repeat 4 to 6 until the convection toward the wall, for the given flux, is balanced by the diffusion away from the membrane wall.

2.9 Results - Single Phase Crossflow

Before introducing more complicated multi-phase flows the flux is calculated for the much simpler case of single phase crossflow to validate the model. In the case of a simple, single phase, steady, fully developed crossflow, the governing equations can be integrated analytically to provide solutions, as shown in the literature review. In these cases the method of calculating the mass transfer coefficient from the shear at the membrane surface has been shown to be valid. Here the model solutions will be compared to those results coming from this theory. The flow field is calculated for both the model and theory solution. For the theory only the shear at the membrane is required, whilst the model uses the entire field. The two methods will be compared for using various different variable values to check the model is robust.

For single phase flow the Sherwood correlation is well established. This is valid for steady shear rates which are present in steady crossflow set ups which are two dimensional in character. The flux model is simplified to 2D form. The flux using this method is given by equation 2.29 where, c_w and c_b, are the wall and bulk concentrations respectively. The mass transfer coefficient is given by equation 1.12 where γ is the shear rate, D is the diffusion ceofficient and L is the characteristic domain length, in this case the membrane height.

$$J_v = k \ln\left(\frac{c_w}{c_b}\right) \tag{2.29}$$

$$k = 0.713\left(\gamma\frac{D^2}{L}\right)^{0.33} \tag{2.30}$$

The laminar cross flow along a semi porous boundary is calculated using equation 2.31, the flow perpendicular to the membrane is given by equation 2.32 taken from Berman [85], where $Re = w_{wall}Z\rho/2\mu$ is a Reynolds number, $b = \frac{Y-y}{Z}$ and $\lambda = \frac{2z-Z}{Z}$. The resulting concentration build-up is illustrated in Figure 2.2.

$$v(y,\lambda) = \left[\bar{v}(0) - \frac{w_{wall}}{b}\right]\left[\frac{3}{2}\left(1-\lambda^2\right)\right]\left[1 - \frac{Re}{420}\left(2 - 7\lambda^2 - 7\lambda^4\right)\right] \tag{2.31}$$

$$\frac{w(\lambda)}{w_{wall}} = \frac{\lambda}{2}\left(3-\lambda^2\right)) - \frac{Re}{280}\lambda\left(2 - 3\lambda^2 + \lambda^6\right) \tag{2.32}$$

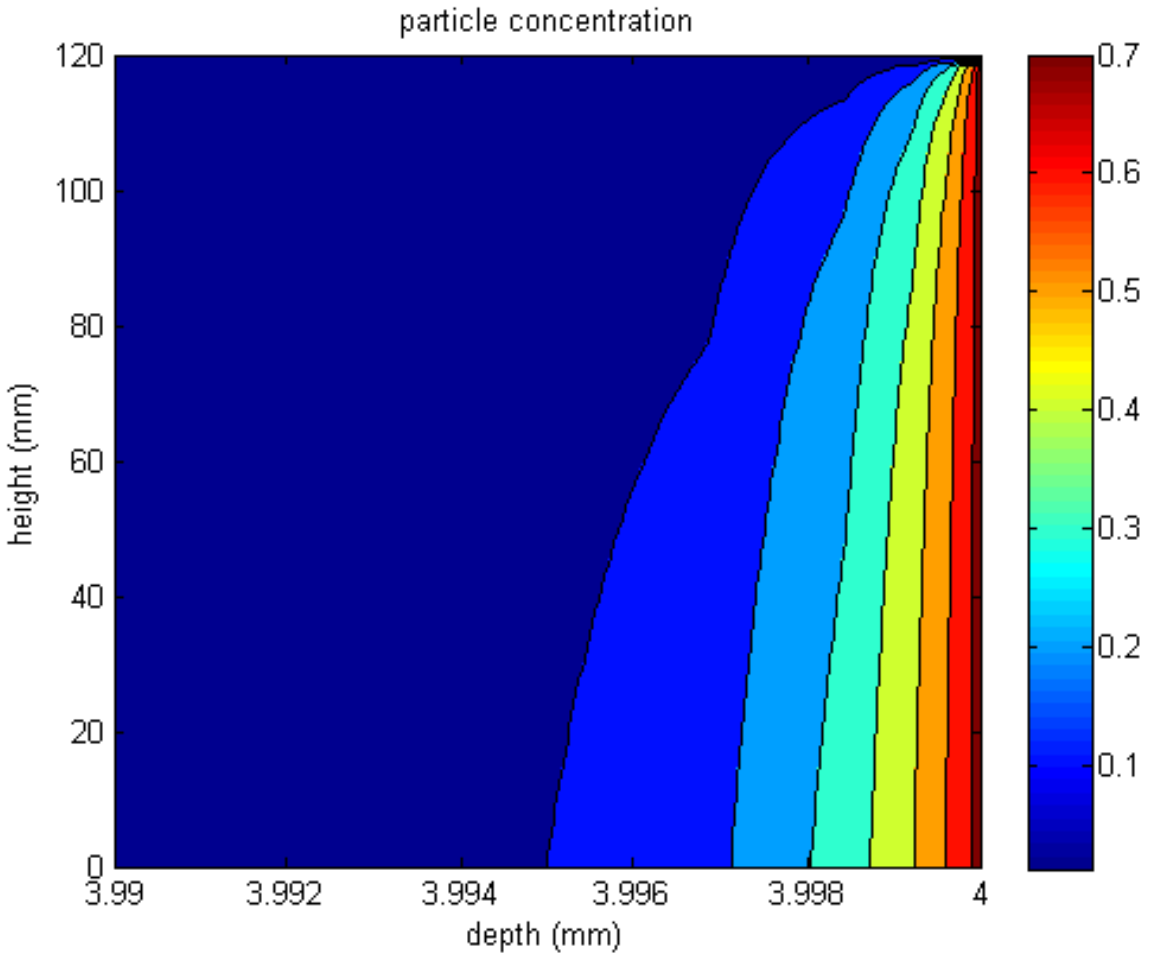

Figure 2.2: This figure shows the build up in concentration from the inlet at the top.

Figure 2.4 shows the comparison between the flux calculation method developed in this thesis and the semi-empirical Sherwood correlation mass transfer method. The transmembrane pressure was fixed at 100kPa, the particle size was 0.1 microns with a bulk concentration of 25g/L. The effect of the mean flow velocity is investigated. The domain height is 120mm and the half-width between the membranes is 4mm. The cell size in the vertical y direction is 1.7mm and in the z-direction the base cell size is 0.4mm for which the cell adjacent to the membrane is refined (halved) downwards 12 times to 0.098 microns.

Transmembrane Pressure (TMP)	ΔP	100 kPa
Temperature	T	293 K
Particle diameter	d_p	0.1 μm
Bulk Concentration	c_b	25 g/L
Domain height	Y	120mm
Gap width	Z	8mm

Figure 2.3: Values used to obtain results, except where stated.

2.9.1 Crossflow Velocity

Figure 2.4 shows the increase in flux with respect to mean crossflow velocity. Higher crossflow velocities will generate larger shear at the surface which will give higher values for k and therefore flux as defined in equation 2.29.

2.9.2 Transmembrane Pressure

The flux for the model and the mass transfer shear method with respect to transmembrane pressure is shown in Figure 2.5. The results capture three distinct resistance regimes. Initially there is negligible resistance compared to the membrane resistance and the flux increases in a straight line with gradient $\frac{1}{\mu R_m}$. As the boundary layer develops with greater TMP, resistance increases due to the increase in concentration towards the membrane. Note the comparison of the model with the theory. Theory takes no account of the interaction between the boundary layer and cake layer, merely that flux is constant once the maximal wall concentration is reached. This results in a sudden transition from clean water resistance to significant cake

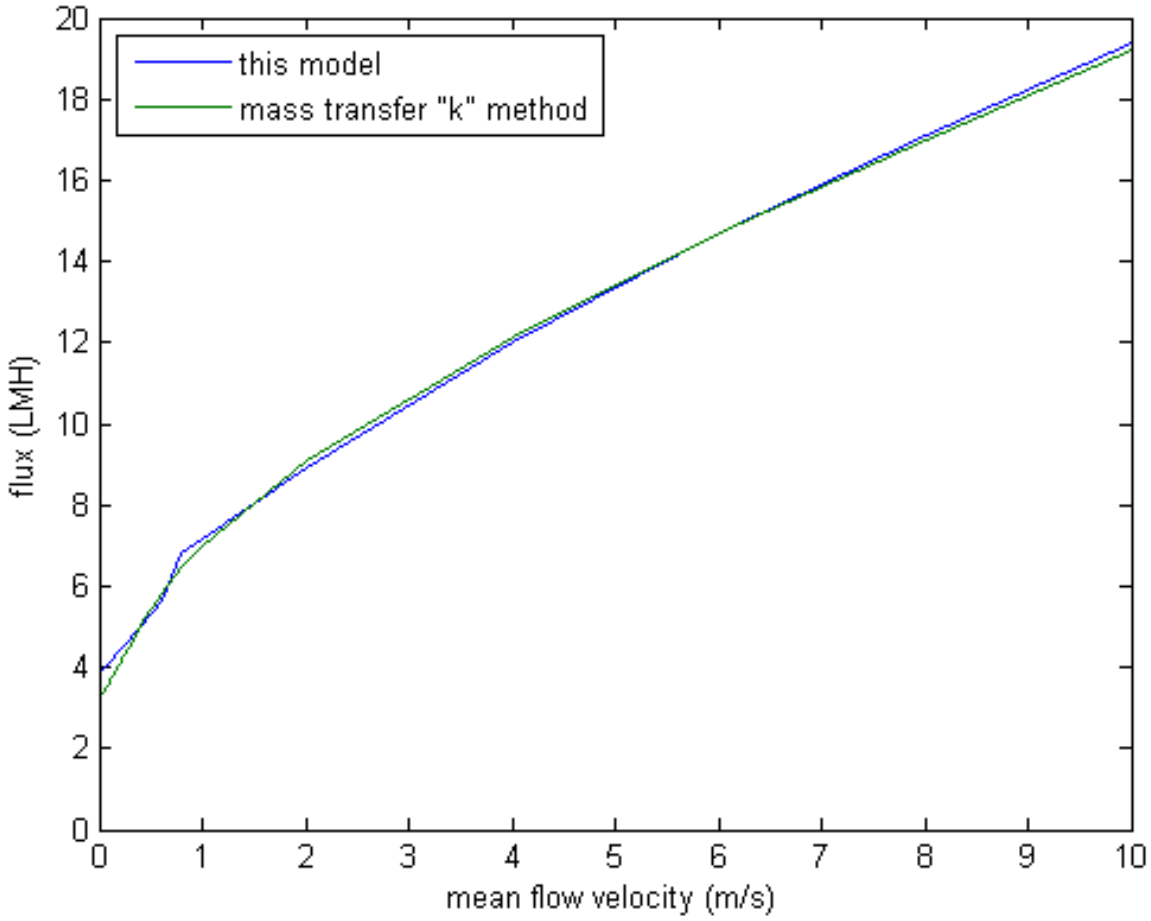

Figure 2.4: The variation in flux with respect to the mean crossflow velocity is shown. The results show the comparison between the two flux calculation methods. To attain steady state the model is run until negligible changes in flux are seen, as shown in Figure 2.19

layer resistance. The model, however, shows a gradual transition as the boundary layer develops and the cake layer starts to form. In the higher flux regions the cake layer is dominant, rendering the flux constant at its limit.

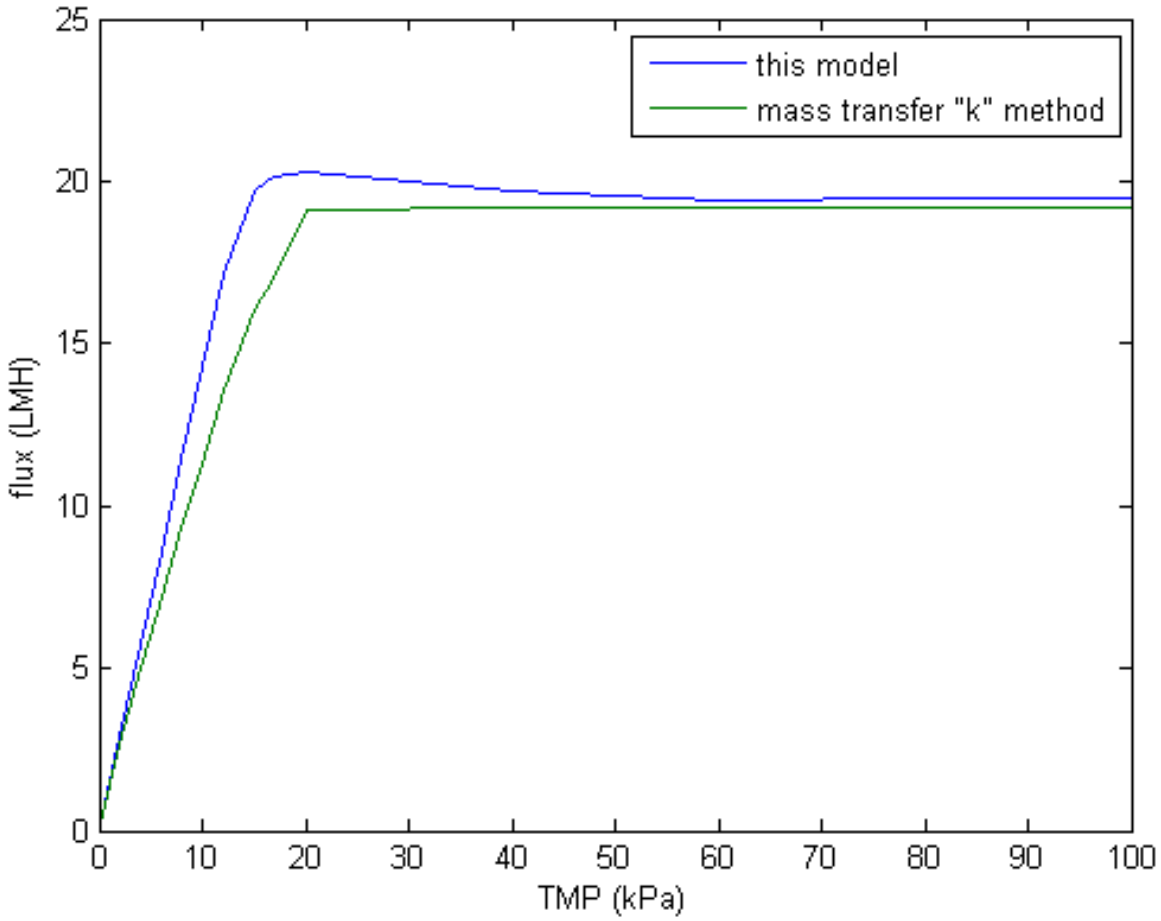

Figure 2.5: Flux with respect to transmembrane pressure for each method. The three regions of constant membrane resistance only, critical flux onset and limiting flux are well captured.

Figure 2.6 shows the behaviour of the boundary layer with respect to transmembrane pressure. Clearly in the lower flux regions the wall concentration is sub maximal and additional TMP increases the wall concentration. As the wall concentration is attained however the boundary layer undergoes a thickening. This explains the interaction shown between the boundary layer and cake layer resistance as seen in Figure 2.5

It is interesting to note the existence of a small peak in the flux performance which is not present for the old theory. It is instructive to refer to the general equation used to calculate

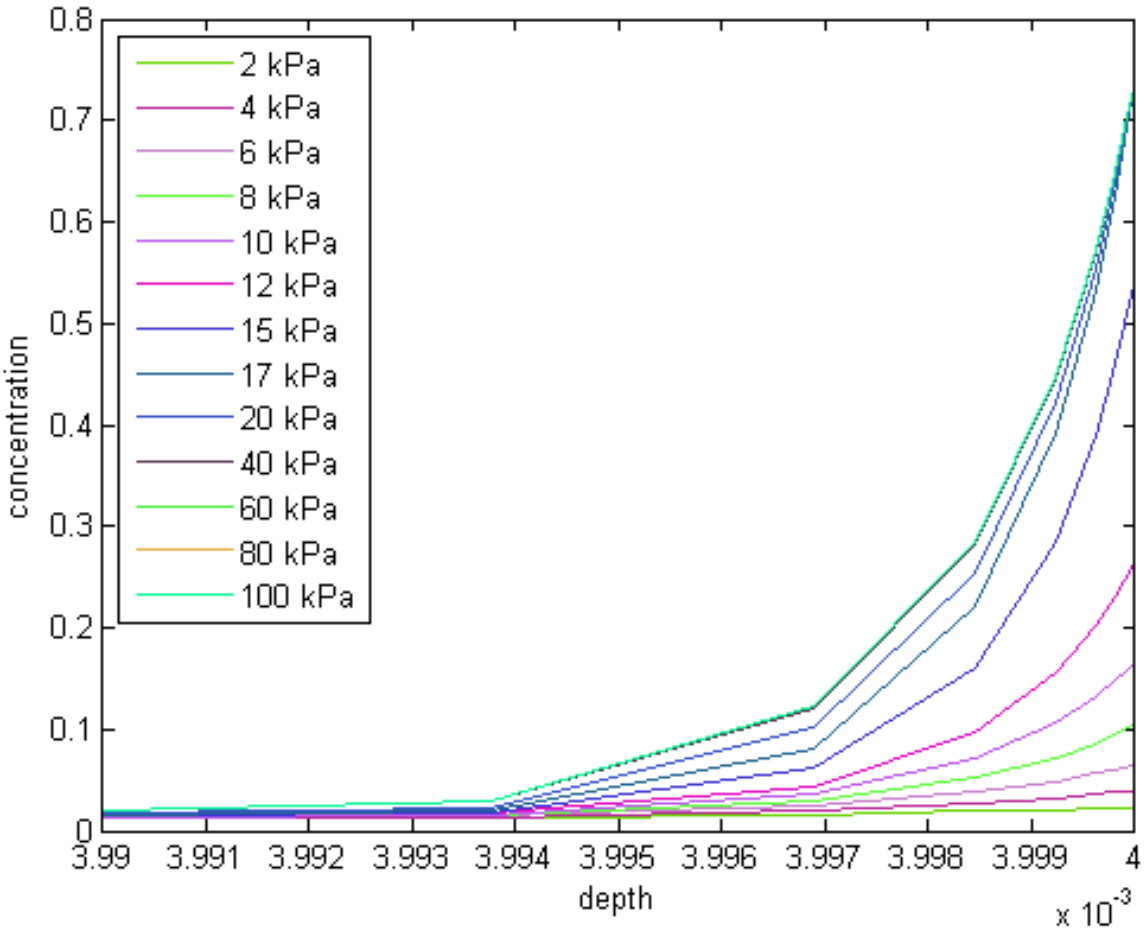

Figure 2.6: Concentration polarisation boundary layer with respect to transmembrane pressure. The concentration is given as the particle volume fraction, the depth is in mm. When the transmembrane pressure exceeds 40kPa the change in the boundary layer is negligible, hence the curves for these higher pressures appear overlaid and indistinct.

the flux. Here for simplicity we will refer to the transmembrane pressure as, P, rather than TMP and the total resistance as R.

$$J = \frac{P}{\mu R} \tag{2.33}$$

If we differentiate the above equation with respect to P we have:

$$\frac{dJ}{dP} = \frac{1}{\mu R^2}\left(R - P\frac{dR}{dP}\right) \tag{2.34}$$

In the model the resistance comprises three components: the membrane, the cake layer and the boundary layer. $R = R_m + R_c + R_{bl}$.

Now we may assume that the membrane resistance is independent of transmembrane pressure, i.e. $\frac{dR_m}{dP} = 0$. Therefore $\frac{dR}{dP} = \frac{dR_c}{dP} + \frac{dR_{bl}}{dP}$. So we have:

$$\frac{dJ}{dP} = \frac{1}{\mu R^2}\left(R - P\left(\frac{dR_c}{dP} + \frac{dR_{bl}}{dP}\right)\right) \tag{2.35}$$

To find stationary points we also require $\frac{dJ}{dP} = 0$. So we have:

$$R = P\left(\frac{dR_c}{dP} + \frac{dR_{bl}}{dP}\right) \tag{2.36}$$

The stationary pressure is found at solutions to the following equation:

$$P - \frac{R}{\left(\frac{dR_c}{dP} + \frac{dR_{bl}}{dP}\right)} = 0 \tag{2.37}$$

Figure 2.7 shows the resistance of the boundary layer with respect to TMP and Figure 2.8 its gradient. After some initial early settling at low TMP the resistance of the boundary layer increases sharply until the maximum wall concentration is reached at 20 kPa, then the change is more gentle as the boundary layer thickens slightly. At 40 kPa this process is completed resulting in a constant resistance boundary layer resistance at higher fluxes.

Figure 2.9 shows the resistance of the cake layer with respect to TMP and Figure 2.10 its gradient. At low TMP no cake layer is present as the boundary layer is still forming and the wall concentration is below maximum. At higher TMP once the wall concentration reaches its maximum the cake layer starts to form, more slowly at first as the boundary layer hasn't finished developing. However as the TMP is increased further all additional resistance

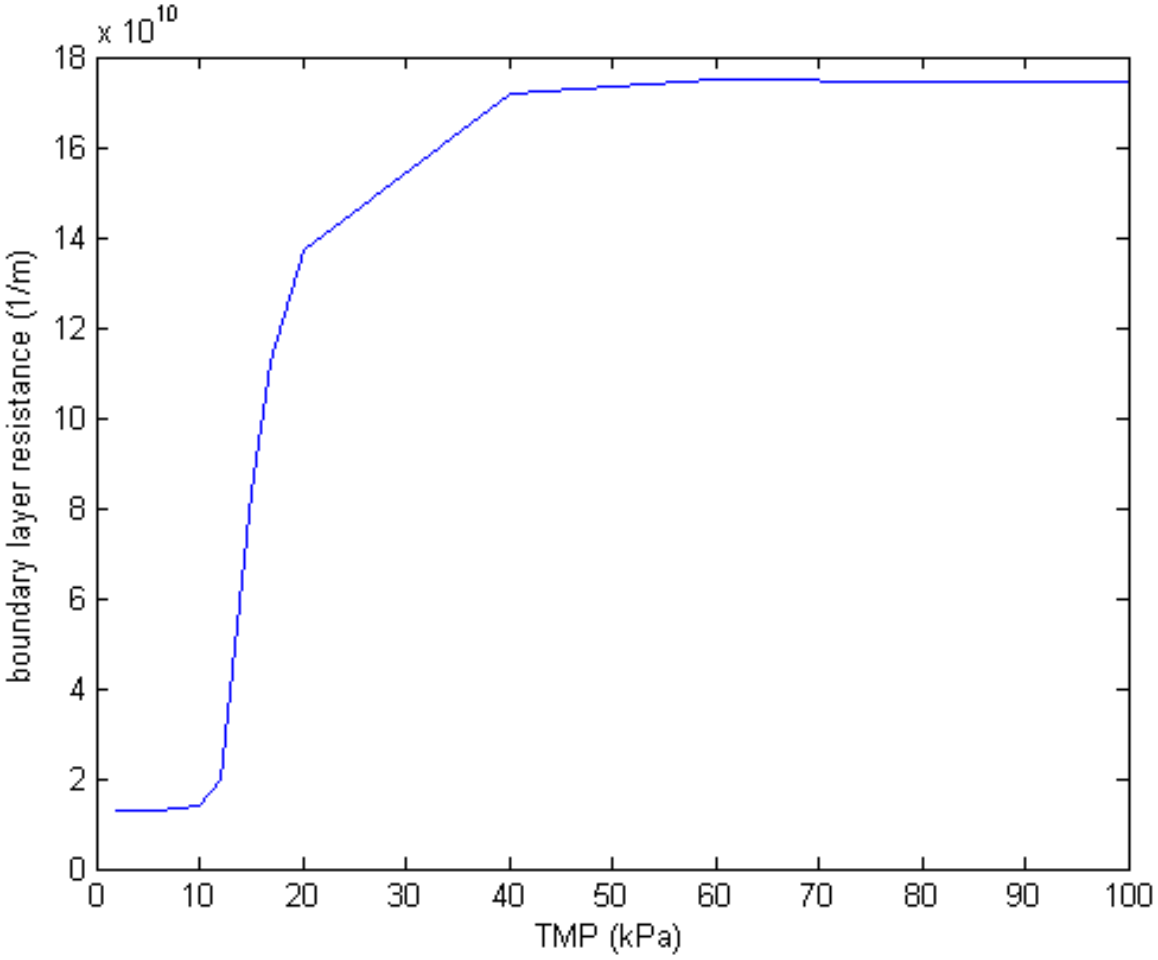

Figure 2.7: Boundary layer resistance with respect to transmembrane pressure.

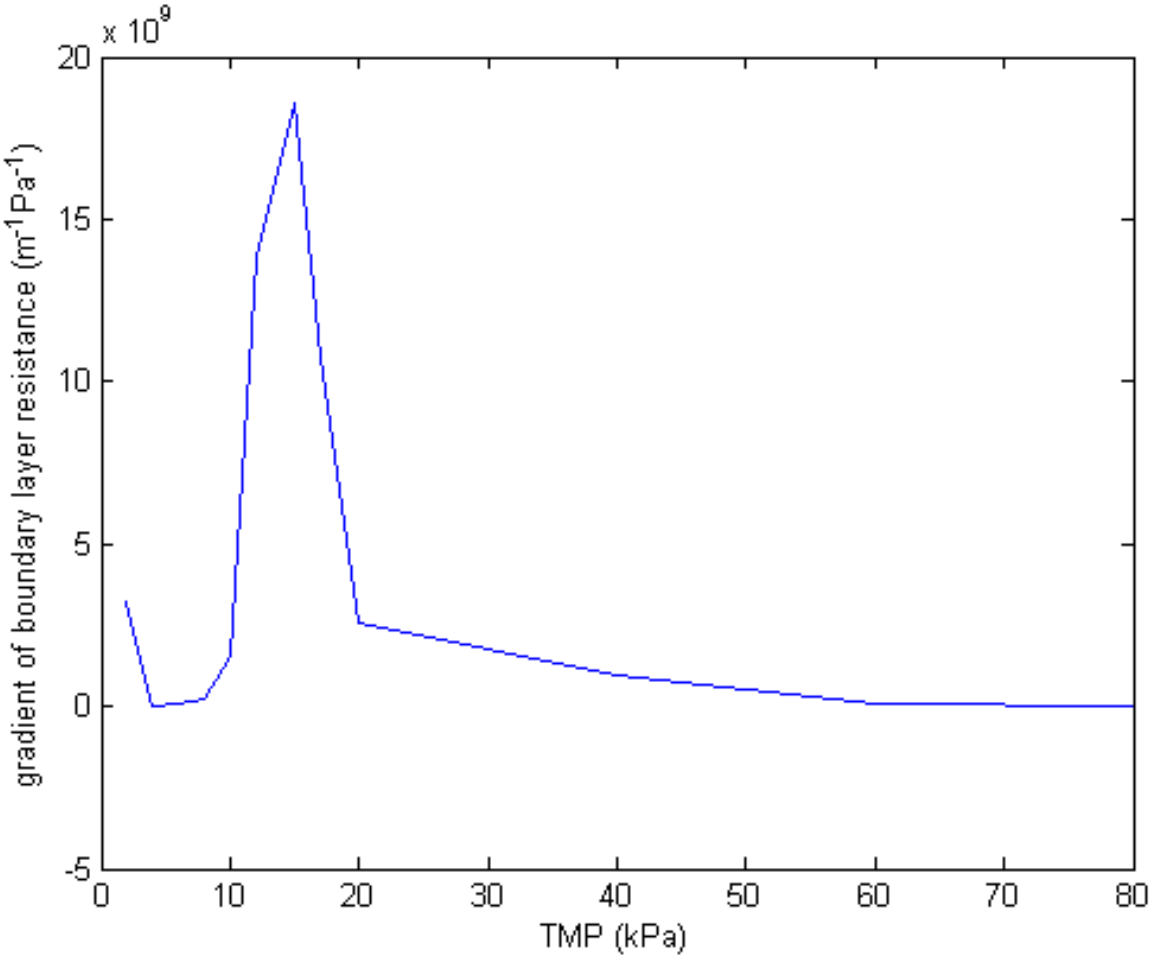

Figure 2.8: The resistance gradient of the boundary layer with respect to transmembrane pressure.

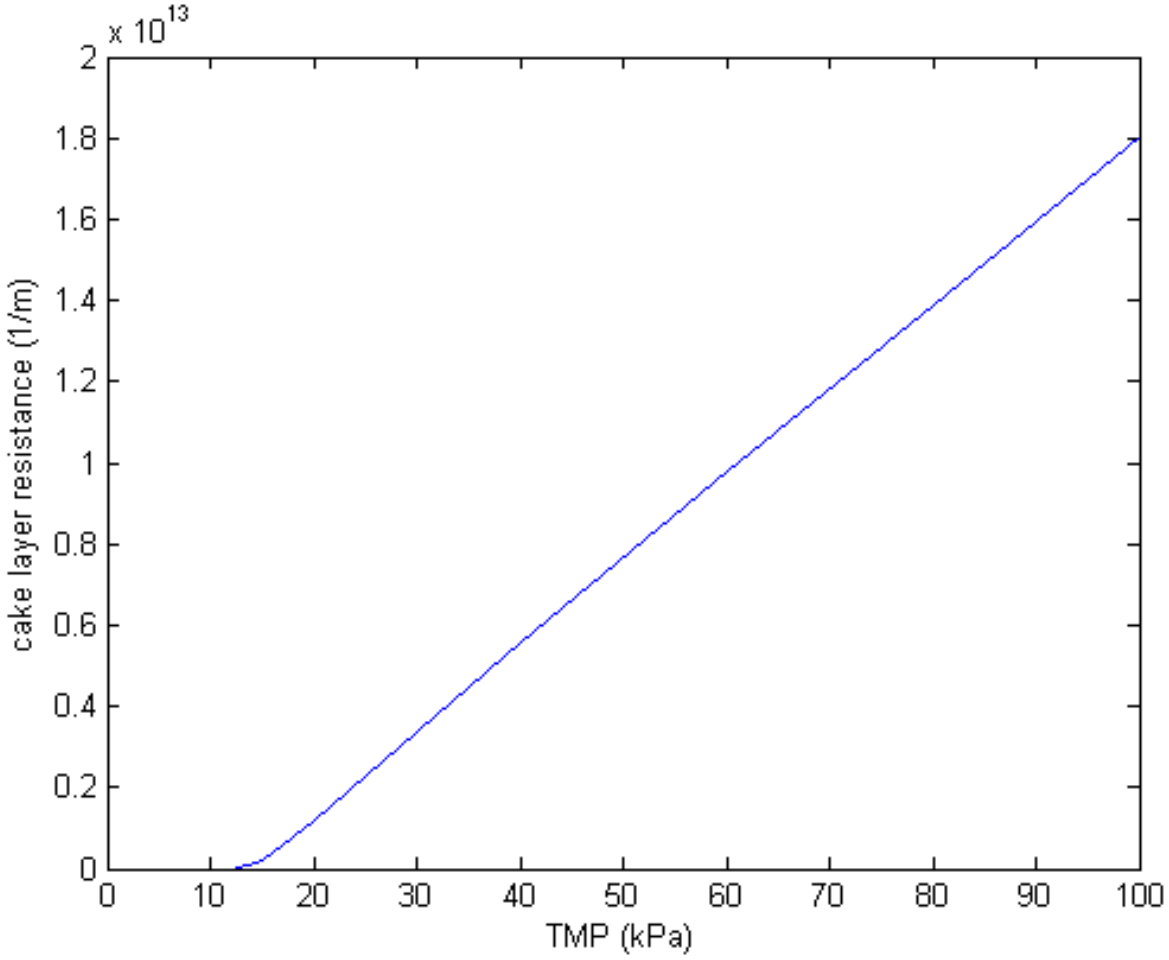

Figure 2.9: Cake layer resistance with respect to transmembrane pressure.

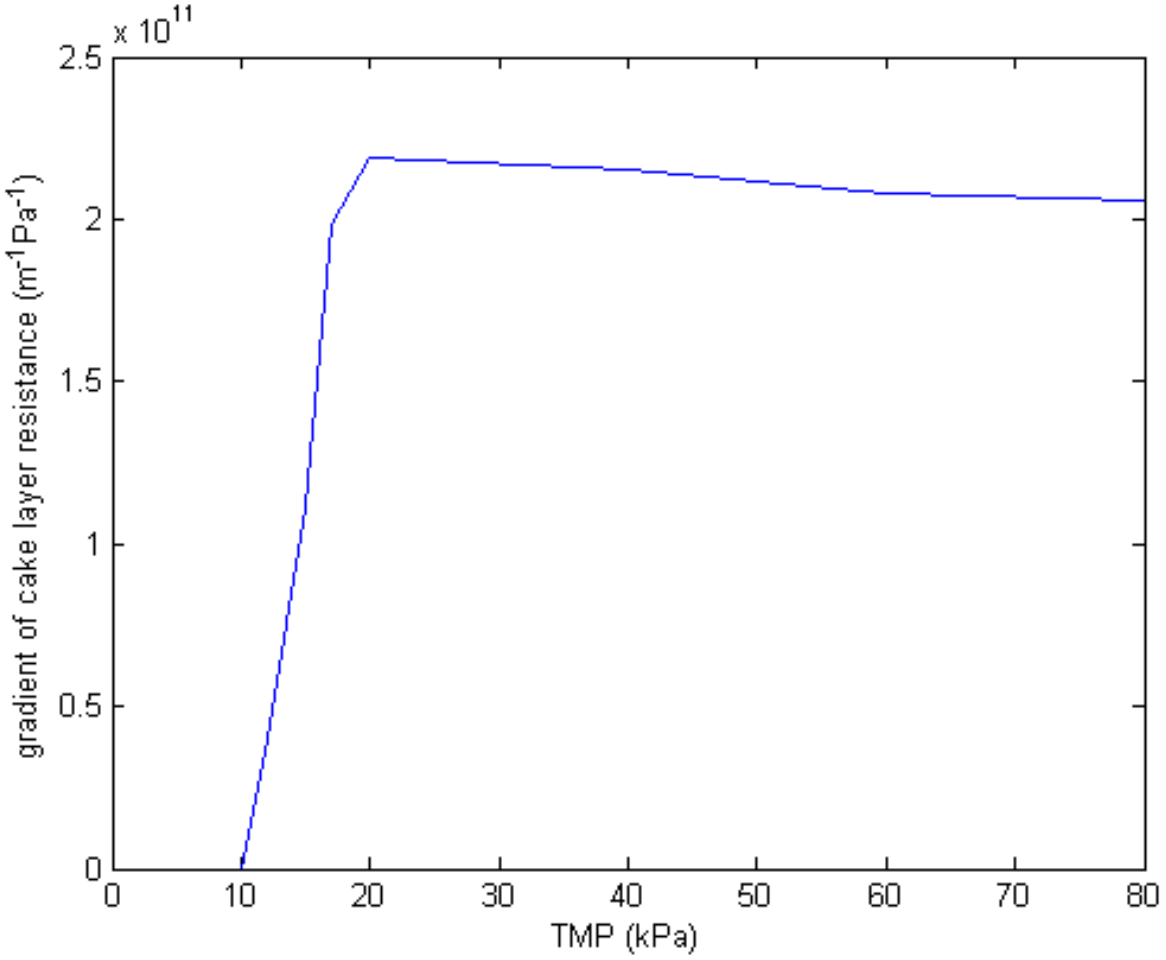

Figure 2.10: The resistance gradient of the cake layer with respect to transmembrane pressure.

is formed by a thickening of the cake layer, resulting in the proportional cake increase with TMP.

The peak in resistance gradient in Figure 2.10 corresponds with the peak in flux seen in Figure 2.5 as expected by equation 2.37. Figure 2.11 plots $\frac{\delta J}{\delta(TMP)}$ against TMP. The two pressures at which $\frac{\delta J}{\delta(TMP)}$ is zero are the stationary points of equation 2.33 and therefore satisfy equation 2.37, given $\frac{1}{\mu R^2} > 0$.

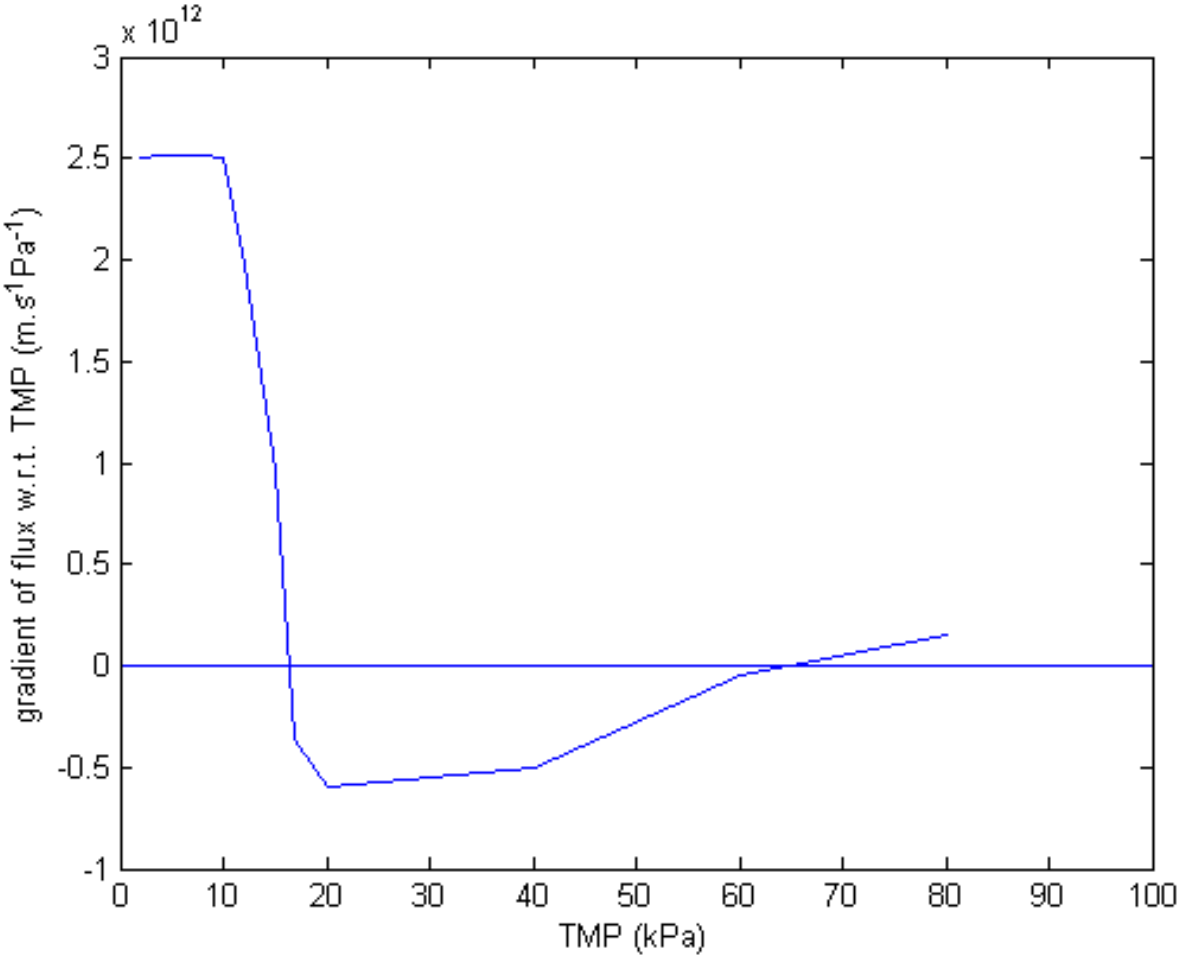

Figure 2.11: Gradient of flux with respect to transmembrane pressure. Note the zeroes indicating stationary points.

2.9.3 Concentration Polarisation

During the membrane separation process the rejected material accumulates near the membrane. This results in a large concentration gradient from the feed side to the permeate

side. A high concentration on the feed side and a low concentration on the permeate side. This is known as concentration polarisation. Figure 2.12 shows the concentration polarisation boundary layer up to a maximum particle volume fraction of 0.74. The bulk concentration is 0.015. If one defines the boundary layer as starting at the point where the concentration exceeds bulk concentration plus ten percent (0.0165) then the boundary layer thickness is found to be 15 microns in this case. This definition is necessary as there will be a large region where the concentration is marginally above the bulk, but is too insignificant to constitute the origin of the boundary layer.

The size of the boundary layer is important in filtration theory.To calculate the mass transfer coefficient, $k = \frac{D}{\delta}$ where D is the diffusivity, equation 1.6 requires a value for the boundary layer width, δ. The boundary layer thickness is often arbitrarily chosen to be $20\mu m$ for this purpose. In the present model, no such assumption is required. The boundary layer width is calculated directly. Actual measurement of the boundary layer in experiment is very difficult as the layer is so small.

When the calculation is run, the initial concentration is bulk throughout the domain. As the simulation time elapses, the boundary layer will develop. Figure 2.13 illustrates this effect. The boundary layer quickly forms in response to the convection of particles to the membrane by the flux. Its rate of development slows towards its final profile as the resistance of the layer increases, resisting the flux.

2.9.4 Particle Size

Figure 2.14 shows the relationship between particle size and flux. The model conforms well to the theory for particle sizes less than 0.5 microns, with some divergence for larger particles. The flux passes through a minimum at 0.1 microns. This correlates with the diffusivity given in equation 2.4. The diffusivity goes through a minimum near 0.1 microns also. Differentiating equation 2.4 with respect to particle radius gives:

$$\frac{\delta D}{\delta a} = 0.06a\gamma - \frac{kT}{n\pi a^2 \mu} \tag{2.38}$$

The stationary point is found at $\frac{\delta D}{\delta a} = 0$ giving equation 2.39. The second derivative evaluated at this point is greater than zero, confirming it as a minimum point.

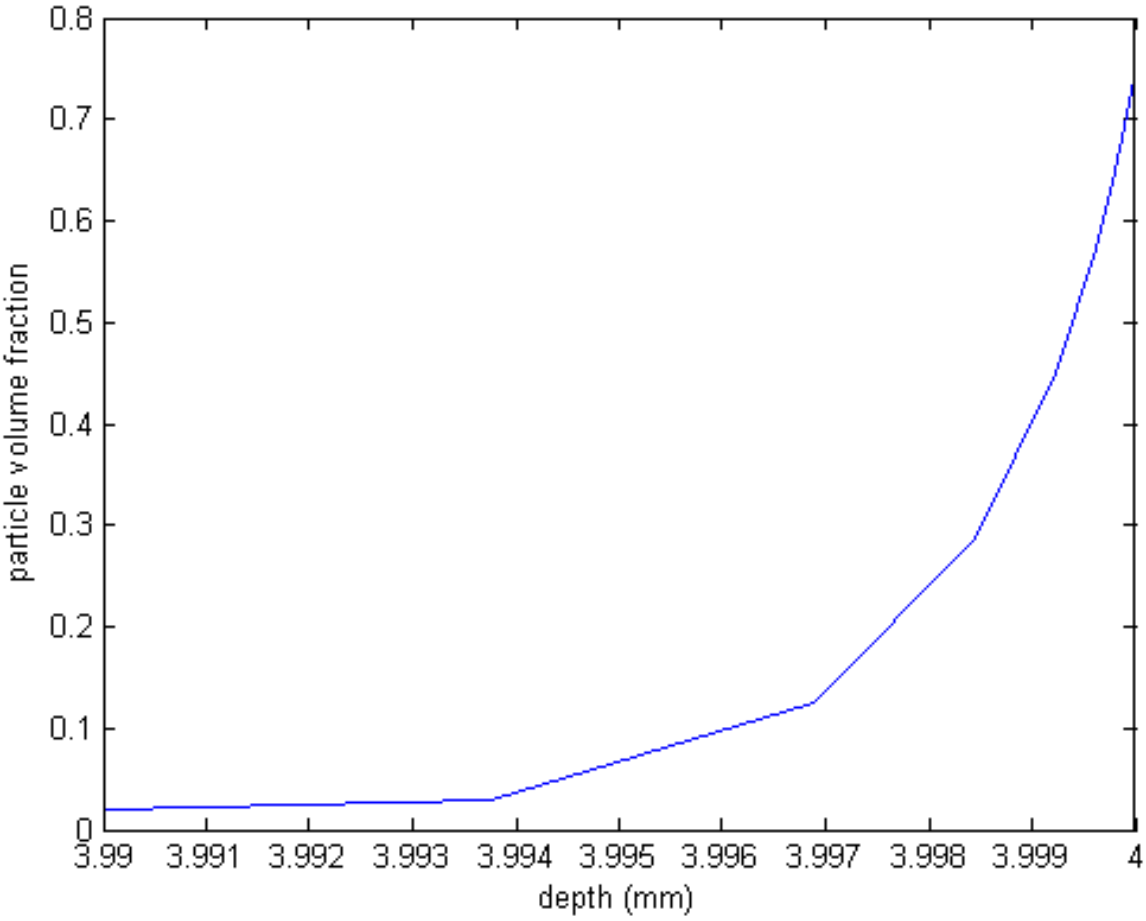

Figure 2.12: This graph shows the steady state particle concentration increase towards the membrane (depth 4mm), half way up the membrane. This illustrates the concentration polarisation.

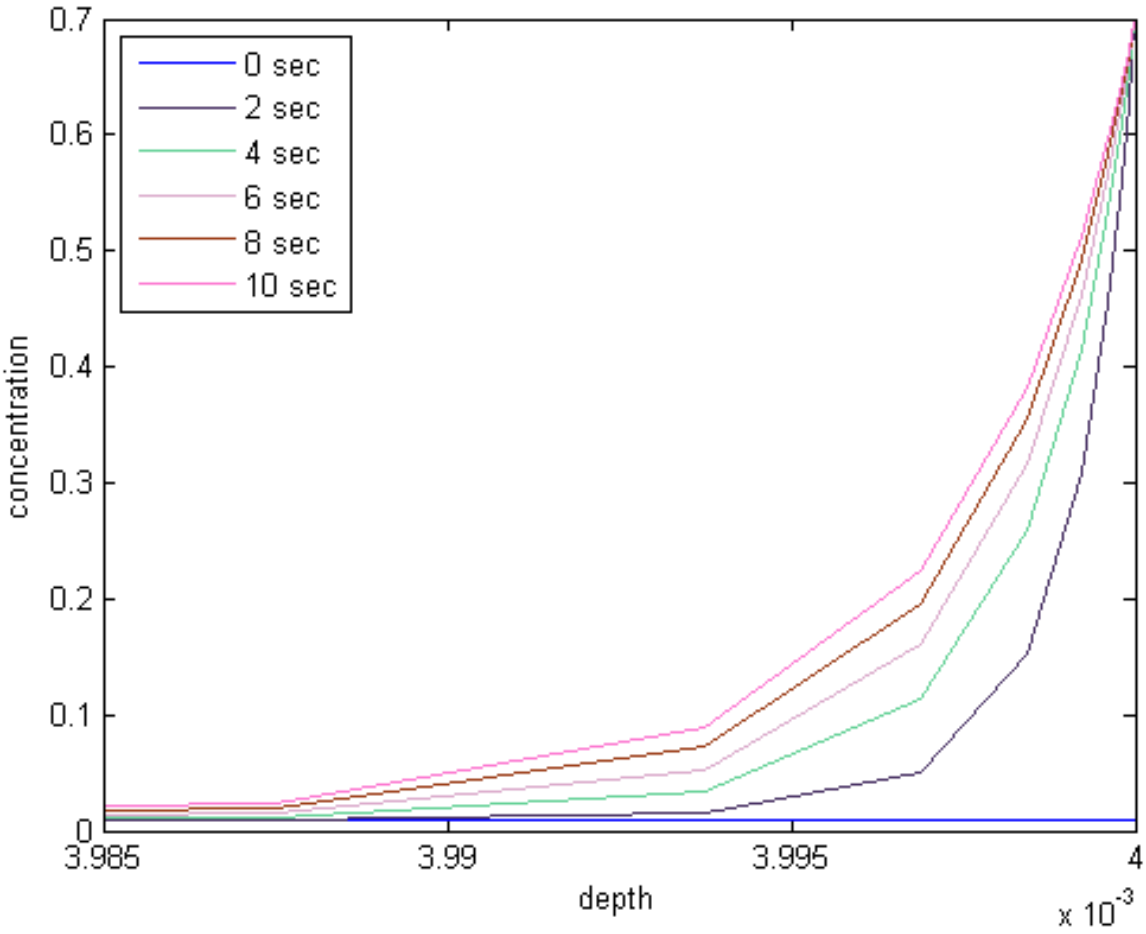

Figure 2.13: Boundary layer development with respect to the simulation time.

$$a_{min} = 2.55\sqrt[3]{\frac{kT}{n\pi\gamma\mu}} \tag{2.39}$$

Given Boltzmann constant k, temperature $T = 290K$, drag on spheres constant $n = 6$, shear rate $\gamma = 100s^{-1}$, permeate viscosity $\mu = 0.001Pa.s$, we find $a_{min} = 0.15\mu m$. The strong coupling of Diffusivity and flux is an inevitable result of the membrane wall boundary conditions. Clearly for larger Diffusivity the transport of particles away from the membrane will be greater, resulting in less resistance and higher fluxes.

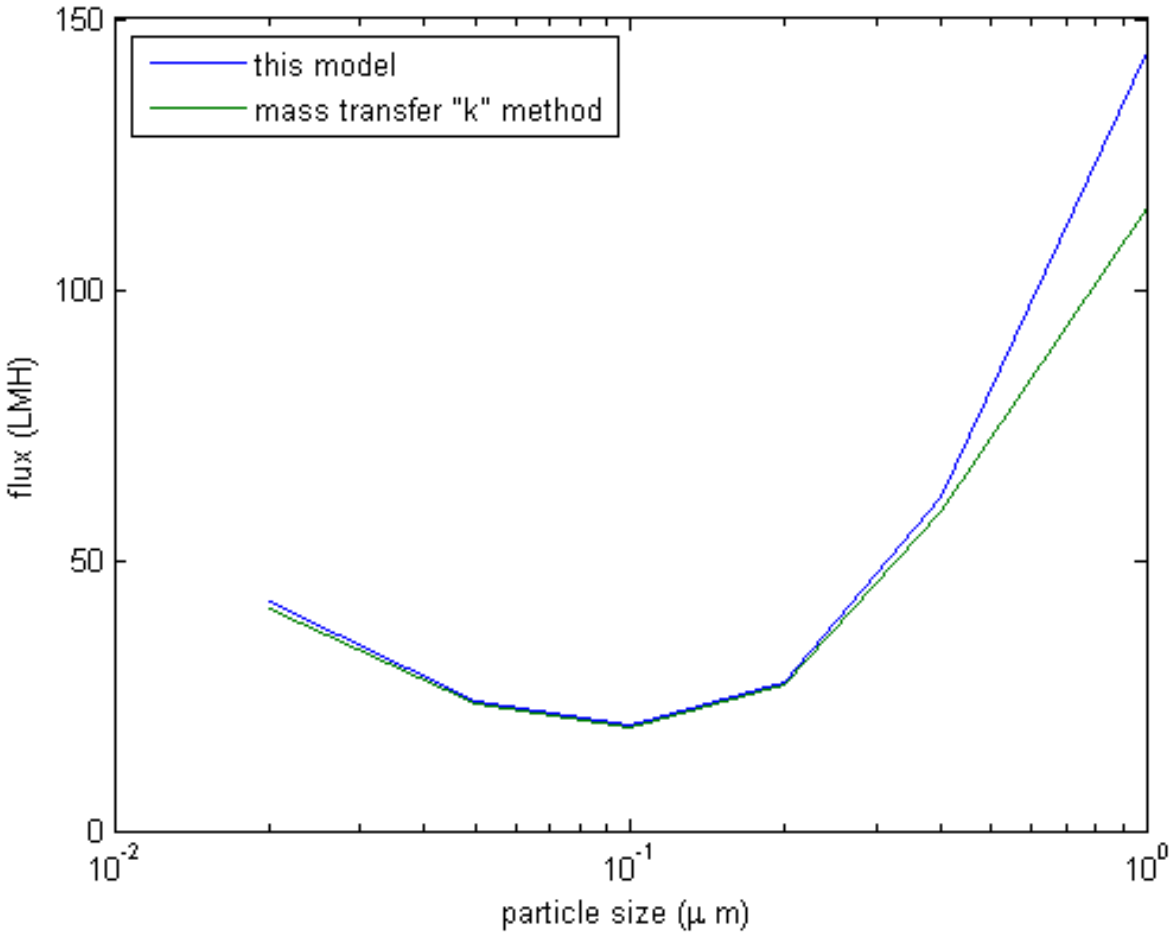

Figure 2.14: Steady state flux variation with respect to particle size. Excellent correlation is found in the ultrafiltration regime, deteriorating for larger particles.

At below the cake layer forming pressure, the variation of the boundary layer with particle size can be analysed. Figure 2.15 shows the boundary layer for three different particle sizes in the no cake layer regime. The larger particle size boundary layer has higher concentration.

This is due to the result that larger particles have less surface area for a given volume than smaller particles. As such there is less resistance due to drag on the surface which results in the more fully developed boundary layer. Larger particles will therefore form cake layers at lower pressures than smaller particles whose greater surface area makes the boundary layer resistance more significant. Equation 1.20 shows that the resistance is inversely proportional to the square of the particle diameter. So for a given particle volume a halving of the particle diameter will result in an 4-fold increase in resistance.

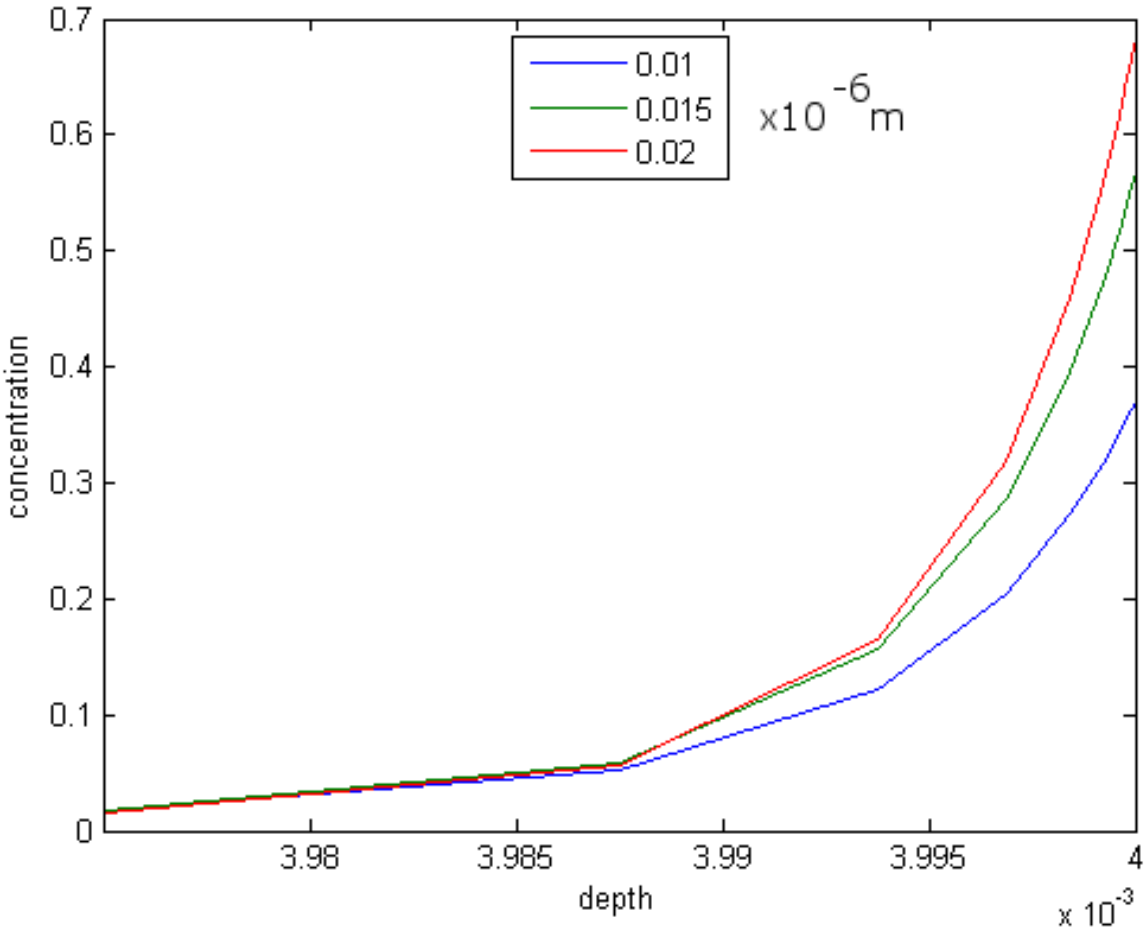

Figure 2.15: Boundary layer development for different particle sizes, no cake layer development.

Figure 2.16 shows boundary layers where the maximum concentration has been reached at the membrane surface and the cake layer has started to form. Here we see the effect of the diffusivity's relationship with particle size. As discussed above at $d_p = 0.2\mu m$ the diffusivity is at a minimum. This will result in less particle transport away from the membrane resulting

in lower concentration in the boundary layer and a steeper gradient at the membrane. As found by the solution of equation 2.24. For the smaller particles the diffusivity is greater resulting in fatter boundary layers and a shallower gradient at the membrane surface.

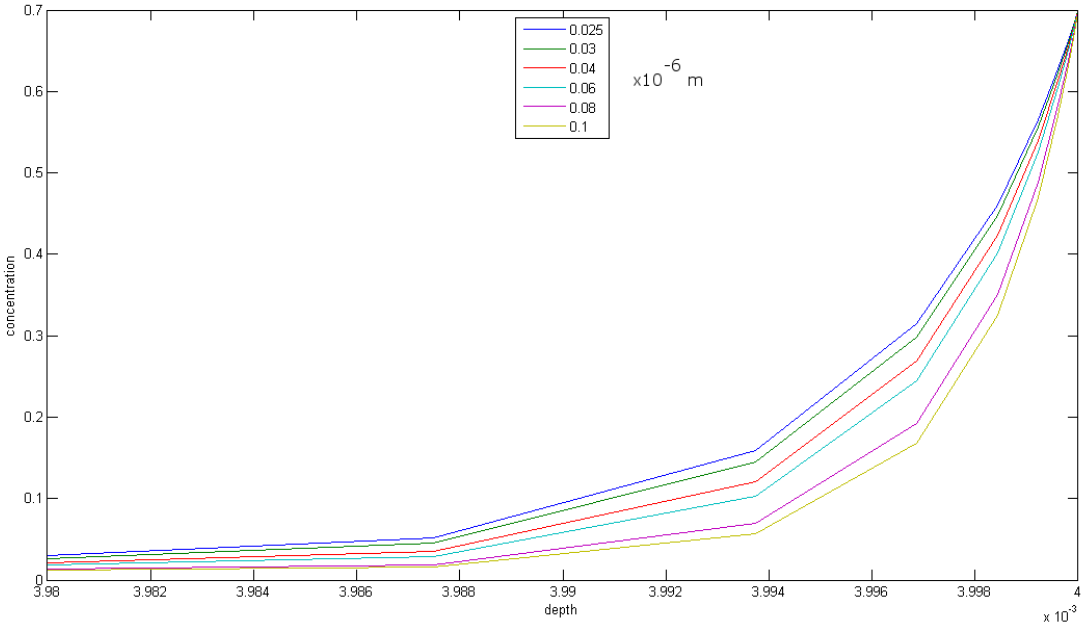

Figure 2.16: When the cake layer has formed the boundary layer development for different particle diameters has a different nature. It undergoes a thickening after the max concentration has been reached. It can be seen that the smaller particle sizes have a higher concentration in the boundary layer.

Figure 2.17 illustrates the relative strength of the membrane, boundary layer, and cake resistances. The membrane resistance is constant throughout by definition. The particle sizes shown occupy the smaller particle size microfiltration and larger particle ultrafiltration. In this region there is clear interplay between resistance types. At the larger particle sizes the cake layer reisistance becomes dominant and the boundary layer resistance is insignificant, at the smaller end the cake layer is not formed and the boundary layer is significant. The boundary layer resistance is lower at 0.01 microns than 0.02 as the diffusivity is higher which results in thinner boundary layers as discussed above. As the particle size increases to 0.02 microns the diffusivity increases resulting in larger boundary layer resistance, despite the lower surface area for drag. The resistance of the boundary layer is maximal at the largest particle

size for which the cake layer does not form, after this, the reduction in surface drag area and the growth of the cake layer resisistance makes the boundary layer resistance relatively small.

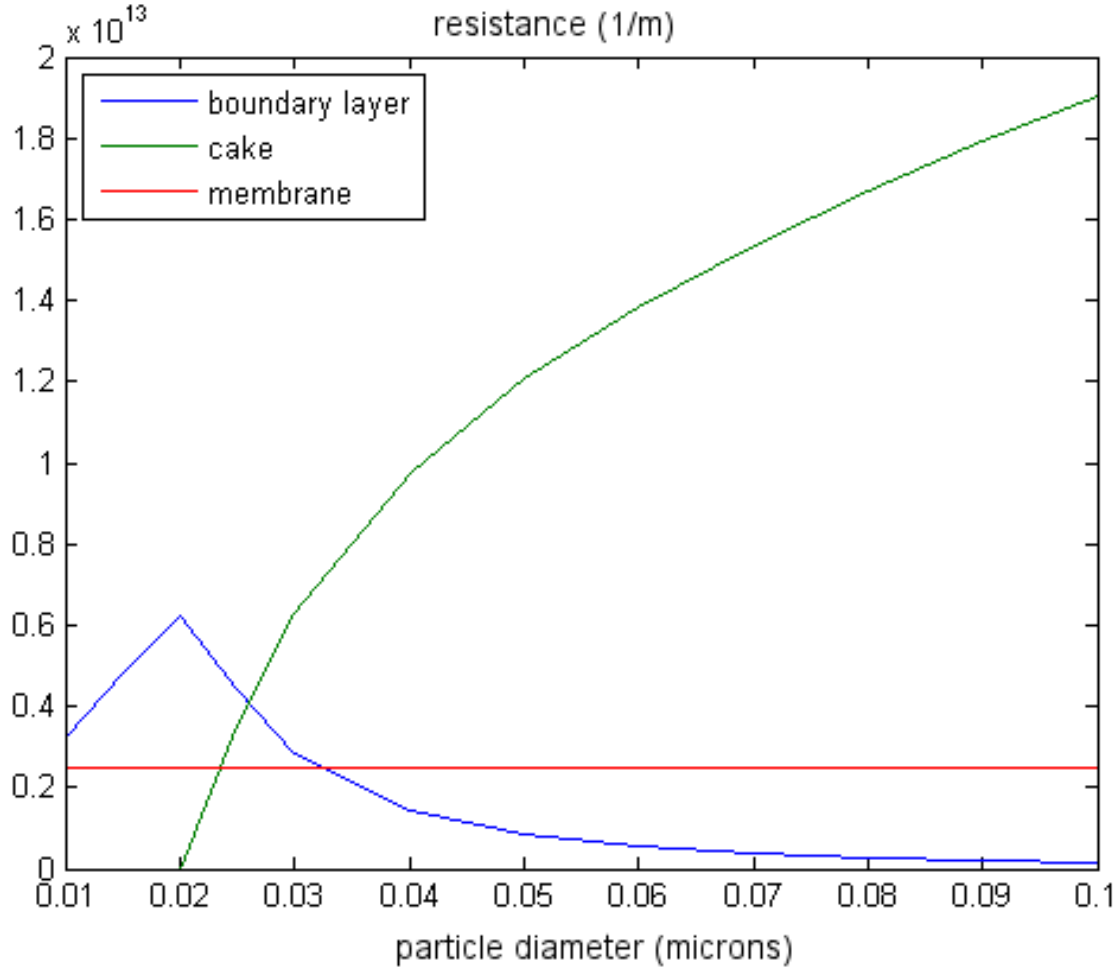

Figure 2.17: Resistance of the membrane, the boundary and cake layers with respect to particle size.

2.9.5 Convergence

Figure 2.18 compares the mesh against the calculated flux. The cell number is the inverse of the cell width, and indicates the cell density and how refined the mesh is. For coarser mesh sizes the flux is higher. As the mesh is refined however the flux starts to reduce and converge asymptotically. It is important that the results are mesh independent. Therefore the mesh must be sufficiently refined to ensure this. In these results the cell number is typically greater than 40 where the influence of the mesh is negligible.

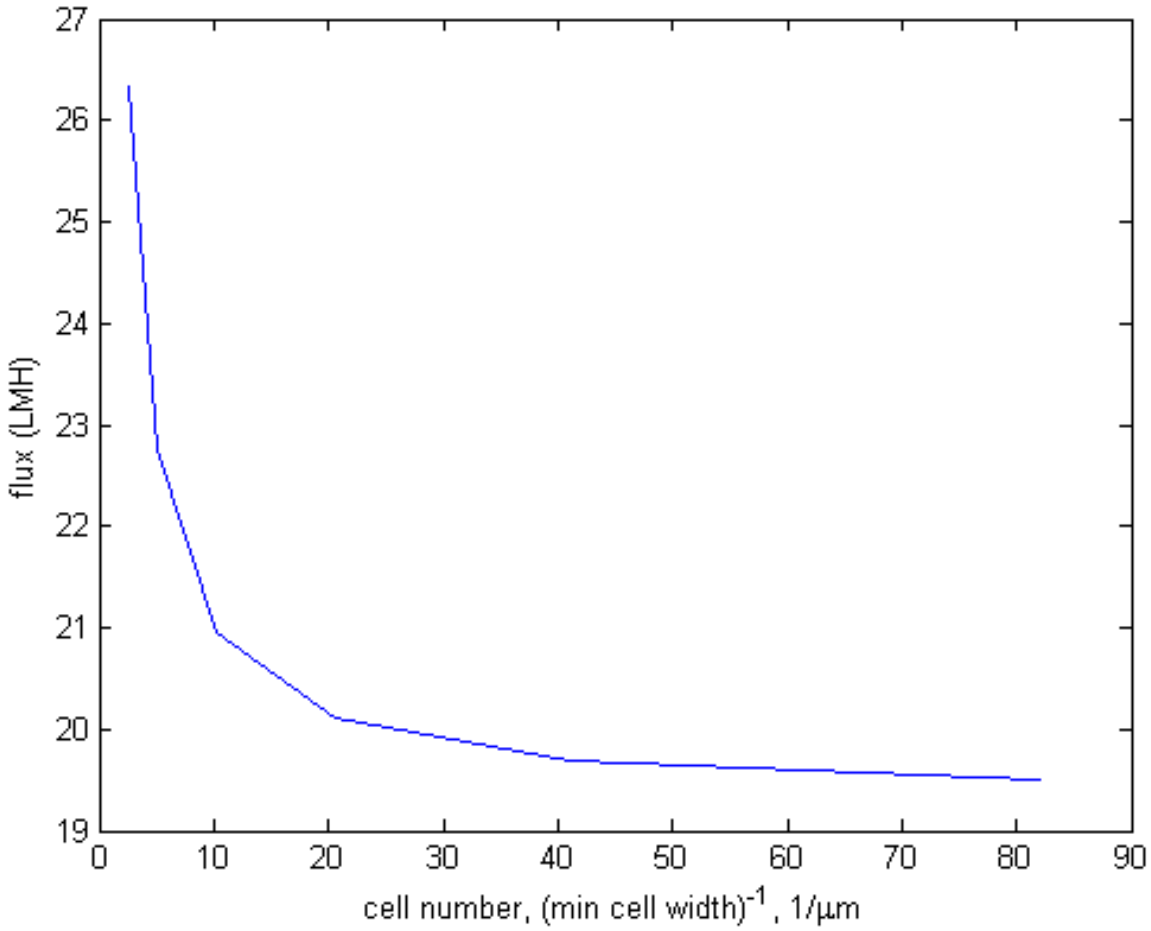

Figure 2.18: The convergence of the results are checked against the mesh. As the cell size decreases and the number of cells increases the flux converges to an asymptotic value.

Figure 2.19 shows the flux convergence against time. As the flux convects particles towards the membrane, concentration polarisation begins to occur and the flux decreases. We see the flux decline develops very quickly. As discussed in the above section the boundary layer develops quickly, hence the associated resistance and cake formation will also. As time progresses the diffusion and increased resistance resulting from the particle build up toward the membrane, will balance out the convection for a given flux and an equilibrium will occur. The time in which this equilibrium is established depends on the operating conditions. Typically for higher flux set ups where there is more fouling control, the equilibrium will occur more quickly. Whereas for lower flux conditions the balance can take longer to appear. Naturally in such circumstance in which the bulk concentration is the same as the wall concentration the flux tend towards zeros, but as time tends to infinity so the balance may not be established. In the flux calculations where the bubble is present the flux enhancement will be used as this will typically achieve a steady state result in a reasonable time. The flux enhancement is the increase in flux compared to the stagnant flow flux.

2.10 Summary

The model provides a method for calculation of flux performance in membrane filtration. Given the decoupling of the liquid and particle phases and the refinement of the mesh the model can allow for any particle size or flow field. The method of solving the convection-diffusion equation also ensures time convergence when a suitable time step is chosen. The only inputs the model requires are the flow field and the particle size, permeate viscosity and temperature along with the membrane resistance and the size of the domain. Note in this work the permeate viscosity and temperature are kept constant. The model is clear in using well established fundamental principles in developing a solution for the flux.

This represents an advancement on previous models both analytical and numerical. Correlation models rely on correlations and assumptions on the particle boundary layer size, to determine the mass transfer coefficient. These models only use the shear at the surface to determine the mass transfer coefficient. These models also require steady shear conditions at the wall to allow for analytic integration of the convection diffusion balance, in particular that the flux is constant in the domain. This requires a fully developed steady flow which in most cases will not be present. Analytical models require the flow field to be sufficiently simple to

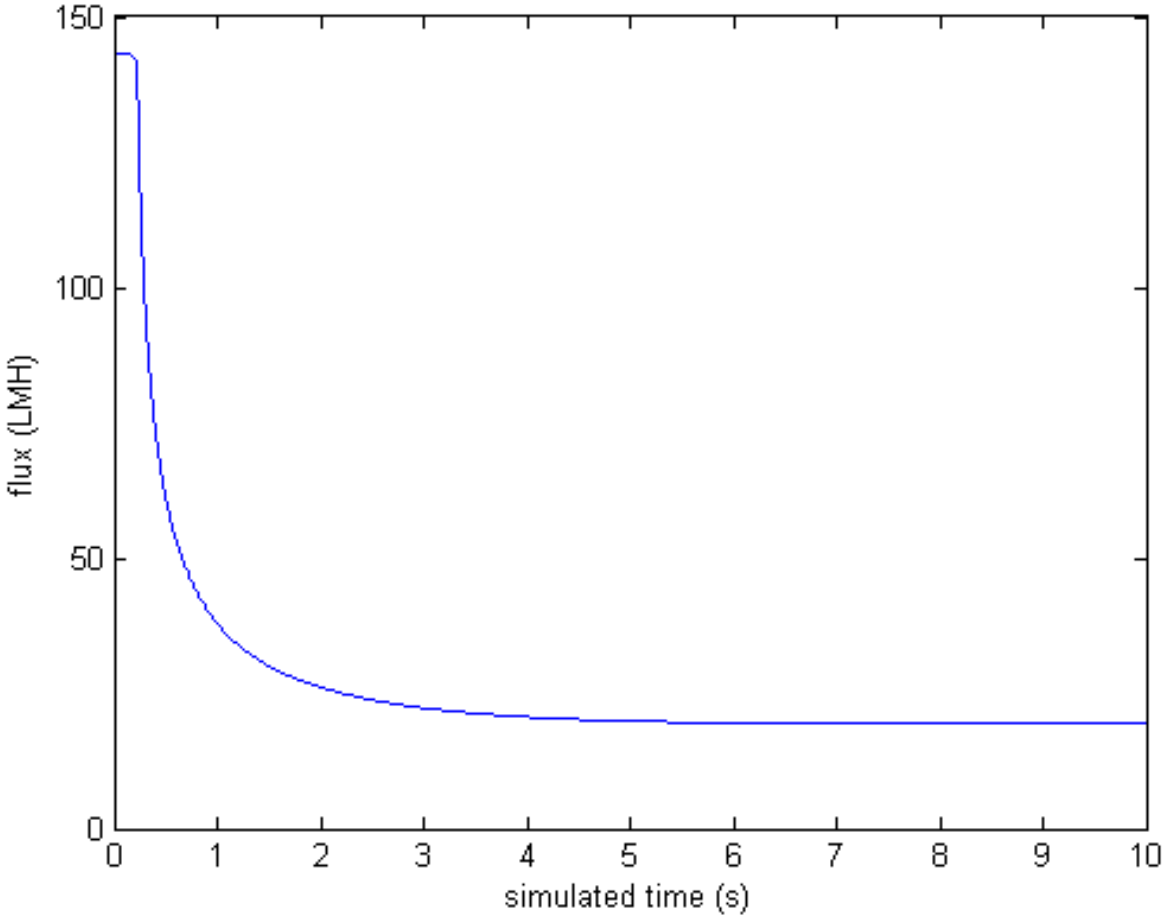

Figure 2.19: The decline in flux with respect to time. Here the flux reaches steady state after 6 seconds with the flux settling at 19.4 LMH. Although for low flux high resistance calculations the steady state flux is not found so quickly. Hence in the subsequent multiphase chapter the flux enhancement is used as this describes both the increase in performance and converges more readily.

permit solution, which would not be suitable for more complicated multiphase systems which we will introduce later. Numerical models using a resistance model have ignored analysis of the boundary layer and do not cater for the different length scales by mesh refinement [29]. The flow field is assumed to be sufficiently small to allow for a reasonable mesh number to calculate the particle effect too. The actual boundary layer size and affects are not calculated.

The model is shown to compare well with the theoretical results for different particle variables and flow velocities and operating conditions of the system. The theory based on shear at the membrane surface will only employ the concentration at the membrane. It does not account for the development of the cake and boundary layer, which provides a more detailed look at the flux. For example, we see how the old theories predicted flux flattens out very sharply to the limiting flux when maximum wall concentration is reached. However, the effect of the sharp changes in cake resistance with respect to transmembrane pressure means this will occur more gradually. Previous work does not consider changes in shape of the boundary layer after the maximum wall concentration is reached. It assumes that upon this maximum being reached the boundary layer will be unchanged. In reality, of course, we can expect a thickening of the boundary layer for a transitional period as the transmembrane pressure is increased.

3 CFD Modelling of Gas-Liquid Flow Between Two Parallel Flat Plates

3.1 Introduction

Compared to slug flow in pipes, or Taylor bubbles, the gas-liquid hydrodynamics between two flat plates has been the subject of much less research. The difficulties arise that unlike in tubular flow where the bubble is constrained radially and is only free to move in the direction of the pipe, the slug between two plates is free to move both vertically and horizontally so has two degrees of freedom. Therefore, whilst the typical tubular set up permits the assumption of axisymmetry, no such simplification is permitted here.

Instructive results about the behaviour of the bubble may be obtained by 2 dimensional analysis in both the plane parallel to the flat sheets and the vertical plane perpendicular to the flat sheets. The former can provide an insight to the movement of the bubble and the latter to the hydrodynamics near the wall for the purposes of mass transfer. Analysis of these methods are undertaken in the following chapter.

Shear resulting from the introduction of a gas phase into systems using membrane bioreactors plays a key role in the enhancement of permeate flux due to the gas phase. The flow of gas bubbles between two flat membrane modules is modelled. To calculate the shear across the entire plane is not possible in 2-D as there is no velocity gradient parallel to the wall. Instead the problem is approached taking a cross-section of the bubble in the plane perpendicular to the wall. In this way the shear along a vertical line in the wall is calculated. The cross-section is taken through the centre of the bubble where the flow through the plane will be minimal due to symmetry and most apt for a 2-D analysis, as shown in Figure 3.1.

Of course both these methods are limited as they will not provide the full picture, resulting in a somewhat qualitative behaviour. To get the complete hydrodynamics a 3 dimensional model is required, this will provide both the bubble behaviour and the induced flow near the wall for mass transfer analysis. However, with a full 3 dimensional analysis the computational load becomes significant. This additional computational time reduces the number of results that can be obtained in the available time.

Single bubbles slugged between two flat sheet membranes are to be investigated. This is illustrated by Figure 3.2.The bubble is modelled using computational fluid dynamics (CFD).

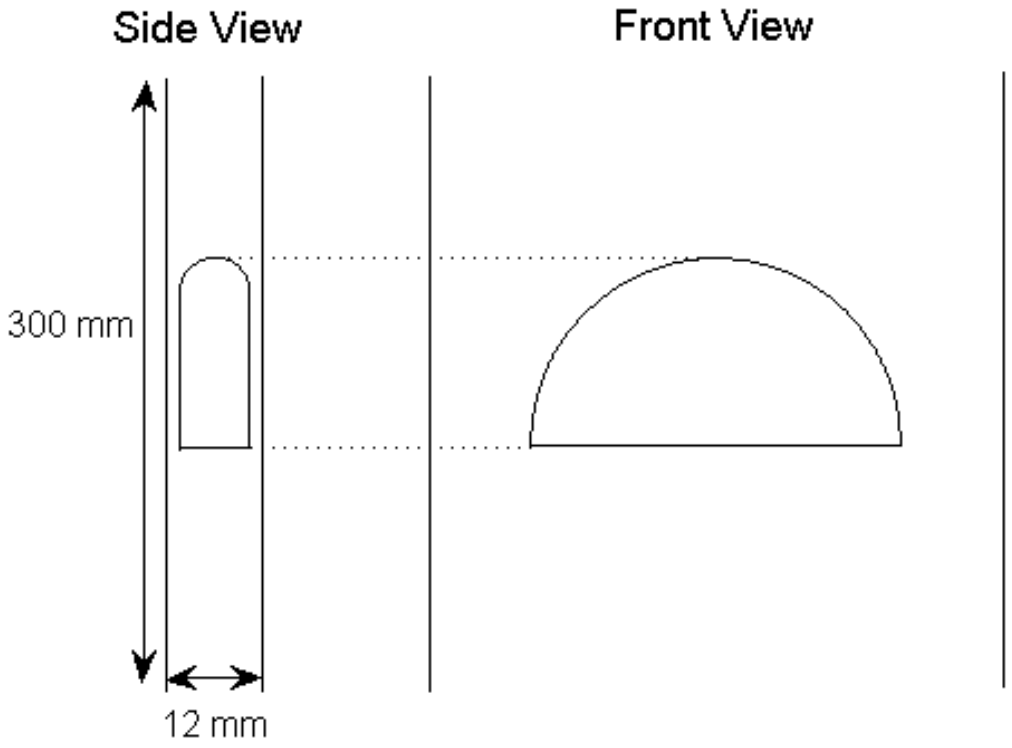

Figure 3.1: Schematic showing the modelled flows in 2D. The shear calculation on the left, which is a plane through the centre of the bubble shown right which is used for the dynamics calculation. The modelled domain is width x height, 12mm x 300mm and 100mm x 200mm, for the side and front calculation respectively.

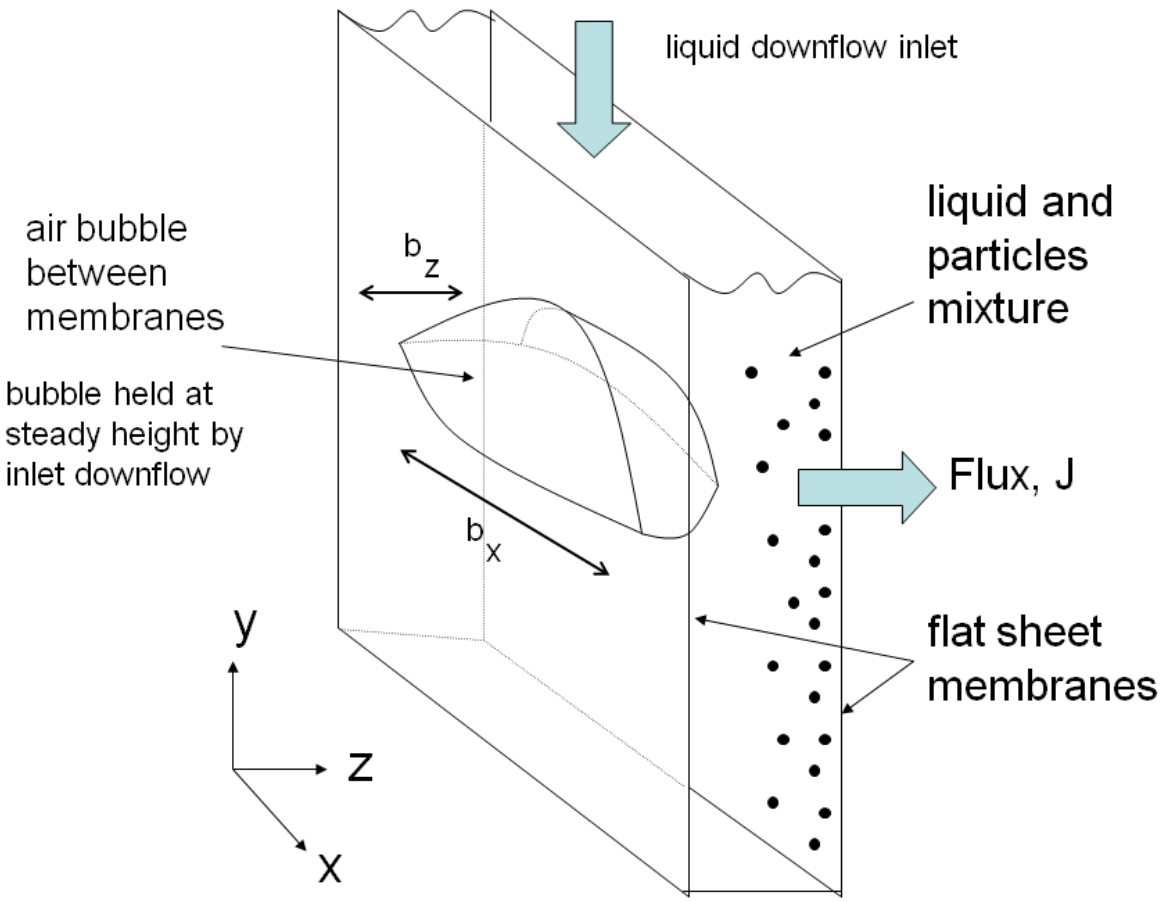

Figure 3.2: Schematic of a single bubble slugged between two flat sheet membranes modelled in 3D. The permeate flux is indicated. Presence of particles shown for illustration purposes.

The Volume of fluid (VOF) method is used to calculate the bubble shape and flow. The gas phase is taken to be air and the liquid phase water at 20^oC. The bubble is modelled as steady by applying a downward liquid velocity component equal to the bubble's rise velocity. In this way, the bubble's position is held stationary.

3.2 Governing Equations

Equation 3.1 is the general equation for the conservation of momentum, where ρ is the fluid density, p is the pressure, $\underline{\underline{\tau}}$ is the stress tensor. $\frac{D}{Dt}$ is the total derivative defined by, $\frac{D}{Dt} = \frac{\partial}{\partial t} + (\underline{v}.\nabla)$. This derivative groups the inertial forces, unsteady acceleration and convective acceleration. The terms on the right of the equation are the static surface forces, given by the pressure gradient, the dynamic surface forces, given by shear, and the body forces respectively.

$$\rho \frac{D\underline{v}}{Dt} = -\nabla p + \nabla.\underline{\underline{\tau}} + \rho \underline{g} \tag{3.1}$$

The body forces employed here are limited to gravity. If x is the horizontal and y is the vertical component, then for a tube at inclination θ to the vertical we have $g_x = g \sin\theta$ and $g_y = -g \cos\theta$ where g is the magnitude of the gravitational acceleration. For vertical tubes ($\theta = 0$) this reduces to $g_x = 0$ and $g_y = -g$.

The conservation of mass is given by equation 3.2. The equation accounts for compressibility effects, for incompressible flow this reduces to $\nabla.\underline{v} = 0$.

$$\frac{\partial \rho}{\partial t} + \nabla.(\rho \underline{v}) = 0 \tag{3.2}$$

In this form the above equations cannot be solved analytically. Computational fluid dynamics solves these equations numerically by use of a sufficiently fine mesh. The relevant gradients are assumed to be constant within each cell whose size is defined by the mesh, hence a fine mesh is required for this to be valid. The governing equations are thus solved within each small cell. The solution for the flow through a cell feed into its neighbouring cells, an iterative method is required for the fluxes to match. At the edge of the overall flow boundary conditions are required to provide closure.

3.3 Multiphase Volume Of Fluid (VOF) Method

The commercial CFD package FLUENT is used to solve the governing equations [86]. The volume of fluid (VOF) method is used to model the gas-liquid flow as the location of the interface between the gas and liquid is not known. The VOF method calculates the properties of the fluid based on the volume fraction of the phases within a cell. The volume fraction of the gas and liquid phase in a particular cell is denoted by α_G and α_L respectively.

The VOF method is an effective Lagrangian method of calculating the interface between two different phases, i.e. gas and liquid. However, this is limited to the case where number of cells containing both phases is relatively small. As in the case of a single bubble. Where multiple bubble swarms are considered and a large number of cells of both phases exist the VOF method is not as effective due to the computational workload. In these cases Eulerian simulations are likely to be more effective, although Eulerian methods will not provide the same detailed interface tracking and rely on simplified bubble shape and size to provide more homogeneous results.

The position of the interface between the gas and liquid phases is found by the solution of a continuity equation for the volume fraction of one of the phases [87]. It is assumed that individually both phases are incompressible. For the gas phase we have

$$\frac{\partial \alpha_G}{\partial t} + \underline{v}.\nabla \alpha_G = 0, \tag{3.3}$$

the liquid phase volume fraction is found by $\alpha_G + \alpha_L = 1$. The shape of the gas liquid interface is calculated using the piecewise linear interface method (PLIC) by Youngs [88]. This allows a linear approximation to the interface within the computational cell, which is not constrained to be parallel to the grid. Like the earlier simple line interface calculation (SLIC) [89]. A review of volume tracking reconstruction methods is given by Rider et. al. [90].

The fluid properties for those cells where both phases are present are estimated for density and viscosity by equations 3.4 and 3.5 respectively.

$$\rho = \alpha_G \rho_G + \alpha_L \rho_L \tag{3.4}$$

$$\mu = \alpha_G \mu_G + \alpha_L \mu_L \tag{3.5}$$

A single momentum equation 3.6, derived from equation 3.1, is solved throughout the domain and is dependent on the volume fraction of the phases. Each phase is considered Newtonian with constant viscosity. The resulting velocity field is shared by both phases.

$$\frac{\partial}{\partial t}\left(\rho \underline{v}\right) + \nabla.\left(\rho \underline{v}\,\underline{v}\right) = -\nabla p + \nabla.\left[\mu\left(\nabla \underline{v} + \nabla \underline{v}^{T}\right)\right] + \rho \underline{g} \tag{3.6}$$

3.4 Surface Tension

Surface tension is modelled in Fluent using the continuum surface force model derived by Brackbill et al. [91]. The pressure across the interface due to surface tension is found by,

$$p_2 - p_1 = \sigma\kappa. \tag{3.7}$$

where p_1 and p_2 are the pressures in each phase either side of the interface, σ is the surface tension between the two phases and κ is the curvature of the interface.

The surface curvature is computed from local gradients in the surface normal at the interface. The surface normal, n, is defined by

$$n = \nabla \alpha_G. \tag{3.8}$$

The curvature is defined by,

$$\kappa = \nabla.\hat{n} = \frac{1}{|n|}\left[\left(\frac{n}{|n|}.\nabla\right)|n| - (\nabla.n)\right], \tag{3.9}$$

where the unit normal is given by

$$\hat{n} = \frac{n}{|n|}. \tag{3.10}$$

3.5 Boundary Conditions

The no–slip condition is assumed at the walls. To improve convergence for the side view shear calculation, the flow was analysed in a bubble steady state [92]. This is achieved by applying a downward velocity condition to the top of the domain and the side walls [41]. It is assumed the liquid phase without the bubble is stagnant. As a result, the velocity inlet profile at the top is uniform across the domain width. The velocity is equal to the bubble rise velocity rendering the bubble stationary. Whilst this affects the velocity of the liquid about the bubble, the shear is unchanged. This is due to the velocity gradient at the wall

being unaffected, a constant velocity is added throughout the profile leaving the gradient unchanged. In the moving bubble state, the central liquid above the bubble nose is pushed upwards whilst the liquid near the wall is drawn downward into the film, conserving mass flow.

The front view bubble dynamics calculation is done without the bubble held stationary by a downward flow. As a result, no slip wall conditions are applied at the base and side walls. A constant atmospheric pressure condition is applied at the top of the domain. The rise of a single bubble in stagnant liquid is modelled.

3.6 Initial Conditions

The modelled flow is unsteady with respect to time, even in the bubble steady case. Initial conditions are required for the calculation. The gas phase is patched into the domain. In the side view shear calculation, the bubble shape is given by a rectangle topped by a semi-circle. In the front view dynamics calculation, a semicircular initial shape is assumed. The initial shapes are chosen to correspond to the expected bubble shape. Other initial shapes converge to the same final shape, but more slowly. For the bubble dynamic calculation, stagnant liquid is assumed so the default zero velocity for each phase is retained. In the shear calculation, the liquid flows down past the bubble. In this case, the initial liquid phase velocity was chosen to be equal to the inlet and wall velocities throughout.

3.7 2D Results – Bubble Dynamics

3.7.1 Bubble Shape and Rise Velocity

In order to design an effective system incorporating gas sparging in flat sheet submerged membrane bioreactors, knowledge of the bubble motion and interactions are required. The shear believed to enhance flux has been discussed in previous sections. It is desirable for the bubble residency to span the bed to maximise the area enjoying the shear enhancement. The bubble behaviour is simulated using the same methods described above applied to the new geometry.

The rise behaviour of a single bubble with equivalent circular diameter of $d_e = 14.14$mm is shown in Figure 3.3. The steady state bubble rise velocity was found to be $u_b = 0.196$m/s. Compare the simulated shape with the experimental result [8] single spherical cap bubble

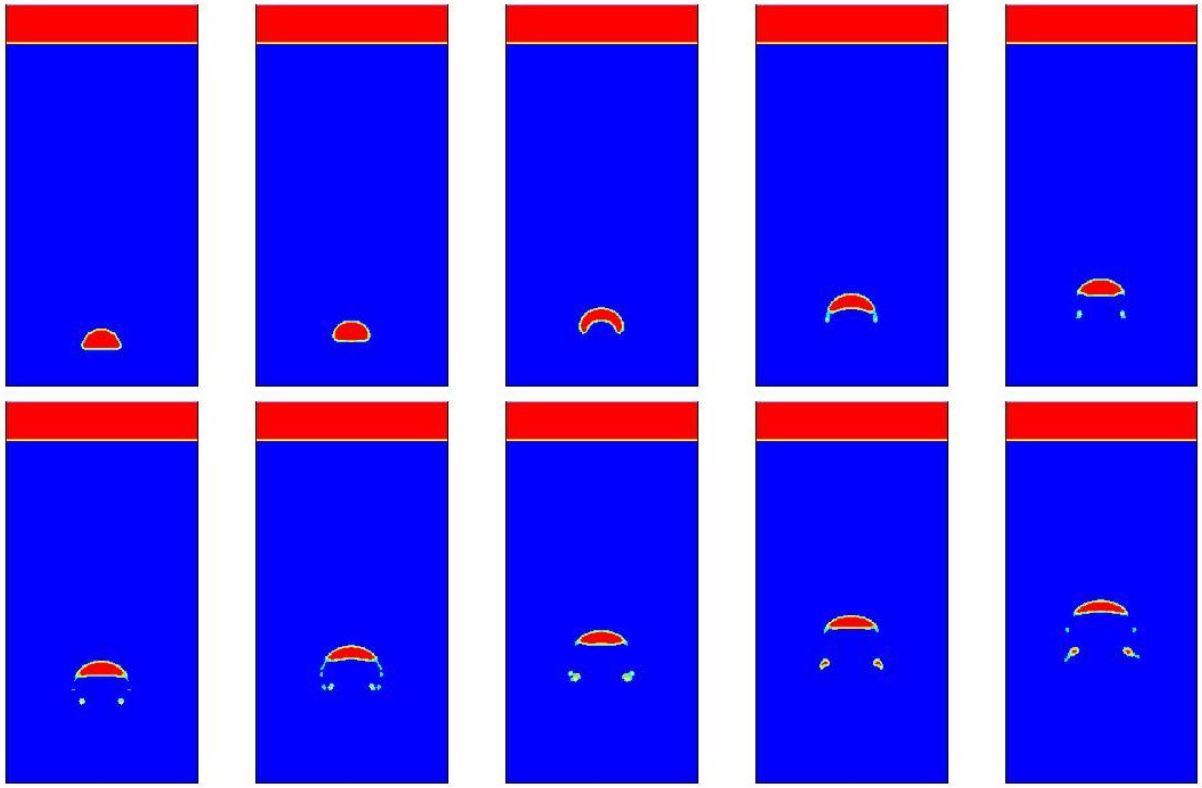

Figure 3.3: Motion of diameter, $d_e = 14.1$mm, bubble up the bed at time increments of 0.1 seconds. As the bubble is accelerating vertically, its Reynolds number will increase; the associated transition in bubble shape is well captured. The bubble has a steady state rise velocity of $u_b = 0.196$m/s, giving a Reynolds number of $Re = 2772$.

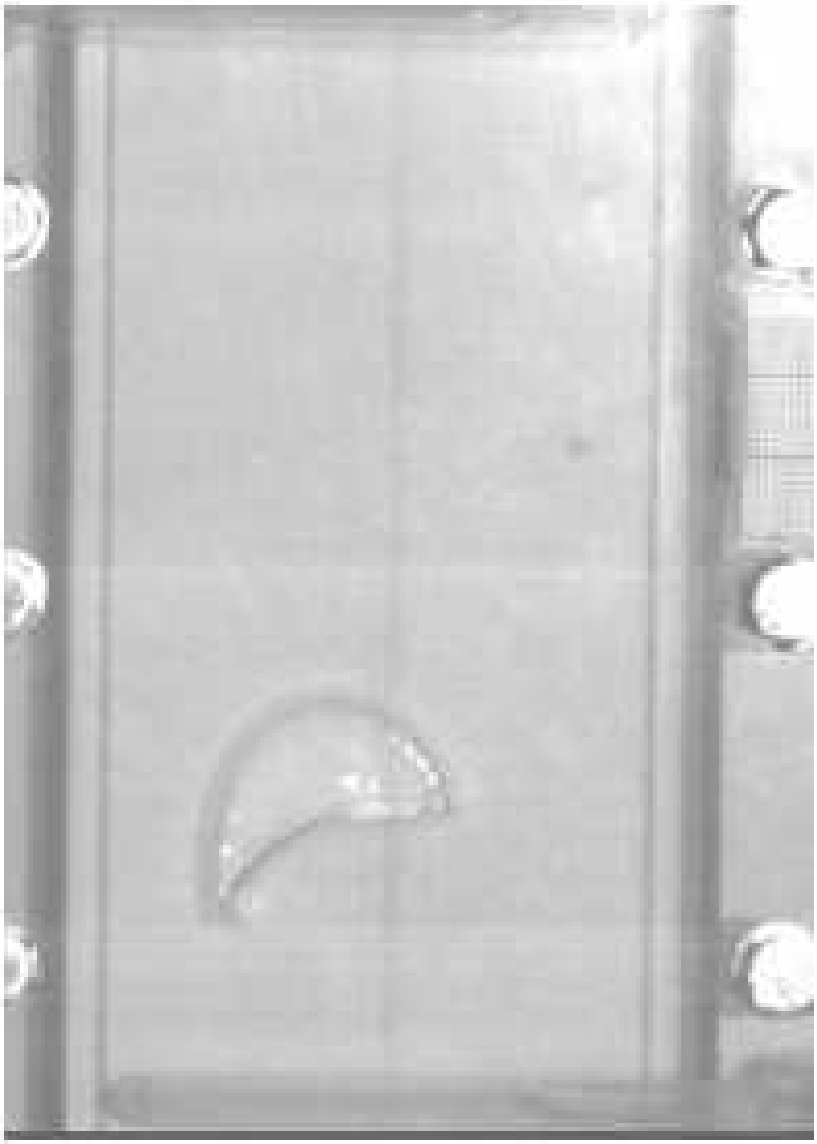

Figure 3.4: Image of single spherical cap bubble moving in a narrow gap between two parallel plates. Taken from Essemiani et. al. [8].

shown in Figure 3.4. The behaviour of bubbles rising through a surrounding fluid can be characterised in terms of dimensionless numbers which relate the properties of the flow. These are as follows. The Eotvos number relates the significance of surface tension to bouyancy forces. The Morton number is independent of the bubble size and velocity and characterises the two phase flow. The Reynolds number relates the significance of inertial to viscous forces. The values of these numbers is given below, where $\rho_{l,g}$ is the liquid and gas densities respectively, σ is the surface tension and μ_l is the liquid viscosity.

$$Eo = \frac{g\left(\rho_l - \rho_g\right) d_e^2}{\sigma}, \quad Mo = \frac{g\mu_l^4\left(\rho_l - \rho_g\right)}{\rho_l^2 \sigma^3}, \quad Re = \frac{\rho_l d_e u_b}{\mu_l} \tag{3.11}$$

For air-water flow, we have, $\rho_l = 1000\,kg/m^3$, $\rho_g = 1.25\,kg/m^3$, $\mu_l = 0.001\,Pa.s$, $\sigma = 0.072\,N/m$. Given $g = 9.81\,m/s^2$ and the bubble size and velocity given above we have, $Eo = 27.2$, $Mo = 2.625 * 10^{-11}$ or $log_{10}Mo = -10.58$, and $Re = 2772$. Figure 3.5 shows the relationship between the dimensionless numbers and bubble behaviour for 3D bubbles rising in sufficiently large volumes of surrounding fluid as to be unconstrained. We can see for a given Eotvos number how the bubble shape may change with respect to Reynolds number as it is accelerated up the bed by bouyancy forces. The bubble in Figure 3.3 reflects this transition in bubble shape. An initial semicircular guess is adopted which becomes skirted and finally spherical cap as it develops. Figure 3.5 can also be used to estimate the rise velocity for a given bubble, as the Reynolds number is a function of the Morton and Eotvos number, which can be calculated from the physical properties. The bubble size and fluid properties are known which provide the Eotvos and Morton numbers. The Reynolds number at which these two meet may then be determined graphically, which in turn will give the bubble rise velocity. Given $Eo = 27.2$ and $log_{10}Mo = -10.58$ we find $Re = 10^{3.46} = 2884$ this compares well with the simulated Reynolds number, $Re = 2772$.

The method for determining the simulated rise velocity is shown in Figure 3.6 for a bubble with an equivalent diameter, $d_e = 33$mm rising in a 100mm wide bed. When the bubble appears to have attained its steady state rise velocity, the average gradient of the position of the nose with respect to time is found. Here, the calculated simulated rise velocity gives a Reynolds number, $Re = 7067$. The Clift chart graphical method gives a Reynolds number for this bubble diameter of $Re = 8171$. The discrepancy likely results from the increased influence of the no slip condition at the walls restricting flow. The larger bubble results in an

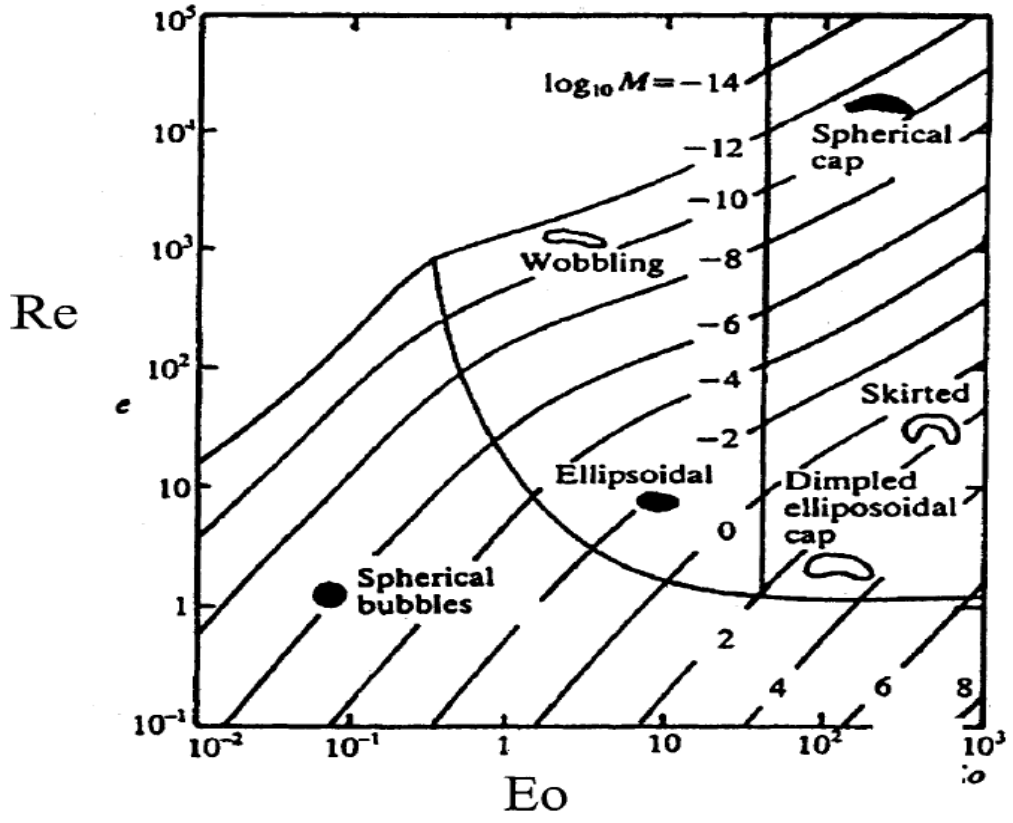

Figure 3.5: Chart showing bubble characteristics with respect to the dimensionless Eotvos, Morton and Reynolds numbers. Taken from Clift et. al. [9].

increased bubble diameter to bed width ratio.

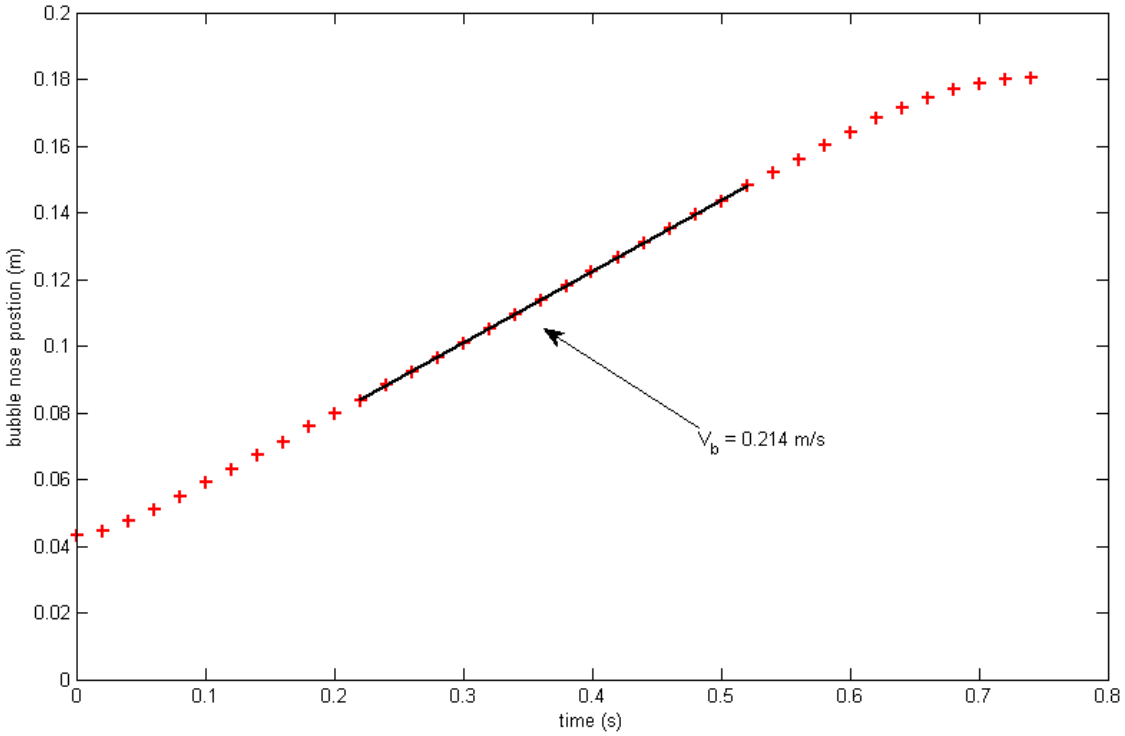

Figure 3.6: Method for determining the bubble rise velocity up the bed. Bubble equivalent diameter, $d_e = 33$mm.

3.7.2 Bubble Interaction

The interaction between bubbles in one-dimensional flow, i.e. through axisymmetric pipes, is well described by Wallis [93]. Here, we shall extend this to 2D planar flow. The interaction between two inline bubbles of the same size is shown in Figure 3.8. The two bubbles develop in a similar manner to the single bubble, but the trailing bubble is drawn into the wake of the lead bubble. The low pressure wake of the lead bubble increases the rise velocity of the trailing bubble. After 0.6 seconds, the bubbles start to coalesce. Surface tension forces will drive the formation of a new single bubble. Surface tension will seek to minimise the surface area of the interface between gas and liquid which is achieved by a single bubble formation. This is achieved by the pressure gradients in the presence of the interfacial curvature, as in equation 3.7. Excessive curvature will cause a pressure gradient coalescing the two phases.

$d_e, [mm]$	$u_{b,sim}, [m/s]$	Re_{sim}	Re_{exp}
5	0.168	840	924
14.1	0.196	2772	2884
21.2	0.208	4412	4771
33	0.214	7067	8171

Figure 3.7: Comparison of simulated rise velocities with experimental results.

After 0.8 seconds, the new single bubble forms, again taking spherical cap shape. The new bubble will behave as a single larger bubble, with gas volume roughly conserved. This would lead to an equivalent diameter, $d_e = 20$mm. However, the bubble will be slightly smaller than that due to the shedding of smaller bubbles from the main bubbles. It is argued that the shape of the bubble governed by surface tension forces is unable to respond sufficiently quickly to the viscous shear experienced on the cap of the rising bubble. This leads to 'bursting' where the skirts of gas are drawn down below the bubble encircling the wake region [94]. The instability of this structure will lead to gas being shed in the form of smaller bubbles. The results compare well with work on bubble interactions by Boulton–Stone et. al. [95].

With reference to Figure 3.5, this phenomena will be clearer for larger Eotvos number bubbles. Figure 3.9 shows the CFD simulation of a bubble with Eotvos number, $Eo = 61.2$. Smaller bubbles are torn off the main bubble by viscous shear. These bubbles encircle the wake region below. Work with larger bubbles ($Eo > 100$) is required to see if stable skirts can be simulated.

The coalescence of bubbles described above may be detrimental to the efficacy of the shear profile along the membrane wall. The turbulent wake region is believed to play a key role in the enhancement mechanism. However, the coalescence of bubbles will reduce the number of wake regions and therefore the span of this property across the wall. To maintain an optimal bubble residency will require further knowledge of bubble behaviour with respect to the gas sparging conditions.

3.7.3 Sparging Frequency

The previous CFD work on bubble interactions has focused on the behaviour when a number of fixed bubbles are placed in the bed at a fixed time spacing. Adding bubbles at a fixed

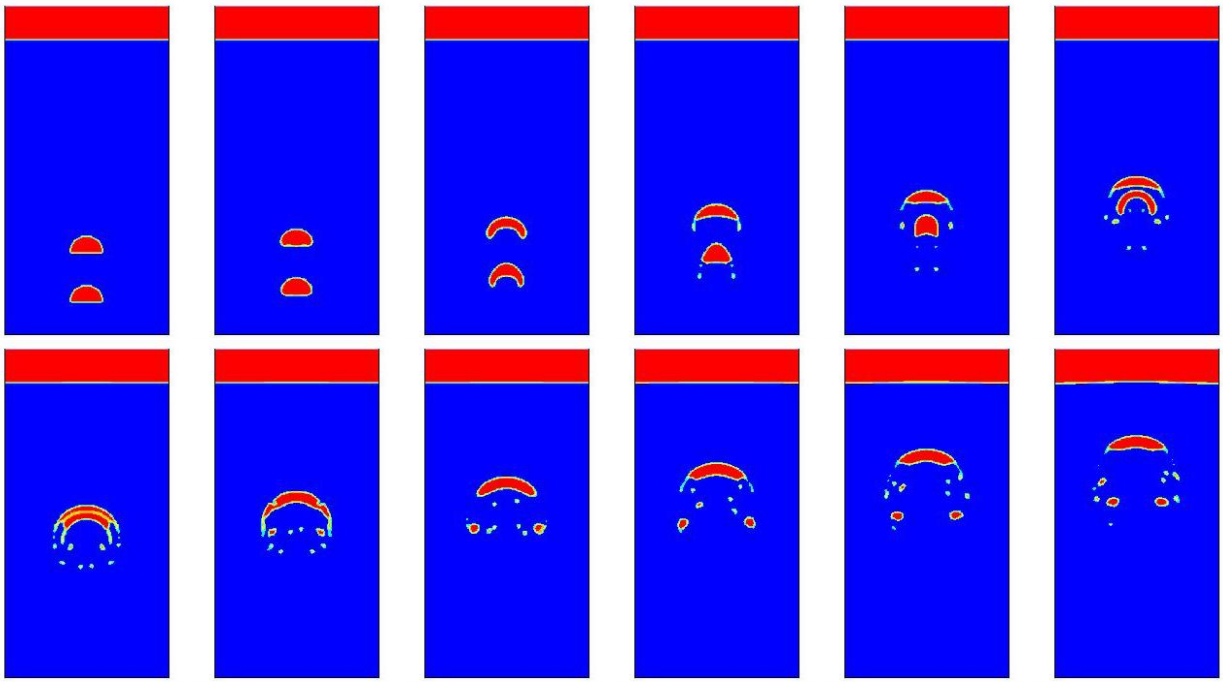

Figure 3.8: The interaction of two vertically inline bubbles of equivalent diameter, $d_e = 14.1$mm. The lower bubble is drawn into the low pressure wake behind the lead bubble, whereupon they coalesce into one larger bubble.

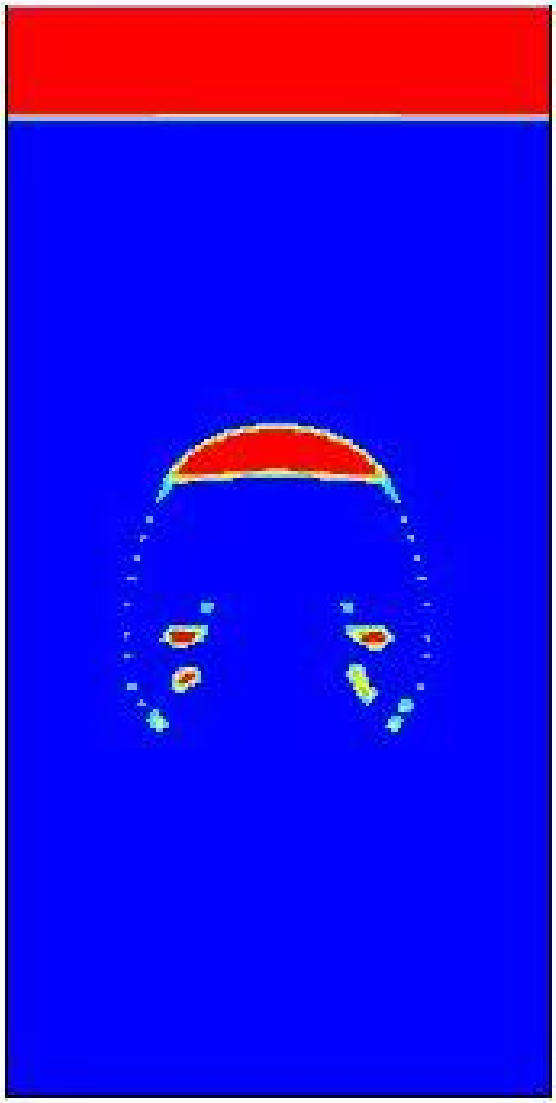

Figure 3.9: Smaller bubbles torn from main bubble with Eotvos number, $Eo = 61.2$. Note how these bubbles encircle and describe the wake region below the main bubble.

frequency, like a gas sparger, is developed here. A new bubble is regularly added after a fixed amount of time. The positions of the nose and tail of multiple bubbles along the centre line at a gas sparging frequency of 5 bubbles/second is shown in Figure 3.10 each bubble has an initial equivalent diamter, $d_e = 14.14$mm.

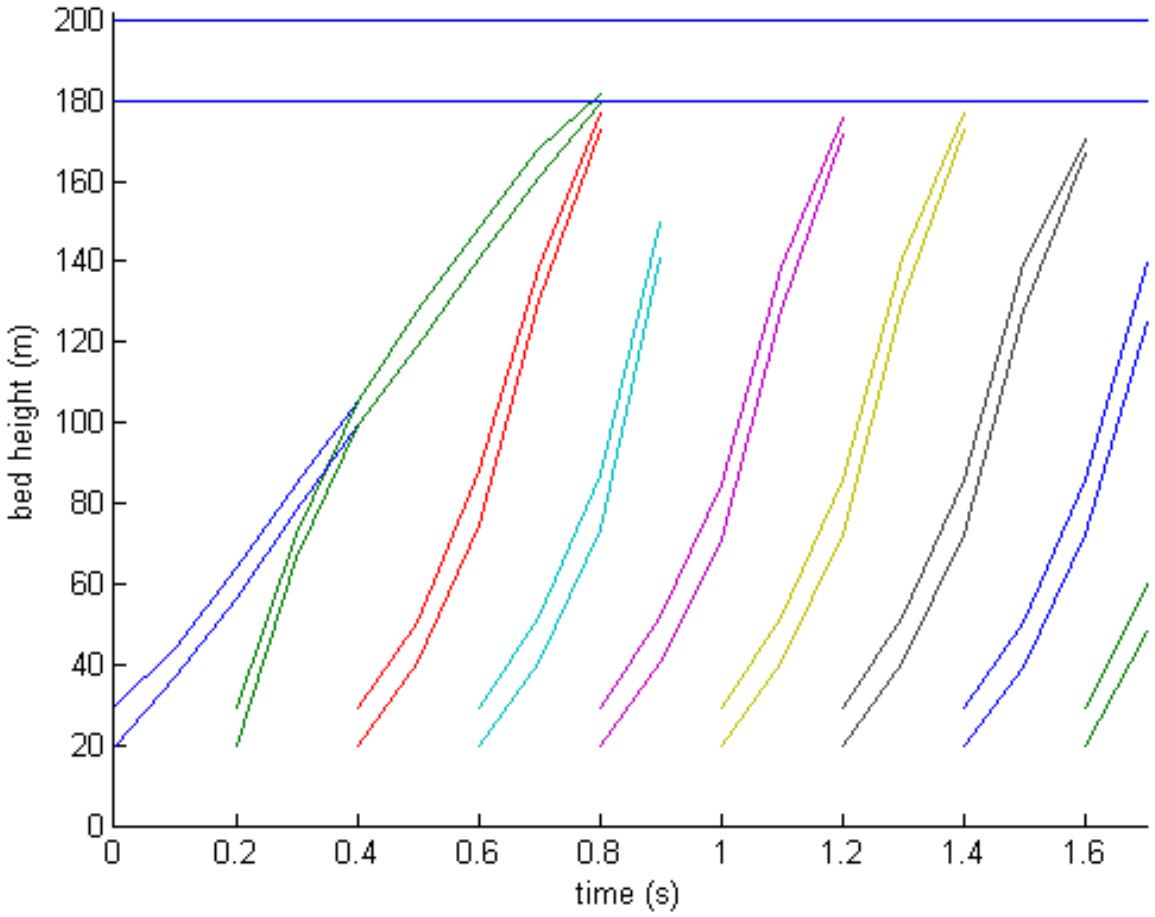

Figure 3.10: The bubble nose and tail paths up the centre line of the bed are plotted at a sparging frequency of 5 bubbles per second. The effects of the bubble interactions appear to reach a steady state. The attraction of a given bubble to its lead bubble is matched by that bubbles own attraction to its leader. The steady state bubble rise velocity exceeds the single bubble rise velocity.

We see the second bubble is quickly drawn into the first bubble. This increases the distance between the second and third bubble reducing the strength of the interaction between the two. As a result the third bubble does not meet the bubble formed from the first and second bubble until the top of the bed. After this a steady state appears to be reached. The attraction

of one bubble to the trailing bubble is matched by the bubbles own attraction to its lead bubble. A higher average rise velocity in the later bubbles results. At a steady state position ($t = 1.3$s) there are two substantial bubbles in the bed. They occupy about 12% of the centre line region. If the wake region is assumed to be a few multiples of the bubble diameter then the proportion of the bed centre line enjoying wake enhancement can also be calculated.

The effect of halving the bubbling frequency to 2.5 bubbles/second is shown in Figure 3.11. We see the lower frequency results in weaker interactions between the bubble pairs. Also, a smaller proportion of the bed is occupied by bubbles. To get a fuller picture of the be-

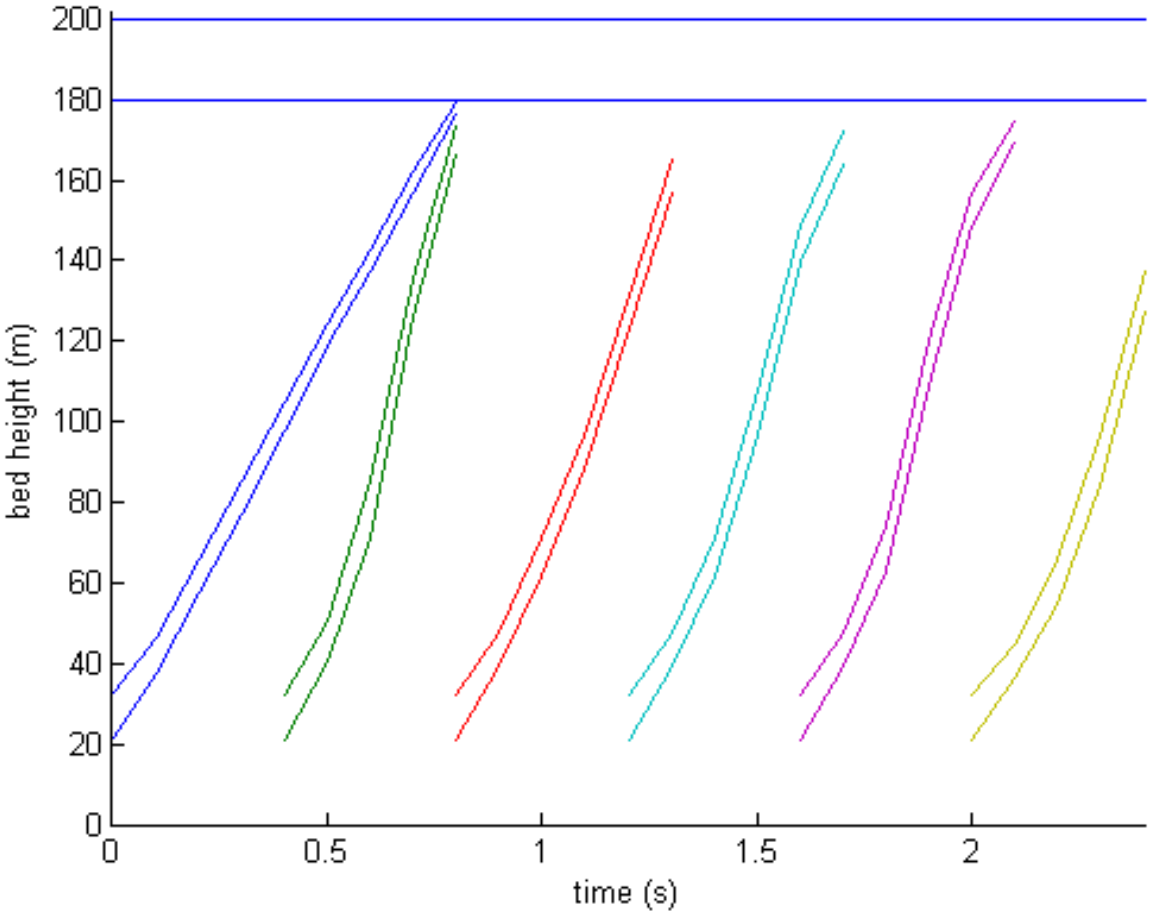

Figure 3.11: Bubble nose and tail positions with respect to time at a sparging frequency of 2.5 bubbles per second.

haviour with gas sparging, a bed of double the height is modelled, again at a frequency of 5 bubbles/second. The results are shown in Figure 3.12. The actual simulated bubbles are

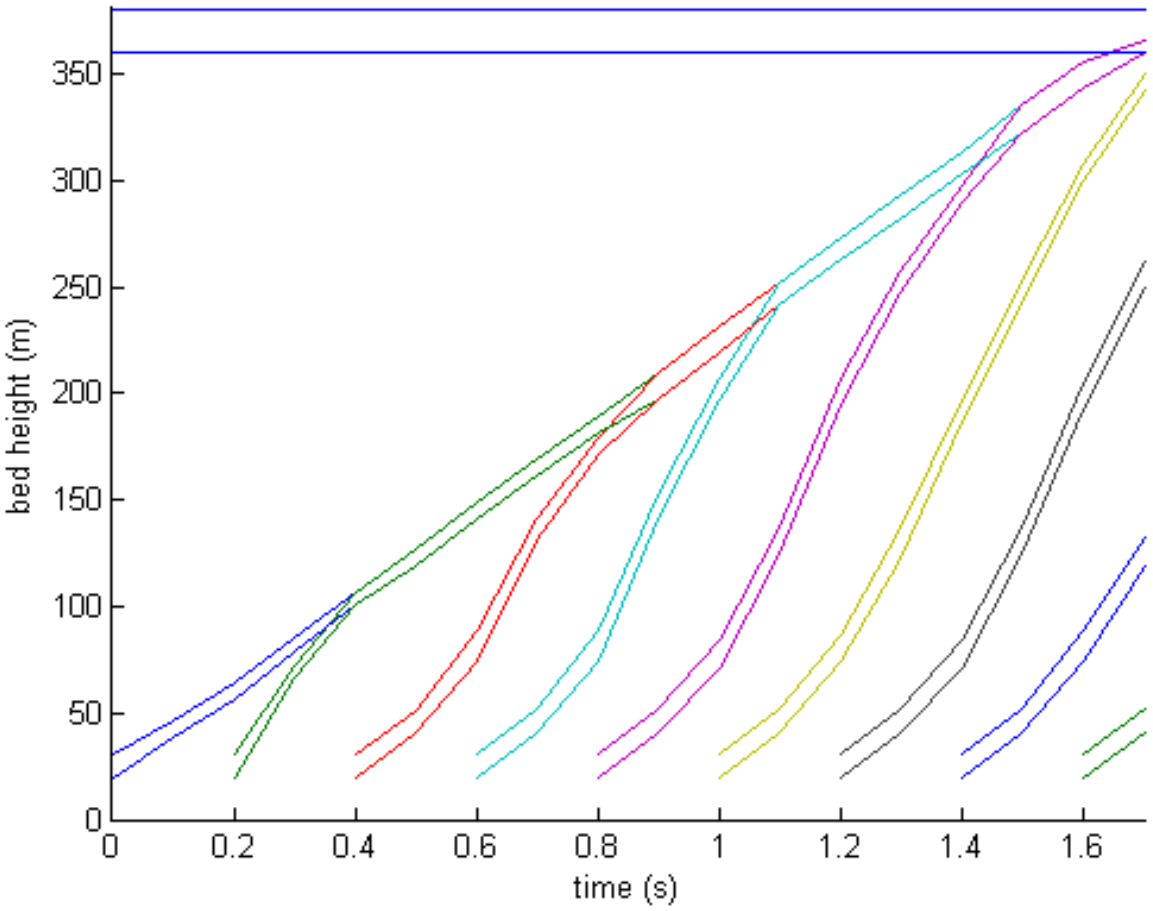

Figure 3.12: Bubble nose and tail positions with respect to time in a taller bed (400mm) at a sparging frequency of 5 bubbles per second.

shown in Figure 3.13. We see the increasing influence of the smaller shedded bubbles discussed above. As these coalesce and grow the bed behaviour becomes more unstable. This is likely to hamper the quality of control of the conditions in the bed. To remedy this, a period where no gas is added to the bed may be required. This will enable the bubbles to leave the bed allowing more stable conditions for the sparging of future bubbles, leading to better conditions for flux enhancement.

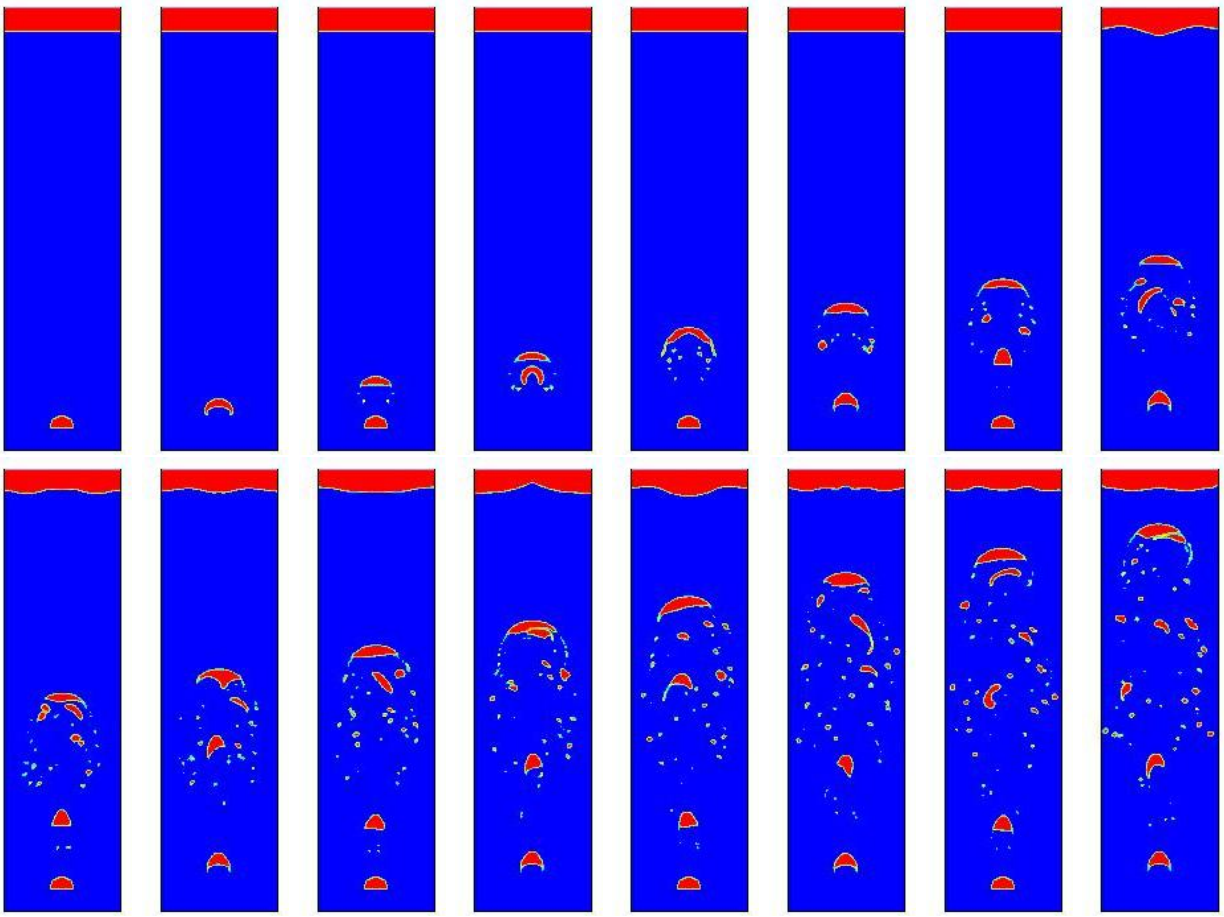

Figure 3.13: These images show the progress of bubbles at time steps of 0.1 seconds up a taller (400mm) bed at a sparging frequency of 5 bubbles per second. The shedding of smaller bubbles from the main bubbles leads to considerable instability in the phases. This is difficult to control and might require a period where no gas is introduced to return the bed to stable conditions.

Figure 3.14 shows the behaviour of two horizontally aligned bubbles moving up the bed. There is little interaction between the two as the low pressure wakes driving previous interactions are aligned, leading to small pressure gradients. This independent behaviour may

enhance the control of the bubbling if the bubble columns can be horizontally aligned in this way by perhaps having simultaneous pulse injection.

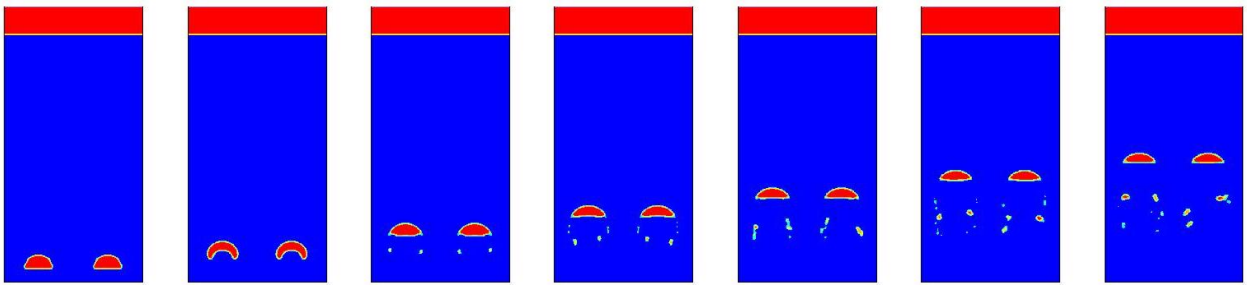

Figure 3.14: Weak interaction between horizontally aligned bubbles.

3.8 2D Results – Induced Flow Against Membrane

3.8.1 Bubble Shape

Figure 3.15 shows the bubble profile for increasing gas volumes. The bubble lengths, l_b, are 15, 25, 45 and 85 mm respectively. Relative to the channel thickness, Z the lengths are l_b/Z =1.25, 2.08, 3.75 and 7.08 respectively. Each bubble shows a smooth nose leading towards a film region. The film thickness reduces with bubble length until, for the longer bubbles, a minimum is reached. The larger bubbles have broadly flat tails and shed smaller bubbles in their wake. The smallest bubble has a slightly convex bubble tail due to the increased significance of surface tension forces compared to inertial forces. The bubble rise velocity was found to be 0.067 m/s for each gas volume. As in Taylor bubbles in tubes we can expect the rise velocity to be dependent on the gap width alone [96, 97]. Collins [98] gives $u_b = 0.23\sqrt{gZ}$ for a cylindrical cap bubble in a narrow channel. For the 12mm gap used this gives a rise velocity of 0.078 m/s.

3.8.2 Wall Shear

Figure 3.17 shows the shear profiles along the bubble length for the different bubble sizes. All bubbles share an increasing shear region in the liquid film. The restriction of flow due to the bubbles accelerates the liquid film downwards creating increasing shear due to the no-slip boundary condition at the wall. It is noticeable in particular for the larger bubbles that the shear flattens off towards the bubble tail. This suggests the liquid film approaches a terminal

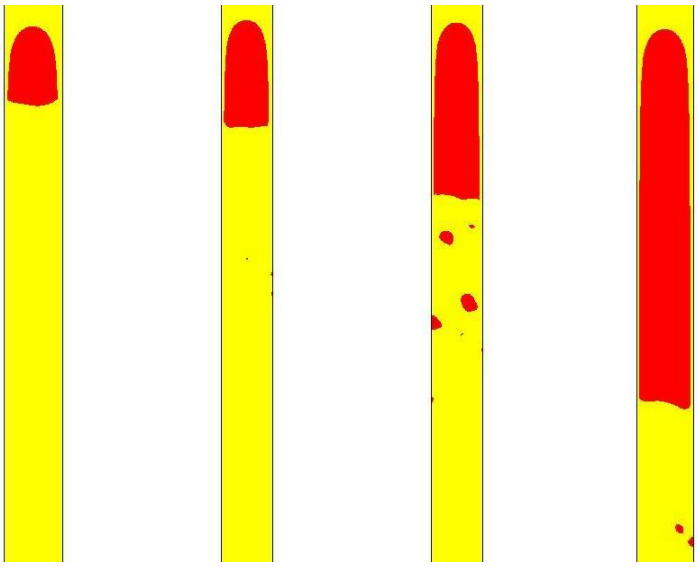

Figure 3.15: Bubble shape for increasing gas volumes. The length of the bubbles relative to the channel width (12mm) are 1.25, 2.08, 3.75 and 7.08 respectively.

velocity, where the shear at the wall balances the effects of the flow constriction due to the bubble. As the film cannot accelerate, conservation of mass will prevent any further thinning of the film. This also explains why the rise velocity of these bubbles, discussed above, is only dependent on the gap width and not gas volume.

At the tail and below the shear stress is highly variable. At the end of the bubble, the liquid film plunges into the wake region. The increased flow area will provide an average reduction in velocity resulting in reduced shear. However, considerable local velocity fluctuations exist providing oscillations in the shear profile. Figure 3.16 shows the pathlines the liquid follows when introduced at the top of the domain. We notice all the wake regions exhibit considerable asymmetry about the centreline of the domain. Small differences in the velocity, size and location of the film at the tail result in large deviations in flow below the tail. A perfectly symmetric flow below the tail may be regarded as a highly unstable equilibrium with respect to the flow conditions above. This also shows that modelling the flow using half the domain and a symmetry plane would be unsatisfactory.

The collapse of the liquid film into the wake and the subsequent oscillations in shear provide an excellent mixing region. Note also the size of the length of the wake region providing useful shear appears insensitive to the length of the bubble. The approach of terminal velocity in the film with respect to bubble length means the velocity of the film

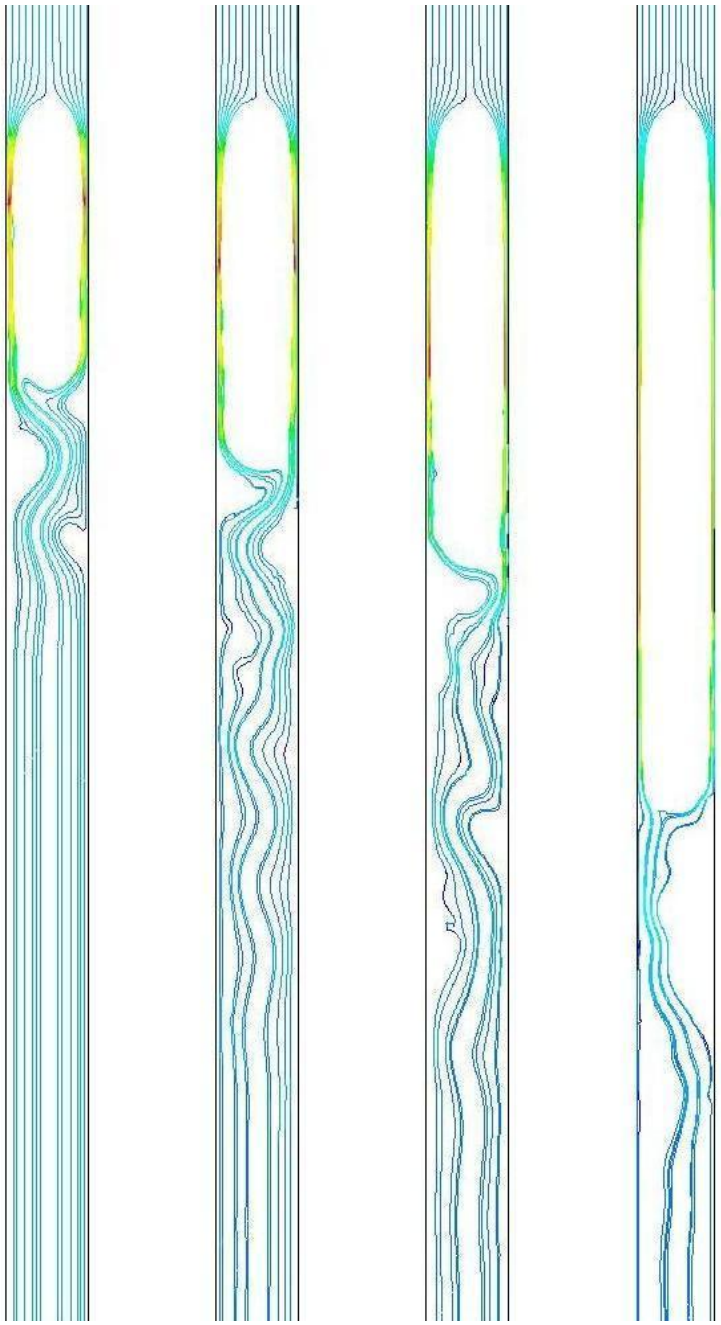

Figure 3.16: The pathlines of the liquid entering the top of the domain are shown for each bubble size at a given time.

entering the wake does not increase proportionately with bubble length.

Assuming the bubbles are sufficiently separate they may be treated individually. This provides the opportunity to build up an anticipated shear profile for bubble chains where the bubbles are of the same size and far enough apart to be analysed independently. We note the shear diminishes to zero away from the bubble tail. Clearly, in this region we may expect the flow to behave as it would without the preceding bubble. However, the non-zero shear wake region is significant with respect to bubble length and much of it is small compared to the shear at the bubble tail. To enhance the overall shear we could neglect the region where the shear has fallen to 10% of the maximum. The small shear region is replaced by the following bubble, as shown in Figure 3.19.

However, the control of the bubble distribution to build up the shear profiles in this way may pose considerable difficulties due to the strong interactions that occur. In particular, a trailing bubble is drawn into the low pressure wake region of the leading bubble. In this way slug bubbles tend to clump together and coalesce, which may provide less effective mixing properties.

Ducom et. al. [99] attempt to link the shear at the wall to the flux enhancement resulting from gas sparging. This employs the electrochemical method for determining shear indirectly, given by Reiss et. al. [100] and Cognet et. al. [101]. Zhang [10] uses the electrochemical method to determine the relative current enhancement, which can be correlated to shear stress, at a point from a passing bubble. The result is shown in Figure 3.20. The response shares the properties of the simulated shear results shown in Figure 3.17, with a steady increase in the film region followed by a diminishing but highly oscillatory behaviour in the wake region, providing good qualitative validation.

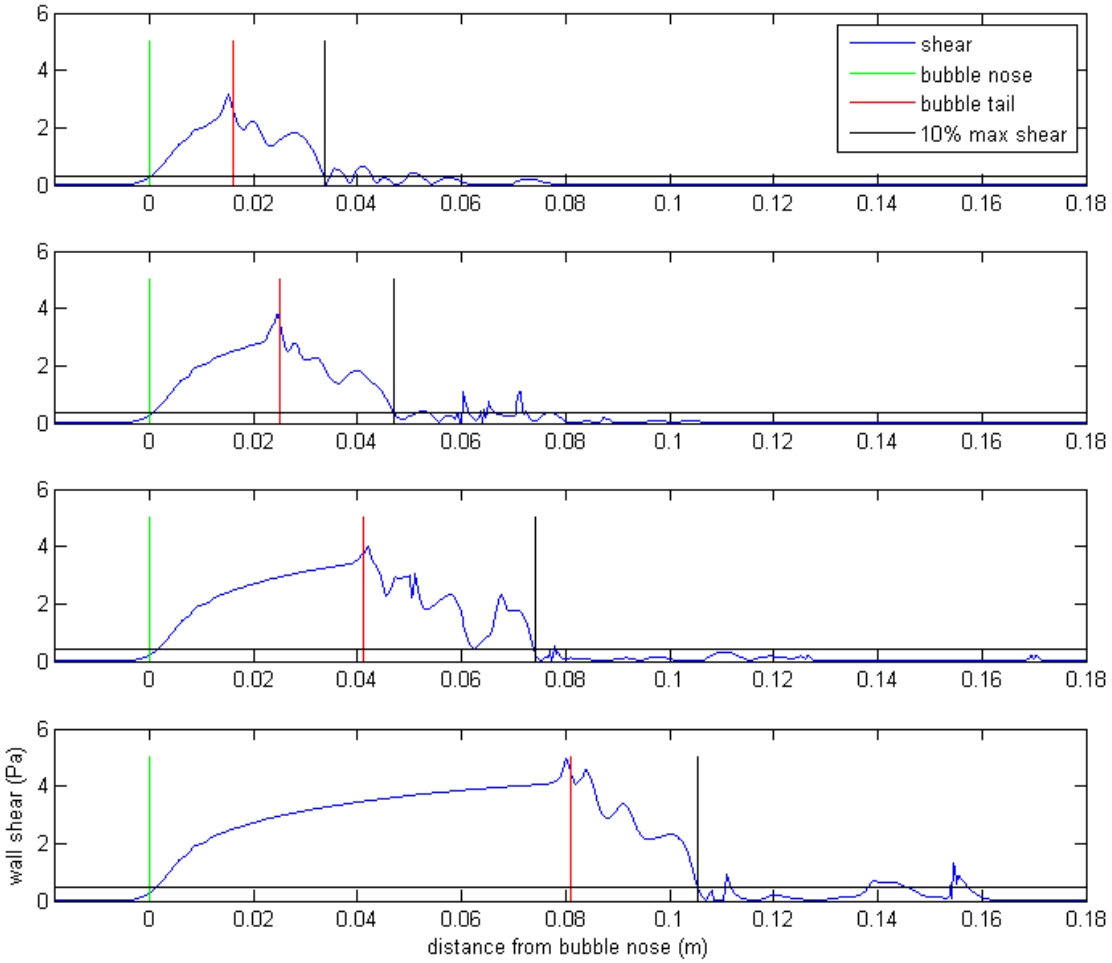

Figure 3.17: Shear profiles for the different bubble lengths of 15, 25, 45 and 85 mm respectively. In the main bubble region all profiles share a smooth increase in shear, directly corresponding to the thinning of the film. In the wake region, the mean shear decreases in the absence of the bubble. However, considerable local fluctuations in the flow yield oscillations in shear at much higher frequency.

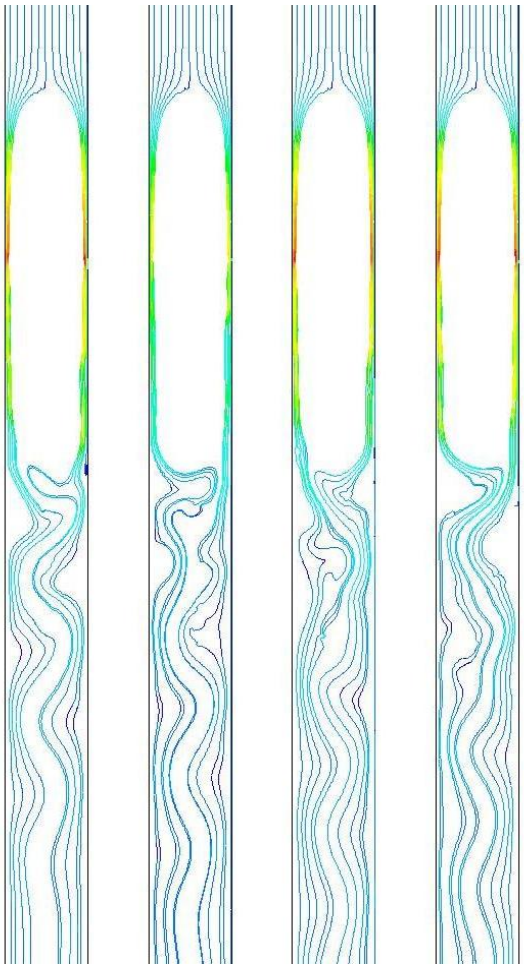

Figure 3.18: Oscillations in the bubble tail shown at a 0.12 second time increment. Note how the flow travels in a wave pattern down the domain. Also we see the alternation in which side of the film penetrates the central region most, this results in the downward motion of a given wake peak.

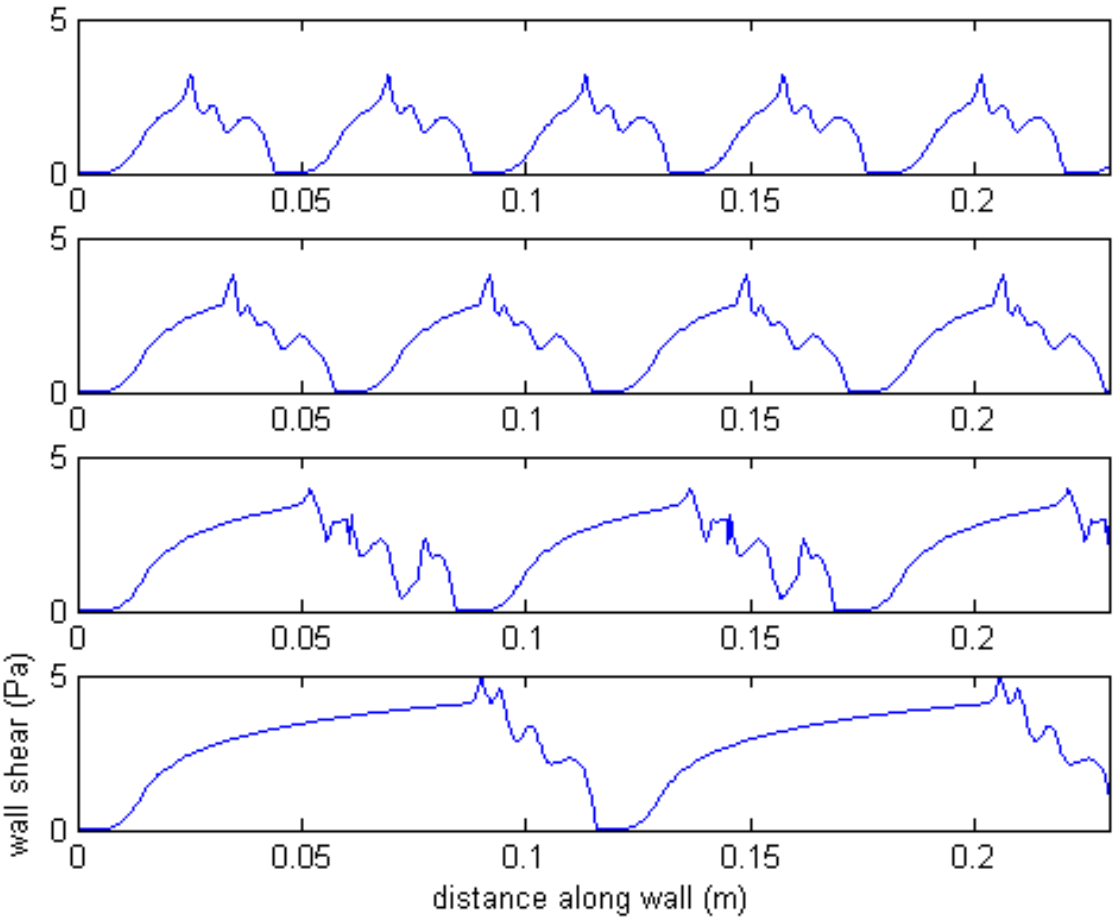

Figure 3.19: Shear profile as may been seen in a chain of bubbles with the same gas volume. If the bubbles are considered to be acting independently the shear profile from one bubble may be used to build up the complete picture.

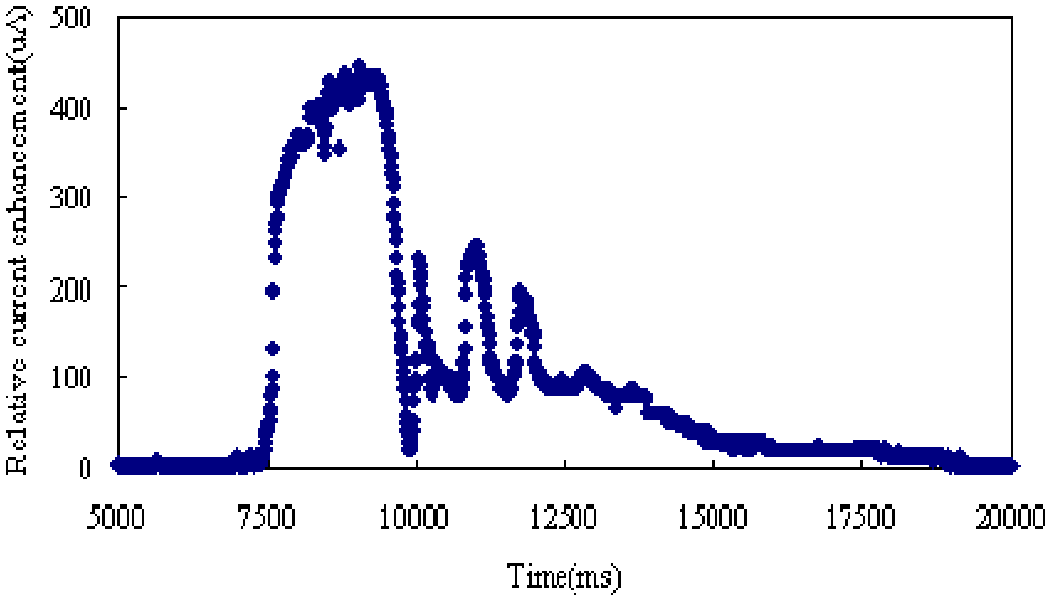

Figure 3.20: Measured response at a point to a passing bubble using the electrochemical method for shear measurement. Taken from Zhang [10, 11].

3.9 3D Results

In the 3 dimensional analysis, two principal factors are to be investigated the bubble volume, V, and the gap between the two flat plates, Z. The multiphase system will comprise air and water only, and the width and height of the flat plates will remain unchanged.

It is desired to analyse the effects of the gap width and bubble volume as these are key components in the design of flat sheet bubbling membrane filtration. An understanding of the hydrodynamics will later inform the flux under filtration.

Bubble volumes of, 3.075mL, 4.950mL, 7.032mL, 12.350mL, each in gaps, 6mm, 7mm, 8mm, 9mm, 10mm, 12mm, 16mm, 20mm, 28mm, 40mm, 80mm are calculated.

3.9.1 Convergence

It is necessary to ensure the results are mesh independent and that a sufficiently fine grid is used to ensure convergence. However, the cell size must not be so small as to render the computational time too great. To minimise computational time, the cell size used should be the largest that ensures convergence of the result. To determine this, the model is run for a 3.075 mL bubble with different cell sizes. For the 8mm gap width, the selected cell sizes for this work are $\Delta x = 0.001m$, $\Delta y = 0.0016m$, $\Delta z = 0.0001m$ in the x,y and z directions respectively. The different lengths of cell size reflect the size of the domain. There are 80 cells in the x direction, 75 in the y-direction and 80 in the z-direction. This cell density was retained for the subsequent simulations at larger gap widths. Note a simple Cartesian system of equal cell sizes in a given direction is employed, as this allows for subsequent incorporation into the particle flux model. The bubble rise velocity is used as the metric for testing the grid convergence. This is shown in Figure 3.21. The bubble rise velocity is plotted with respect to the number of cells in the z direction, (10 20 40 80 160). After 80 cells, the change in bubble rise velocity becomes small indicating satisfactory convergence.

3.9.2 Bubble Shape

Figure 3.22 shows the calculated shape both in the plane half way between the membranes and the central vertical plane perpendicular to the membranes, for a volume of 3.075 mL and gap of 8mm. The bubble nose was found to be held steady (at a height of $y_b = 94.5$mm) with an inlet downflow at the top of 0.264m/s, which is taken to be the bubble rise velocity.

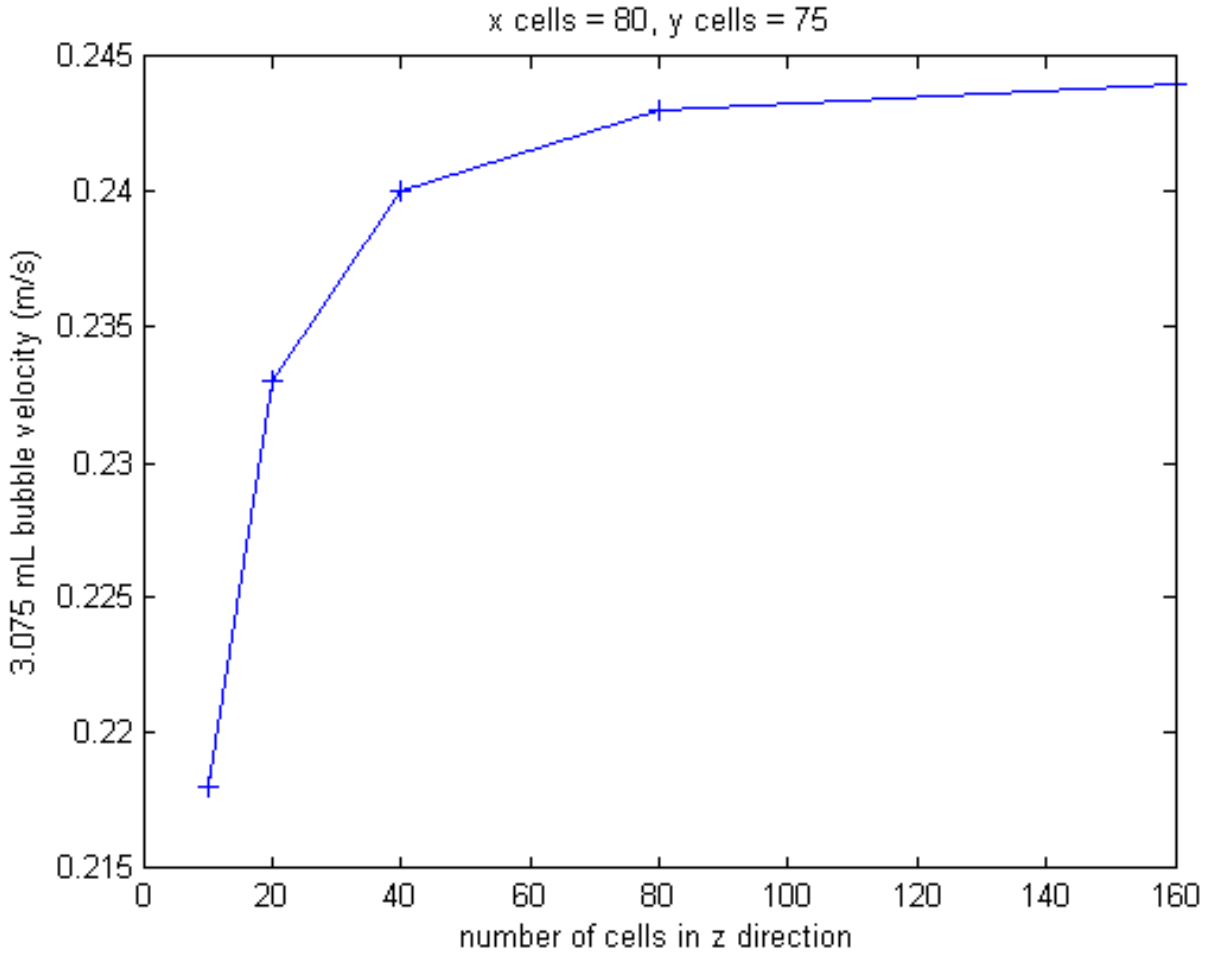

Figure 3.21: Grid convergence for the rise velocity of a 3.075 mL bubble. Domain width $X = 80$mm, height $Y = 120$mm and gap $Z = 8$mm.

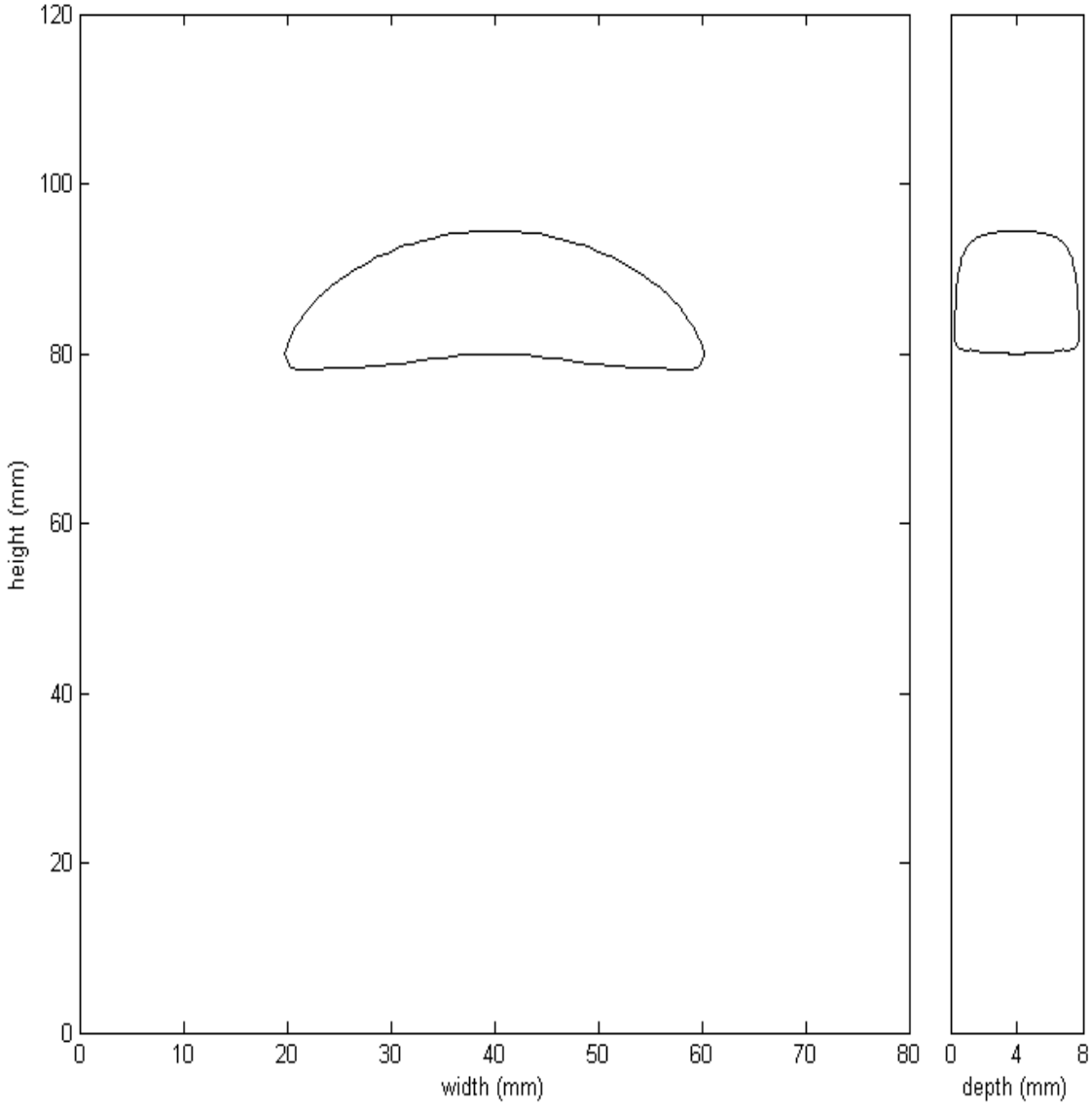

Figure 3.22: Bubble volume, $V = 3.075$mL. Membrane width $X = 80$mm, height $Y = 120$mm and gap $Z = 8$mm.

The bubble shows the typical spherical cap shape found in larger bubbles, note the membrane is assumed to be hydrophilic, which ensures the membrane is always wetted and there is always a liquid film between bubble and membrane.

The bubble shape can be described as spherical cap for larger Eotvos numbers greater than 10 in an unconstrained flow area. As the bubble gap is reduced, the shape is better described as a circular cap. To analyse the bubble shape for the results, a shape factor is introduced. The simplest shapes with well defined geometry similar to the spherical and circular caps are a hemisphere and hemicylinder respectively. The bubbles investigated are defined by their volume, the volume of a hemisphere with respect to its diameter is $V = \frac{\pi}{12}d^3$ and for a hemicylinder $V = \frac{\pi}{8}d^2Z$, where the length of the hemicylinder is taken as the gap width. Hence, for a given bubble volume and gap width, we can find the equivalent diameter for each shape.

The actual calculated diameter is found from measuring the maximum width of the 50% gas volume fraction contour of the bubble from the results. For each bubble and gap this diameter is recorded and compared to the equivalent diameter. Figure 3.23 plots the ratio of the equivalent diameter to the actual calculated diameter (shape factor) for each shape against the ratio of the bubble depth to the gap depth ($\frac{b_z}{Z}$). For larger gap widths where the bubble depth is small compared to the gap depth, the hemisphere provides a better approximation of the bubble shape, as it has a closer shape factor to one (0.9), whilst the hemicylinder approximation is much poorer with a shape factor of less than 0.5, indicating a spherical cap shape. The shape factor is less than one, as the spherical cap is concave in shape with less thickness than the hemisphere. The concave shape results in a wider span of the bubble.

As the gap width is reduced, the depth of the bubble becomes more significant with respect to the gap depth. This results in the hemisphere becoming a poorer shape approximation and the hemicylinder becoming the more representative shape. This transition occurs once the bubble depth exceeds 89 percent of the gap depth. Again, the bubble shape remains concave in nature with a shape factor less than one until the gap depth is smaller than 8mm. For the smallest gap depths, the shape factor actually exceeds one. This indicates a transition to a convex shape. This is likely the result of surface tension effects which are more significant for smaller gaps. Surface tension effects will promote a rounder bubble tail region, as is seen in very small flow areas such as capillaries, hence the more convex shape.

There is strong correlation between the ratio of the bubble depth to gap depth and the two shape factors, irrespective of bubble volume. Clearly, for the range of volumes investigated, the depth ratio is the governing influence on bubble shape.

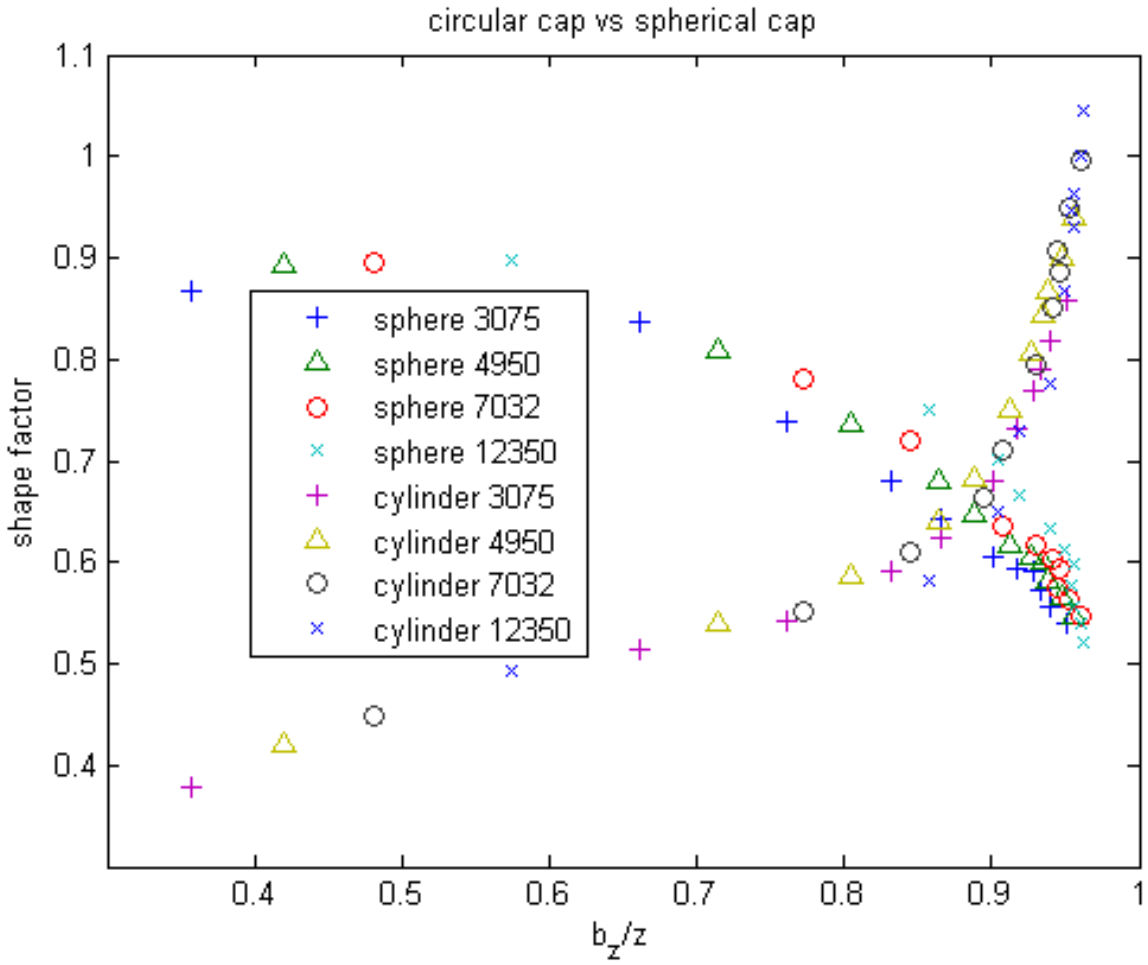

Figure 3.23: The shape factor indicates how similar the bubble shape is to a hemisphere or hemicylcinder. It is the ratio of the diameter of a perfect hemisphere or hemicylinder to the calculated bubble diameter. Where the ratio of bubble depth to gap depth is small, the shape is similar to a hemisphere. When the bubble depth is greater than 0.9 of the gap depth, a hemicylinder is a much better approximation of the shape.

Figure 3.24 shows the aspect ratio of the calculated bubble width, b_x, with respect to the bubble depth, b_z. As the gap depth reduces, the bubble width increases, as is expected. The results are characterised by the asymptotic nature of the film thickness between the bubble and membrane for smaller gap widths. As the membrane is assumed to be hydrophilic, the

ratio of the bubble depth to gap depth is always less than one. For the results plotted, the largest gas fraction in the gap width (z) direction is 96.2 percent. Large increases in gas volume or reductions on gap width appear to have little impact on this maximum.

Note again the strong correlation between the aspect ratio and the bubble depth to gap depth ratio. Given this correlation, we can deduce that a bubble of higher volume in a larger gap width is geometrically similar to a smaller bubble in a smaller gap, where the ratio of the bubble depth to the gap depth is the same. This is to be expected, as the bubbles for the range of volumes and gap depths analysed will have similar Eotvos and Reynolds numbers on a log10 scale. Namely, $1.64 < log_{10}Eo < 2.05$ and $3.6 < log_{10}Re < 3.9$.

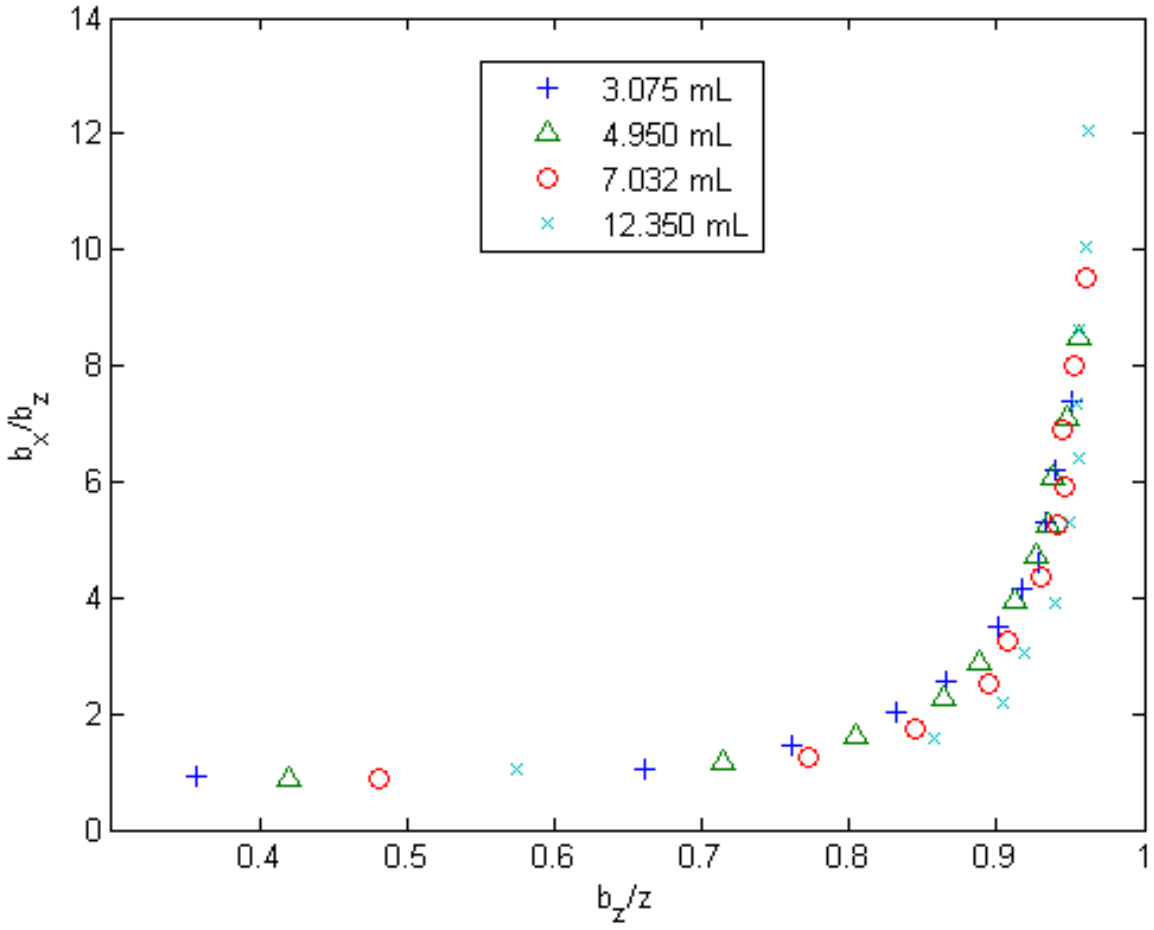

Figure 3.24: This figure indicates the strong correlation between the width and depth of the bubble (the aspect ratio) against the bubble depth to gap depth ratio.

Figures 3.25, 3.26, 3.27 shows the bubble shape in the plane of the flat sheets for the

3.075mL and 7.032mL bubbles in each plane.

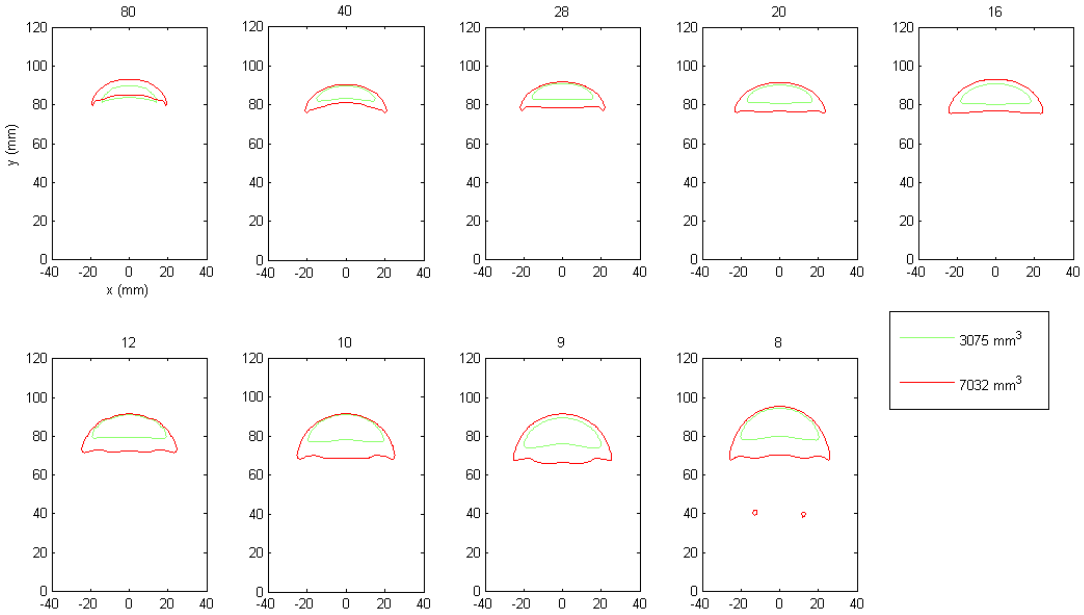

Figure 3.25: Bubble shape in x-y plane by gap depth for gas volumes of 3.075mL and 7.032 mL.

Figure 3.27 shows the top view (x-z plane) of a 3.075mL and 7.032 mL bubble for gap widths, 8mm, 9mm, 10mm, 12mm, 16mm, 20mm, 28mm, 40mm, 80mm. The transition between a spherical cap shape for the larger gap widths to a cylindrical cap shape is shown.

3.9.3 Wall Shear

Figure 3.28 shows the mean shear magnitude generated against the membrane wall by the bubble. Clearly, for very large gap widths, the shear is small as the effect on the liquid flow by the bubble is restricted to the center. As the gap is reduced, clearly the flow at the membrane surface starts to be more influenced by the bubble, resulting in higher mean shear values.

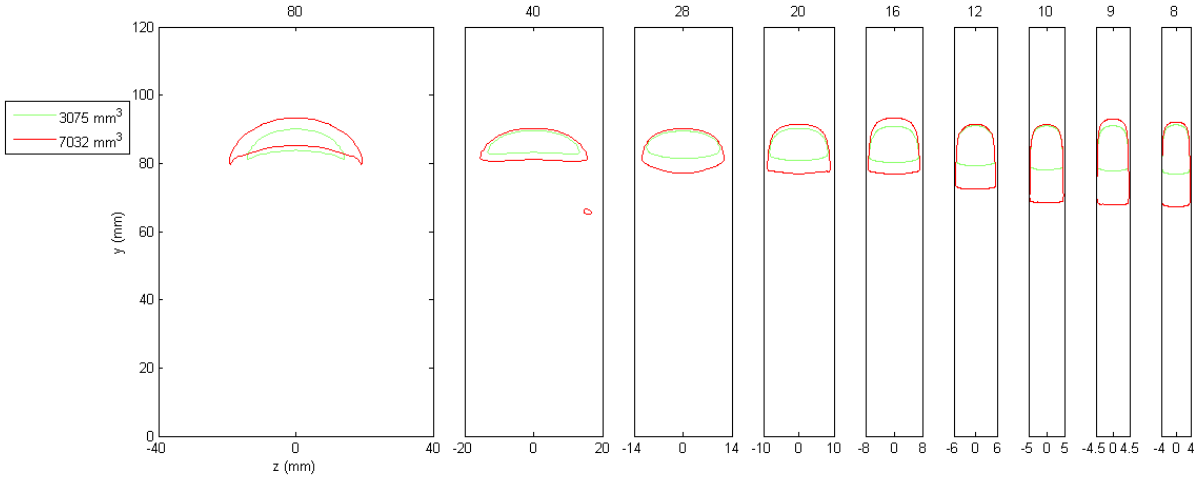

Figure 3.26: Bubble shape in y-z plane by gap depth for gas volumes of 3.075mL and 7.032 mL. The influence of gap width on bubble shape for a given gas volume. From left to right the gap widths are, 80mm, 40mm, 28mm, 20mm, 16mm, 12mm, 10mm, 9mm, 8mm respectively. Note the limiting minimum of the liquid film between the membrane and the bubble.

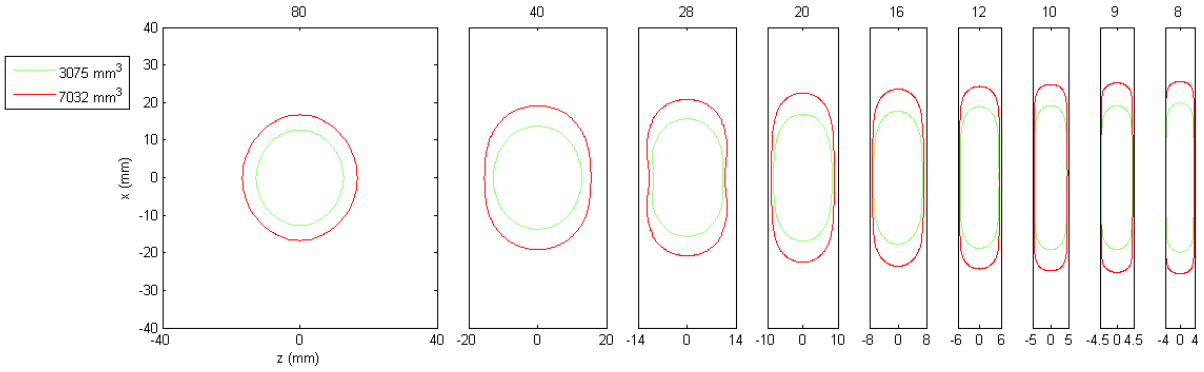

Figure 3.27: Bubble shape in x-z plane by gap width for gas volumes of 3.075mL and 7.032 mL.

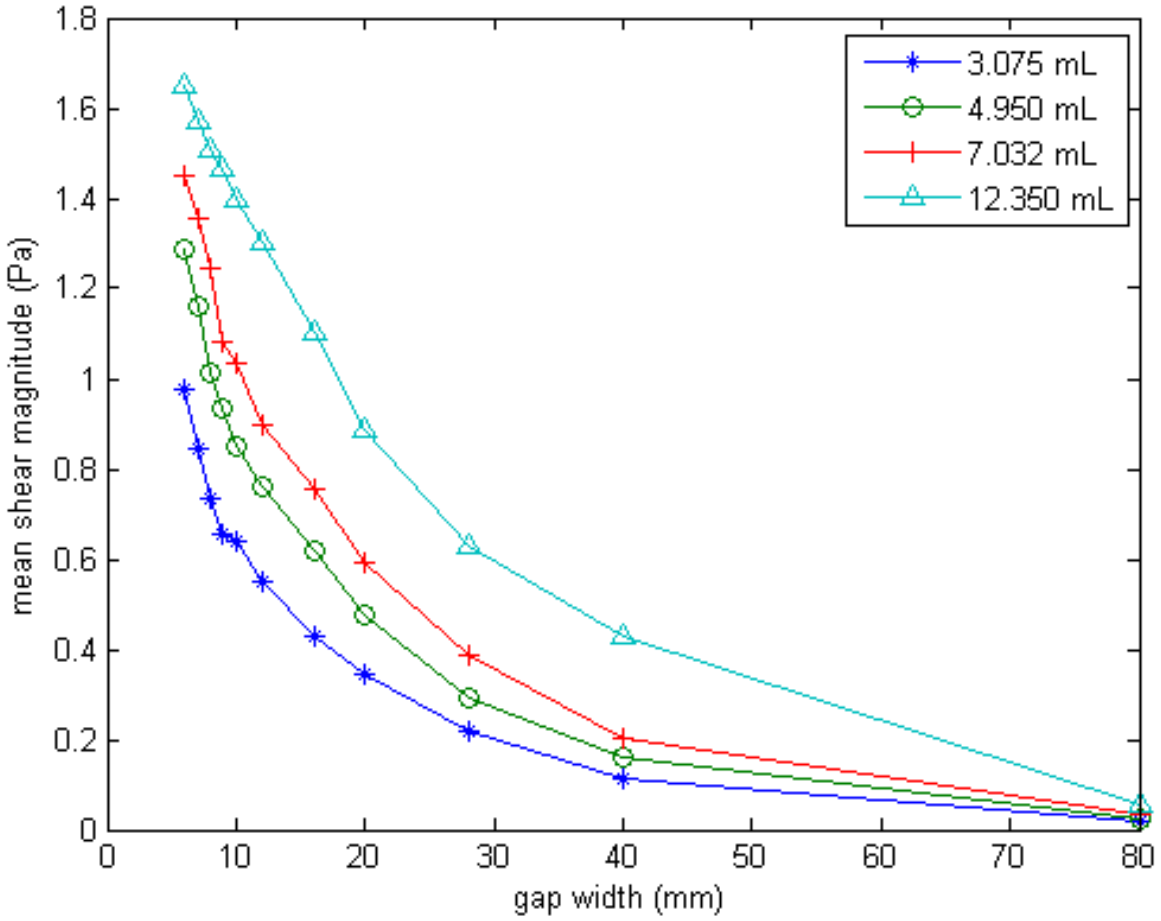

Figure 3.28: The mean shear magnitude increasing with the reduction of the gap. The mean shear magnitude is plotted, instead of maximum shear, as this is more representative of the predicted flux enhancement using shear based methods.

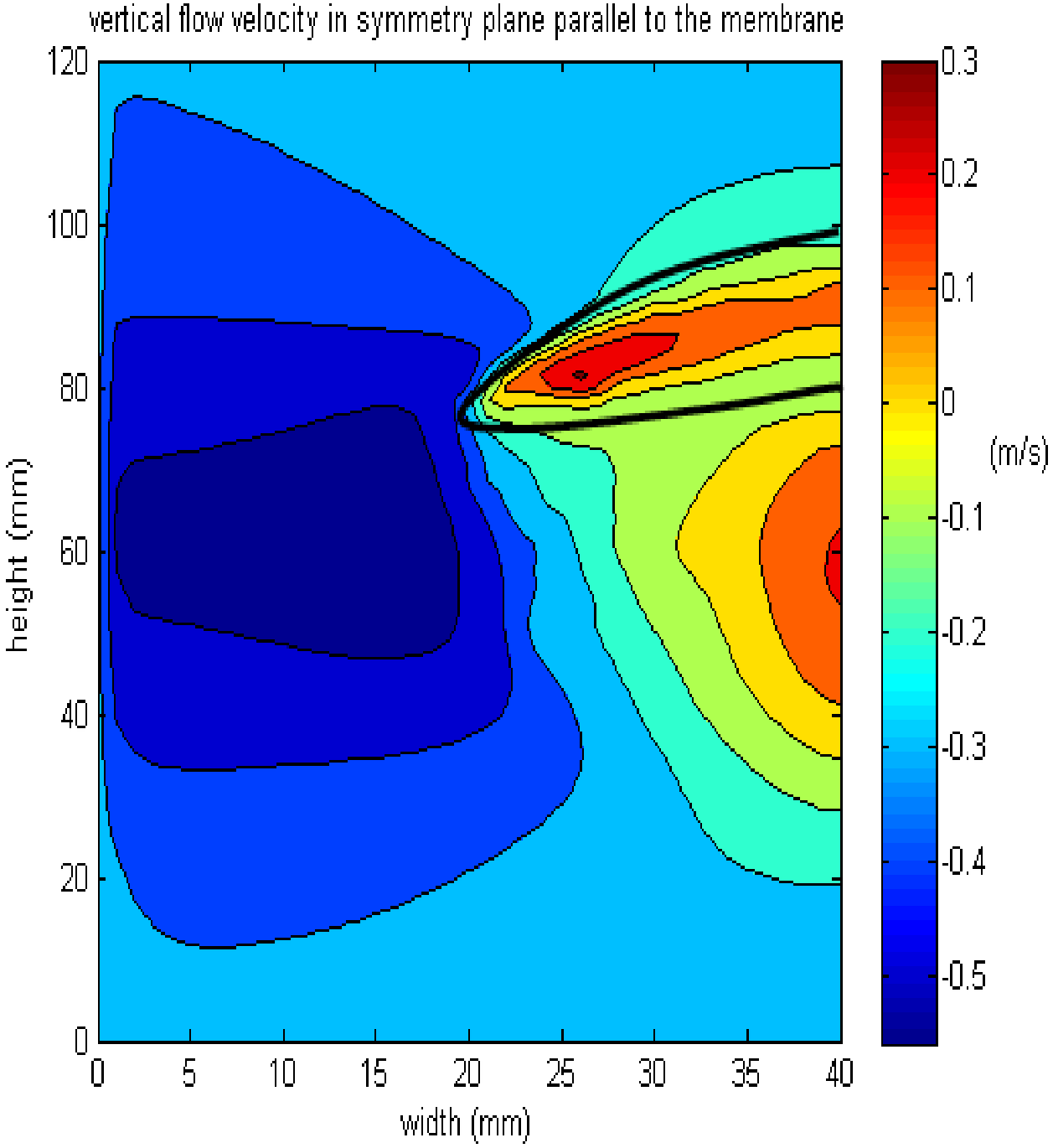

Figure 3.29: The flow of the liquid phase around the 3.075 mL bubble in a 8mm gap, the black line shows the position of the bubble. The boundary condition at the top is an inlet defined at the velocity found to hold the bubble stationary (the bubble rise velocity). This is in the central plane parallel to the membrane. There are regions of upward flow in the recirculatory regions of the bubble and the wake. However, the main feature is the acceleration of the flow to the side of the bubble caused by the constriction of flow area by the bubble.

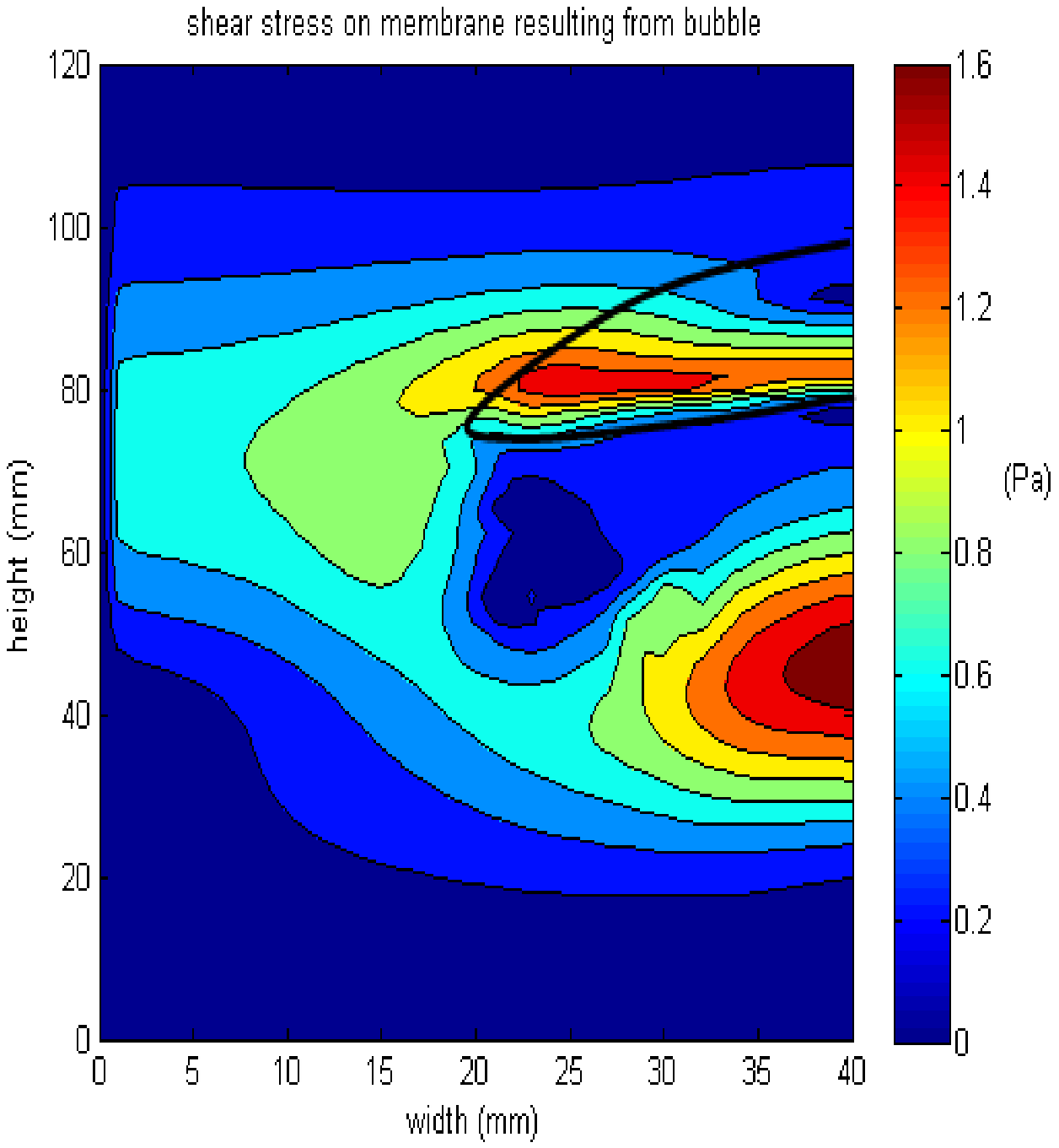

Figure 3.30: The shear on the membrane due to the 3.075 mL bubble in a 8mm gap, the black line shows the position of the bubble. There are high shear regions adjacent to the bubble caused by the small film between bubble and wall. There is also increased shear in the wake region below the bubble.

3.9.4 Bubble Rise Velocity

The rise velocity of bubbles in extended liquids and in two dimensional planar set ups is well researched. However, the response of the bubble velocity as its flow geometry transitions from one extreme to the other is not. Figure 3.31 shows the bubble rise velocity with respect to gap. At the larger (80mm) gap the bubble is unconstrained by the walls. This allows the liquid phase to pass more easily around the bubble, permitting a higher bubble rise velocity. As the gap is reduced towards the free width of the bubble, the liquid around the bubble is subject to greater shear by the walls, reducing the ease with which it can flow past the bubble, resulting in a lower rise velocity. This will be termed the z dominant region, the ratio of bubble width in z to gap being the key factor. However as the gap is reduced further the shape of the bubble is significantly affected by the walls. The constriction results in the bubble assuming a more streamline shape. In particular the frontal area past which the liquid must flow is reduced, resulting in less drag on the bubble. This allows a higher bubble rise velocity. This will be termed the transitional region. As the gap is further reduced, however, the width of the bubble in the x-direction becomes significant and velocity starts to be reduced due to drag in that direction. This will be termed the x dominant region.

Figure 3.32 compares the rise velocity in dimensionless form with respect to z, $\frac{u_b}{\sqrt{gZ}}$, and the aspect ratio of the flow geometry. It shows good correlation for each bubble volume. Where aspect ratio is greater than 0.2 this would provide a reliable method of determining the bubble rise velocity. However, as the ratio is more skewed with smaller gaps Z the data is more spread giving a less reliable indicator of bubble rise velocity. This is a result of the increased influence of the bubble width in the x direction.

Unlike the usual analysis which varies the gas volume for a given flow geometry, this analysis is based on the effect of changes in the gap depth for a given volume of gas. The method to obtain a meaningful dimensionless velocity in the x direction is developed here.

The rise velocity of bubbles in extended liquid where the boundaries are sufficiently large to not be a factor in the rise velocity is given by equation 3.12 [6], where $d_e = \left(\frac{6V}{\pi}\right)^{\frac{1}{3}}$ is the equivalent diameter, assuming a spherical volume, V.

$$u_b = 0.71\sqrt{gd_e} \tag{3.12}$$

The equivalent diameter defined above is independent of gap depth, so will be constant

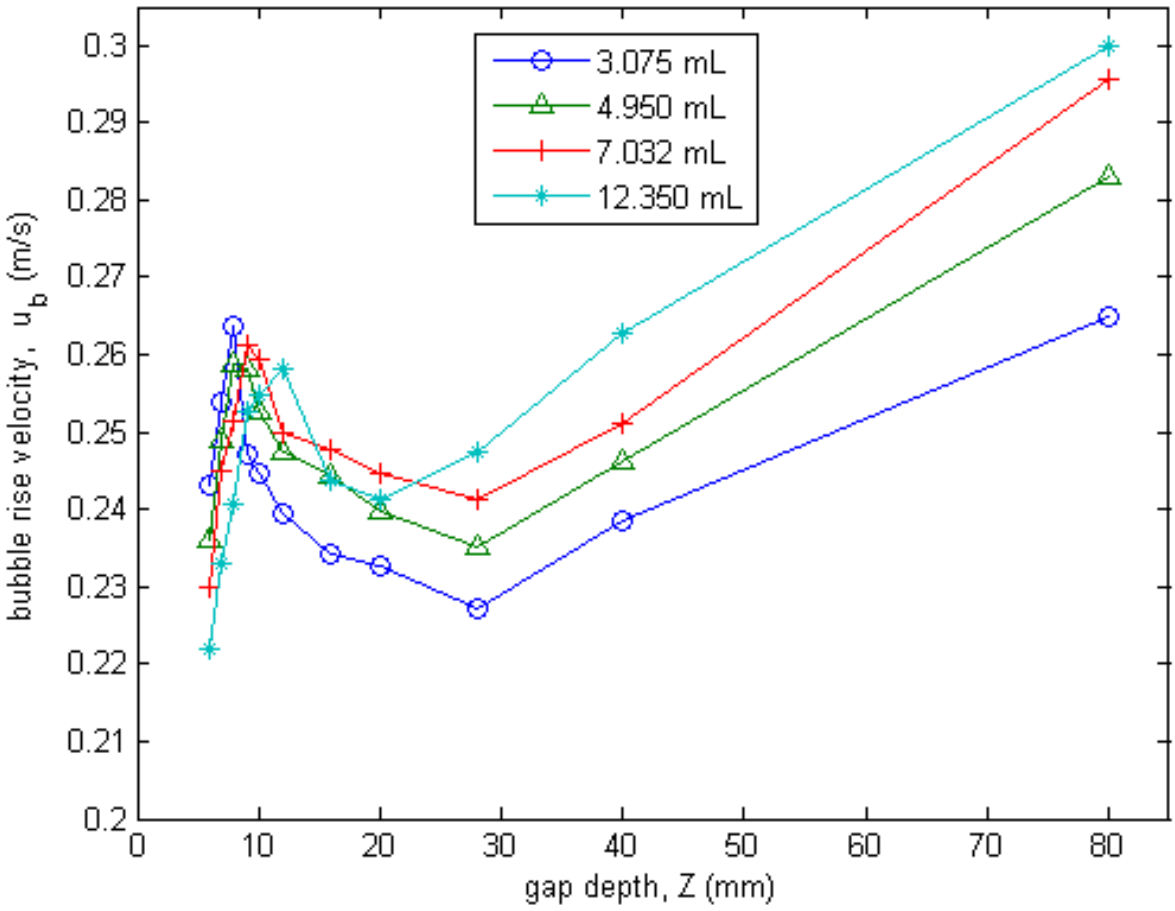

Figure 3.31: The bubble rise velocity for each bubble volume for a given gap depth. Each bubble shares three flow types. For larger gaps the bubble is largely unconstrained by the walls so has a higher velocity. As the gap is reduced the drag on the walls creates a reduction in the rise velocity. However, as the film region is formed and is largely constant there appears an increase in bubble velocity. The shape of the bubble is streamlined by the constriction. Further gap reduction brings a decrease in velocity as the width of the bubble becomes significant to the side walls resulting in additional drag as the flow is no longer free in that direction.

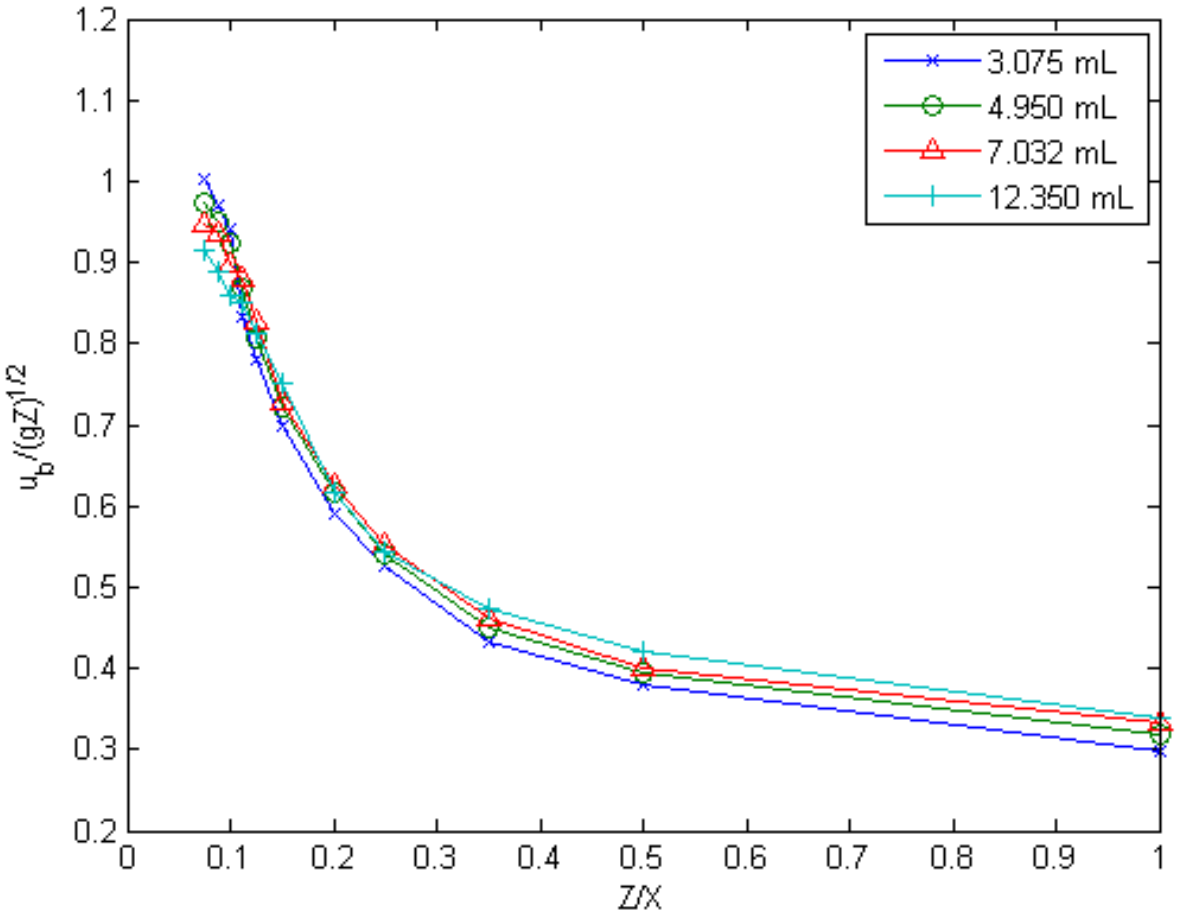

Figure 3.32: The bubble rise velocity is given dimensionless form for the gap depth Z. There is good correlation between this and the aspect ratio of the flow area. The value $Z/X = 1$ represents a square flow region. For the flow regions with small depth, Z, the correlation is less clear as in this region the size of the bubble in the x direction becomes more significant.

for each bubble. This neglects the changes in conditions that will inevitably occur as the gap is varied. To account for this, a new equivalent diameter for the width of the bubble in the x-direction, d_x, is introduced. This assumes the gas volume is in the form of a cylinder whose axis is perpendicular to the membrane and whose length is equal to the gap depth, z.

$$d_x = \left(\frac{4V}{z\pi}\right)^{\frac{1}{2}} \tag{3.13}$$

Equation 3.12 is now rewritten in terms of d_x, giving, $u_b = 0.71\sqrt{\frac{d_e}{d_x}}\sqrt{gd_x}$. Hence the equivalent dimensionless rise velocity is given by equation 3.14 whoch accounts for both gap and bubble volume.

$$\frac{u_b}{\sqrt{gd_x}} = 0.71\sqrt{\frac{d_e}{d_x}} = 0.68\left(\frac{\pi}{V}\right)^{\frac{1}{6}} Z^{\frac{1}{4}} \tag{3.14}$$

Figure 3.33 compares the dimensionless rise velocity with theories for both the case of bubbles rising in extended liquid and bubbles rising in a plane. The curves above the data points are the dimensionless rise velocity for a bubble in an extended fluid, $0.71\sqrt{\frac{d_e}{d_x}}$. The curve below the data points is the correlation established experimentally for flow in a narrow gap between two flat sheets and numerically for 2d CFD calculation, $0.2\sqrt{\frac{X}{d_x}}$, by Krishna et al [12].

For the larger gaps the bubble rise velocity is closer to the extended flow theory case, as the walls have less influence. As the gap is reduced and the influence of drag on the walls increases, the bubble rise velocity decreases and approaches the 2d theory case. An exception to this general rule occurs after the bubble undergoes significant size reduction in the z direction as the gap becomes smaller. In this region the bubble rise velocity increases. It has been argued that the bubble shape becomes more streamlined as the projected area decreases [102]. This is only valid while the bubble width in the x direction permits free flow in that direction. The small flow in the film between the bubble and the wall is less significant than the flow between the bubble and side walls in the X-direction.

Figure 3.34 compares the dimensionless rise velocity in x, $\frac{u_b}{\sqrt{gb_x}}$, with the sphericity of the bubble shape. It shows how the respective velocity regions share bubble shape, Z dominant for sphericity ratios less than 1.6, transitional between 1.6 and 1.75 and X dominant for ratios greater than 1.75.

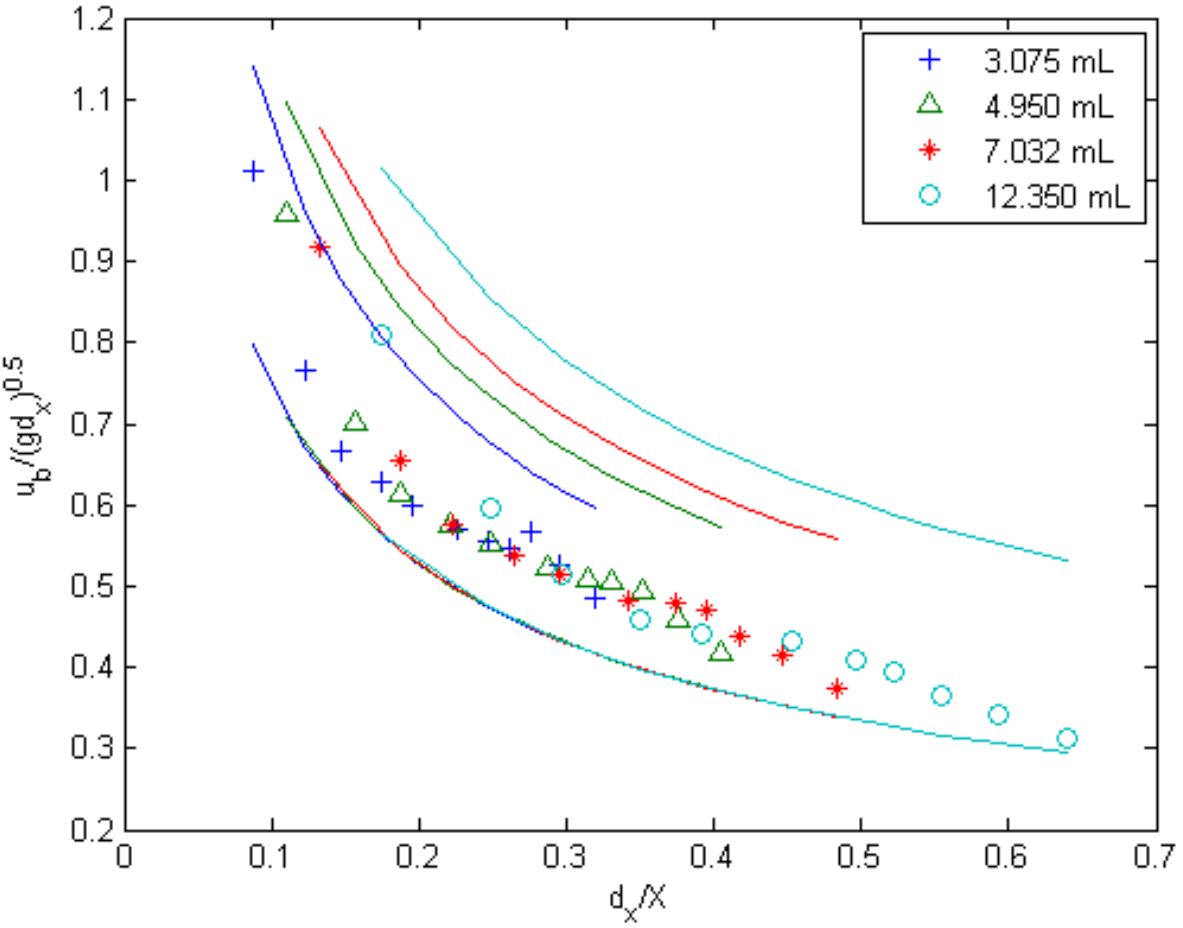

Figure 3.33: The top lines are the unconstrained dimensionless rise velocities for each bubble volume. The bottom line is the dimensionless rise velocity for a 2-dimensional simulation [12]. The data shows the transition between the two flow regimes and which is more significant. When the width of the bubble is small compared to the domain width, the velocity is similar to the inconstrained case. However, as the relative bubble width increases the 2 dimensional approximation is more representative.

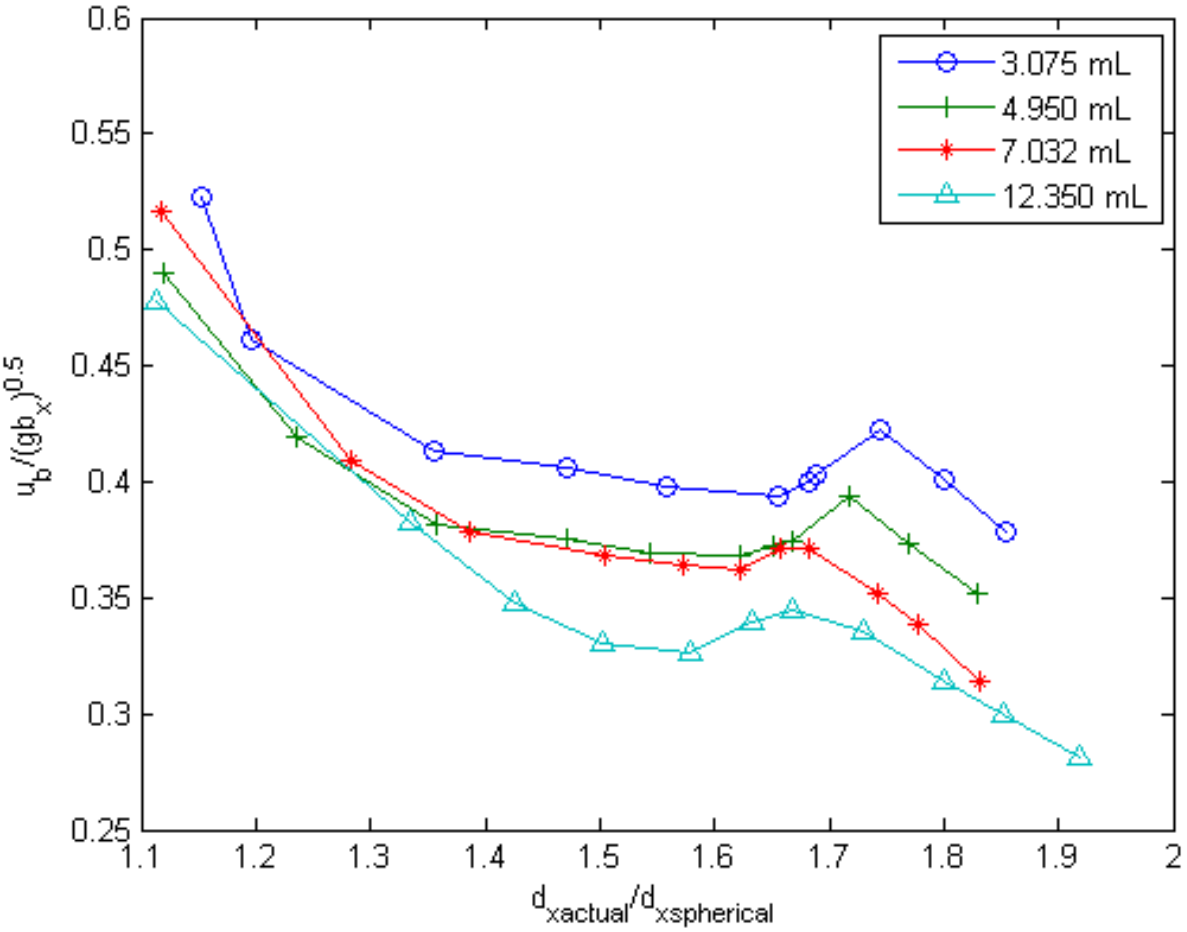

Figure 3.34: The dimensionless velocity compared to the sphericity of the bubble shape. This indicates the correlation between bubble shape and the region where the bubble has a peak in velocity, in the region where the ratio is around 1.7.

3.10 Summary

The CFD method provides a simulation of single gas bubbles between two flat parallel plates. The gap between the plates was smaller than the free width of the bubble, generating a constriction of the bubble and a film region between bubble and membrane. This generates additional shear on the surface beneficial to membrane filtration.

The 2 dimensional models provided insight into the bubble motion behaviour in one plane and the secondary flow generated near the membrane surface in the other plane. In the 2 dimensional simulation in the plane of the plates, the bubble shape and rise velocity compared well with the literature. Multiple bubble situations were also investigated showing the interaction between them. As expected, vertically aligned bubbles show strong interaction due to the low pressure wake region behind them which attracts the following bubble, whilst horizontally aligned bubbles show weaker interaction. In the plane perpendicular to the membrane, we saw the effect of the constriction due to the membranes. In a bubble steady frame of reference, the liquid film is accelerated down past the bubble. This causes a steady increase in shear until the base of the bubble is reached, whereupon the behaviour of the wake leads to a more turbulence influenced shear profile with higher frequency fluctuations.

The 3 dimensional model was able to simulate the bubble shape, motion and the secondary flow near the wall. The factors affecting the bubble rise velocity where shown to vary depending on the gaps. As the gaps start to decrease and the size of the bubble in this direction becomes significant, it is this length which is significant however, as further reductions in gap occur the width of the bubble in the x direction compared to the domain becomes the significant factor. In between these regions, there is a transitional region where the bubble rise velocity increases due to streamlining in z and the width in x is still not significant.

The model can also be applied to different membrane geometries. For example where hollow fibre membranes are used. In this case the governing equations for the concentration (convection-diffusion) and hydrodynamics (Navier-Stokes) would have to be restated in cylindrical form. The Matlab code would then have to be rewritten to solve the cylindrical form of the convection-diffusion equation and cyclindrical grids would have to be formed for the CFD solution of the Navier-Stokes equation. The physical principles of the model would remain unchanged.

4 Flux Enhancement for Bubbling Membrane Filtration

4.1 Introduction

In the previous sections, a method has been developed to calculate the flux performance of membrane filtration systems in the presence of a gas phase. This is now used to determine the most efficient MBR design. The filtration system is influenced by numerous design considerations. In this section, the effect of changes in the design is considered. It is desired to determine the optimal conditions for the enhancement of filtration flux by the bubble.

When considering the set up of two parallel flat plates, one of the principal design factors is the gap between the two flat sheet membranes. One can expect variations in the rise velocity, and induced shear on the membrane as the gap is varied. Another significant consideration will be the size of the bubble or the gas volume fraction (voidage). Again, for a given gap, changes in gas volume will result in changes in the bubble rise velocity and induced shear. The effect these changes have on the resultant flux will govern the efficiency of the design.

One should bear in mind the energy costs of introducing the gas phase. For example, one may obtain good flux enhancement by the introduction of a vigorous sparging of gas. However, the associated cost of this would undermine the overall benefit of the gain in flux. By knowledge of the effect of bubble size and gap, one can gain the greatest benefit when the flux enhancement is compared to the energy cost (amount of gas).

The multiphase particle flux behaviour will be calculated for each of the bubble hydrodynamical conditions investigated in the CFD analysis. This is done by taking the velocity matrices from the CFD calculation as the convection terms in the convection-diffusion equation. Investigating the large number of variables discussed in the 2 dimensional single phase section is not carried out, as the computational burden is too great to allow for useful results in a reasonable time. Control variables are defined and are present in each calculation, unless otherwise stated. These are, $TMP = 100kPa$, particle diameter $d_p = 0.2\mu m$, particle density $\rho_p = 2000kg/m^3$. Clean water resistance $R_m = 2.5\text{x}10^{12}m^{-1}$. Bulk concentration $c_b = 15g/L$. Permeate viscosity, $\mu = 0.001Pa.s$.

Although the CFD model was appled to the whole domain with no symmetry boundary conditions, the particle flux model is calculated for one half of the domain on the width X.

This is done to save computing time and reduce redundancy. Symmetry is assumed about $x = X/2$, hence only the width in x from 0 to 40mm is shown.

4.2 Particle Concentration

Figure 4.1 shows the particle concentration on the membrane wall. The influence of the bubble can be seen. At the bubble itself the concentration is lower. This is due to the increased shear region against the membrane resulting from the thin film of liquid accelerated downwards by the contraction in flow area. Directly below the bubble, the wake area also enjoys a region of lower concentration polarisation. We can see a region of increase particle build up below the left edge of the bubble. Particles are pushed away from the centre to the edge by the flow around the bubble. This leaves the trail shown as the bubble has moved up the domain and deposited the particles there.

Figure 4.2 shows the concentration polarisation more clearly in the central plane perpendicular to the membrane. The concentration only within 10 microns is shown. Again, we see reduced concentration polarisation in the region where the liquid film between bubble and membrane is present and again lower down in the wake region. The reduction in the thickness of the high concentration region will result in a lower resistance allowing higher fluxes.

4.3 Flux

Figure 4.3 shows the flux through the membrane. The correlation between the bubble dynamics and particle concentration are clear. In the lower concentration regions near the bubble and in the wake, the flux is higher. The region to the side where the particles are redeposited by the rising bubble suffers from lower flux.

Figure 4.4 shows the flux enhancement for the 3.075mL bubble in a 8 mm gap. The ratio of the fluxes settles to reveal the increase due to the presence of the bubble. Figure 4.5 shows the flux enhancement with respect to gap for bubbles of volume, 3.075mL, 4.950mL, 7.032mL,12.350mL. For the three larger bubbles there is a peak in the flux enhancement. This is due to the competing effects of shear and gas volume fraction. As the gap is reduced, the shear increases which promotes greater flux. The size of the bubble relative to the flow area also increases which leads to a reduction of space for the particles to mix resulting in particle build up reducing flux.

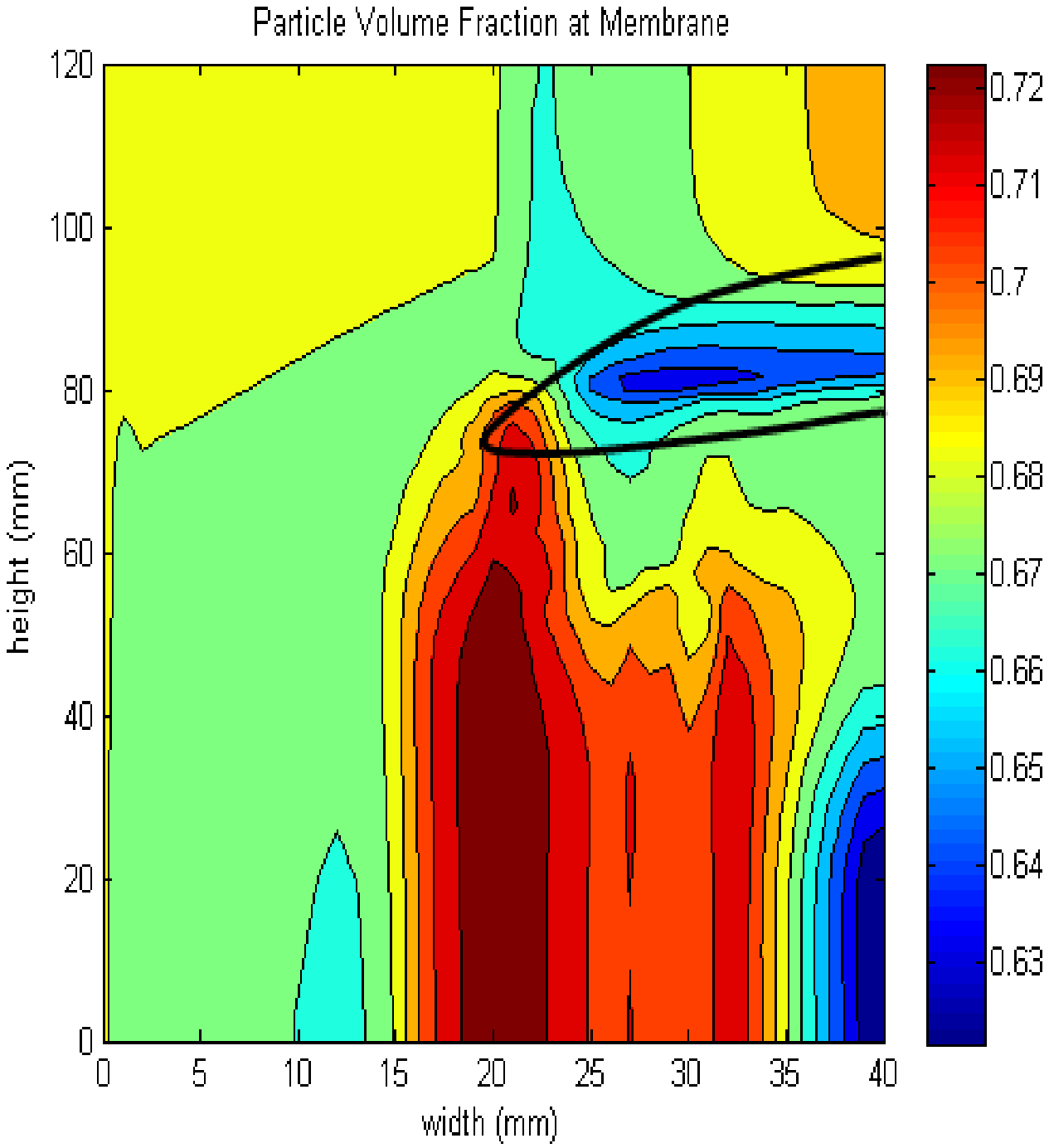

Figure 4.1: Particle volume fraction on the membrane in the presence a 3.075mL bubble in a 8mm gap, the black line shows the position of the bubble. Transmembrane pressure, $TMP = 100kPa$. Particle diameter $d_p = 0.2\mu m$. Clean water resistance $R_m = 2.5\text{x}10^{12}m^{-1}$. Bulk concentration $c_b = 15g/L$

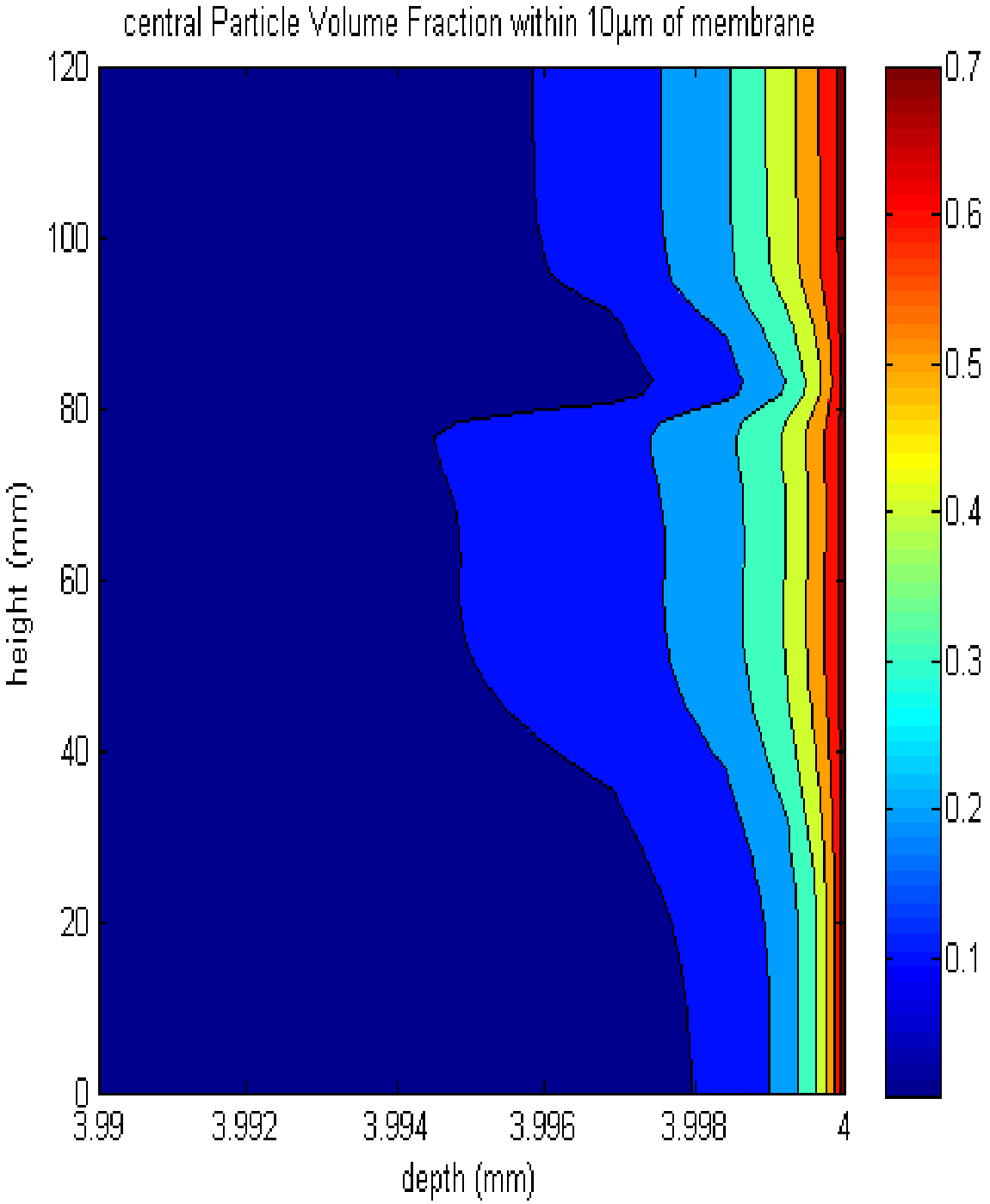

Figure 4.2: Particle volume fraction perpendicular to membrane within 10 microns in the presence a 3.075mL bubble in a 8mm gap, the black line shows the position of the bubble. Transmembrane pressure, $TMP = 100kPa$. Particle diameter $d_p = 0.2\mu m$. Clean water resistance $R_m = 2.5\text{x}10^{12}m^{-1}$. Bulk concentration $c_b = 15g/L$

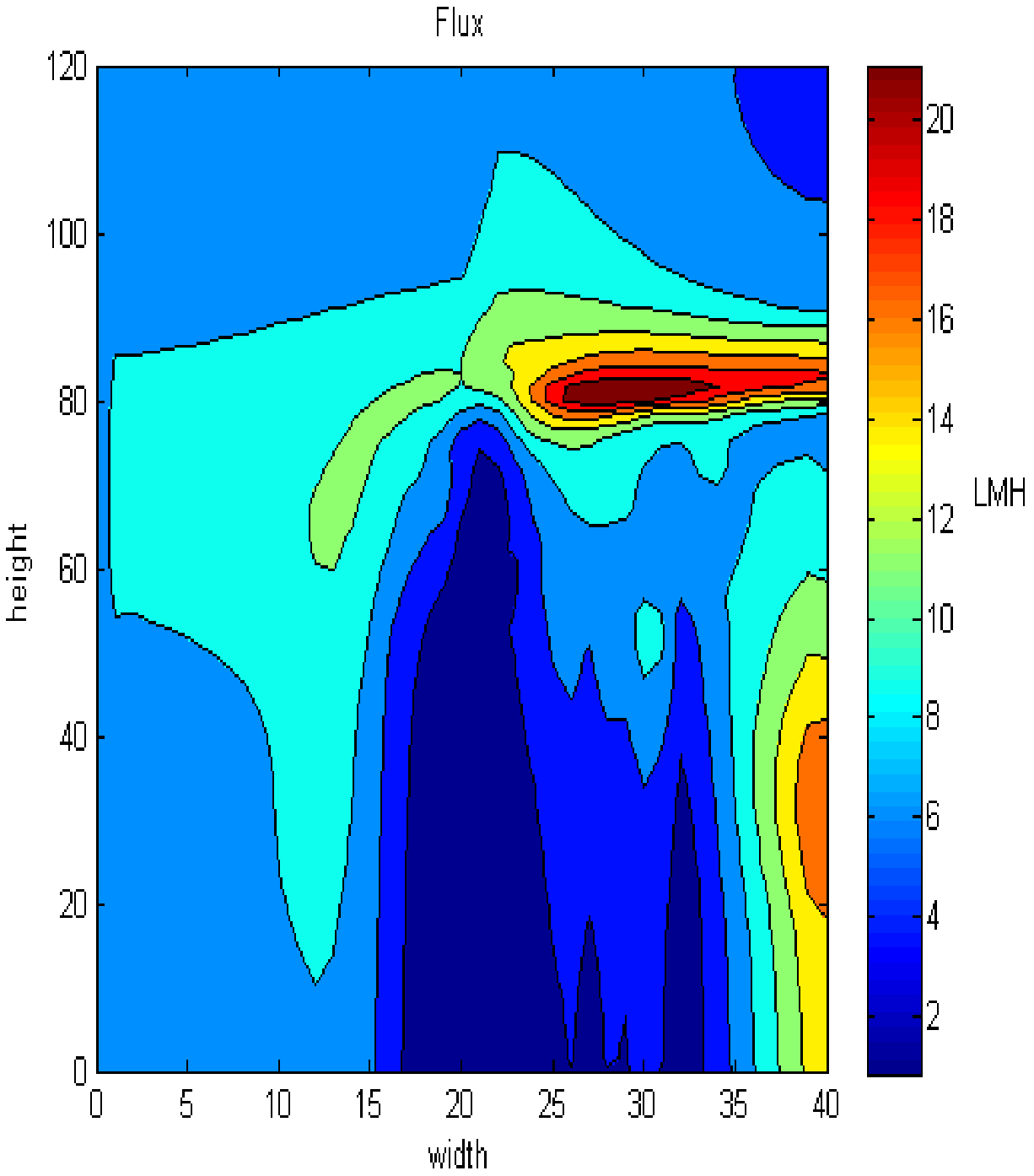

Figure 4.3: The flux through the membrane. Transmembrane pressure, $TMP = 100kPa$. Particle diameter $d_p = 0.2\mu m$. Clean water resistance $R_m = 2.5\text{x}10^{12}m^{-1}$. Bulk concentration $c_b = 15g/L$. High flux regions include the bubble film and wake, whilst the region where particles are deposited to the side as they pass the bubble suffers from low flux as a result.

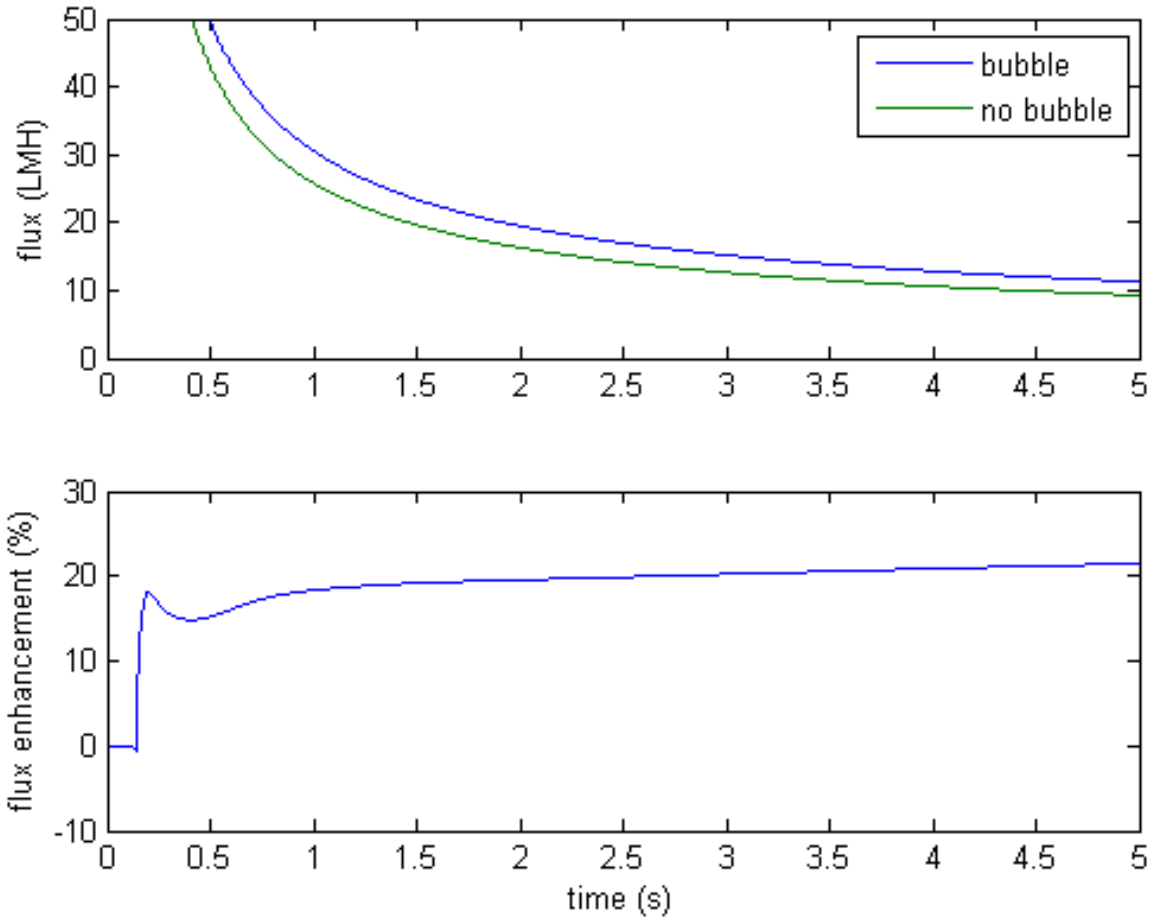

Figure 4.4: Convergence of the flux enhancement for the 3.075mL bubble in a 8 mm gap.

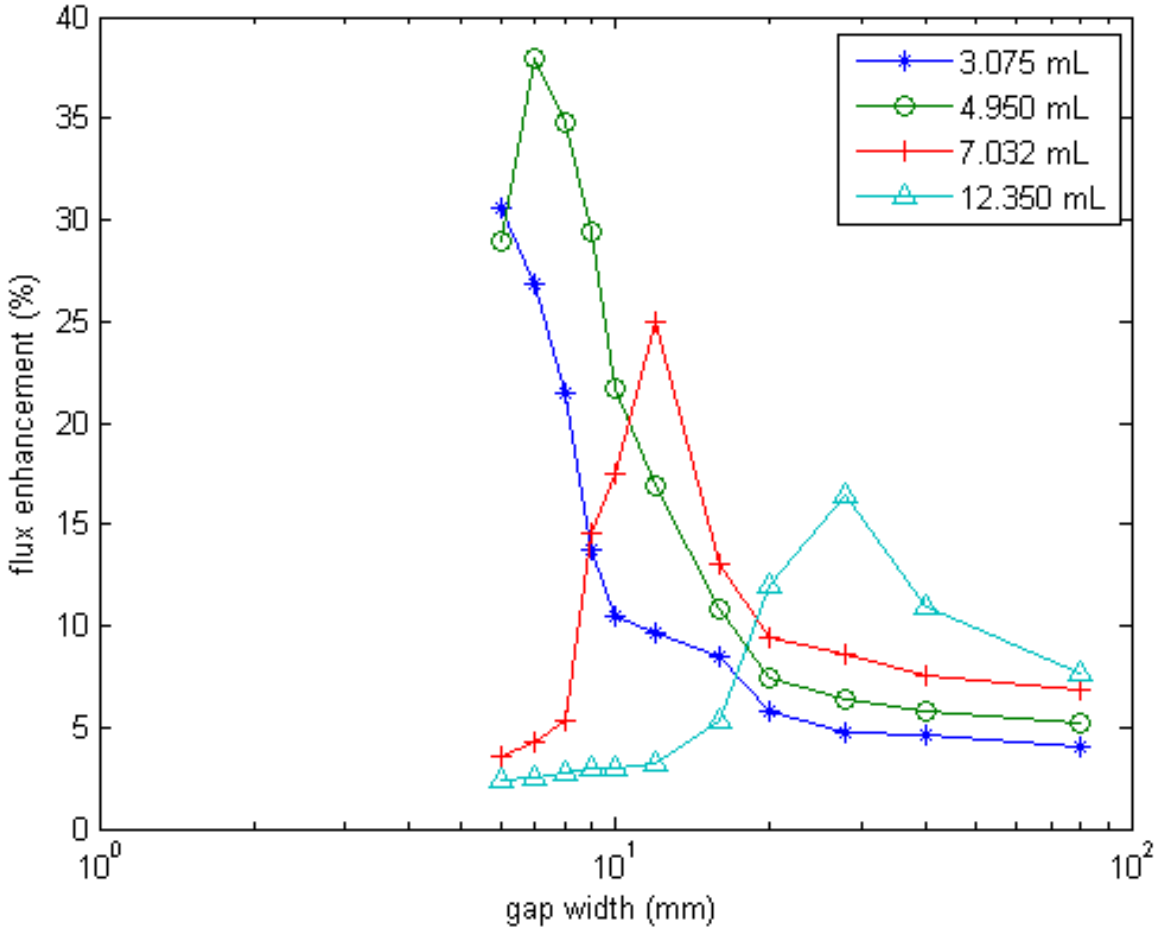

Figure 4.5: The flux enhancement for each bubble volume with respect to gap. The three larger bubbles suffer a reduction in flux as the bubble size compared to the flow area becomes too large and causes flow constriction and particle build up. When the bubble size is smaller the flux increases with shear as would be expected.

The flux for a given bubble when the gap is varied is now calculated. Figure 4.5 shows the influence on the flux performance. The enhancement is calculated compared to the case where no bubble is present. We see how as the gap is reduced the performance increases as the bubble has greater influence on the membrane surface. The enhancement is not significant until the gap is reduced to 10mm. The bubble shapes depicted in Figure 3.26 show that the bubble length, for the 3.075 mL volume, is largely constant down to the 12mm gap. For the 10,9,8mm gaps however the bubbles are elongated by the constraint of the gap generating a significant liquid film region between the bubble and membrane. The length of this region allows for an acceleration of the downward film generating increased shear and mass transport away from the membrane.

As the bubble volume increases and takes up more space in the domain, a reduction in the flux enhancement can occur. Figure 4.7 shows the particle concentration at the membrane surface with a 12mm gap. Figure 4.6 shows the particle concentration at the membrane surface with a 8mm gap. As the gap reduces to 8mm, the bubble will require more space in the plane parallel to the membrane to maintain its gas volume. This results in an extra build up in concentration to the side of the bubble. The particles are pushed to the side by the bubble, but there is not sufficient space for them to disperse resulting in a large concentration build up and less flux.

Figure 4.8 shows the correlation between flux and shear. At lower gas volume fractions, the correlation is strong, indicating that the shear is the significant influence on the performance. However, in the high shear and high gas volume fraction region, the correlation deteriorates as other influences become more significant. The restriction to particle flow caused by the bubble size becomes the significant factor.

Figures 4.9 & 4.10 show the particle concentration on the membrane surface with respect to gap for the bubble volumes 3.075mL and 7.032mL respectively. The smaller bubble enjoys a continuous decrease in concentration with decreasing gap. However, the larger bubble clearly suffers from an increase in concentration after 12mm, due to the constriction of particle flow space between the bubble and the side walls. This is also shown in the results for flux shown in Figures 4.11 & 4.12.

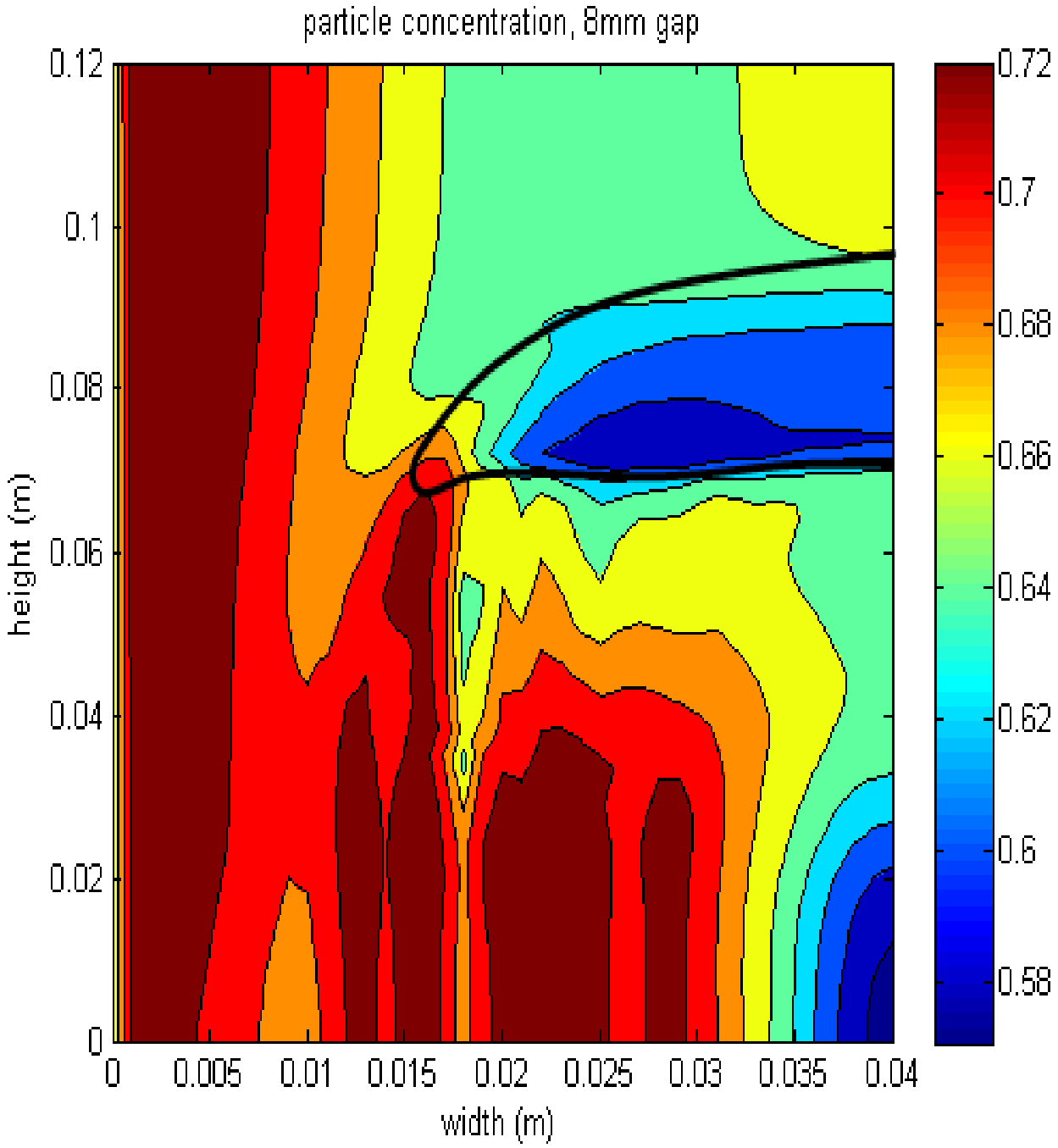

Figure 4.6: Particle concentration at the membrane surface with a 8mm gap in the presence a 7.035mL bubble, the black line shows the position of the bubble. Note the extra build up of particles by the side wall due to the constriction of the bubble, resulting in reduced flux.

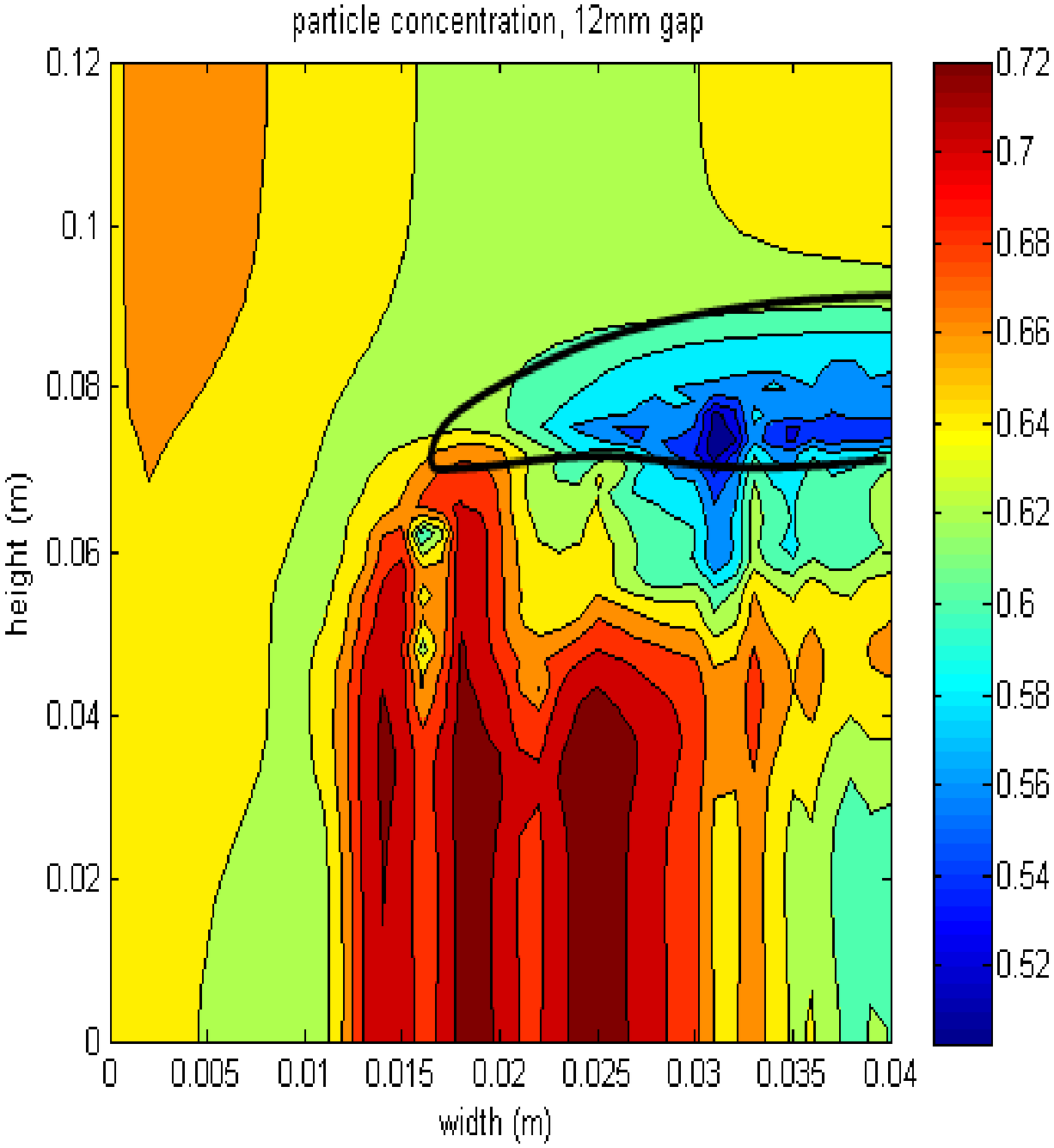

Figure 4.7: Particle concentration at the membrane surface with a 12mm gap in the presence a 7.035mL bubble, the black line shows the position of the bubble.

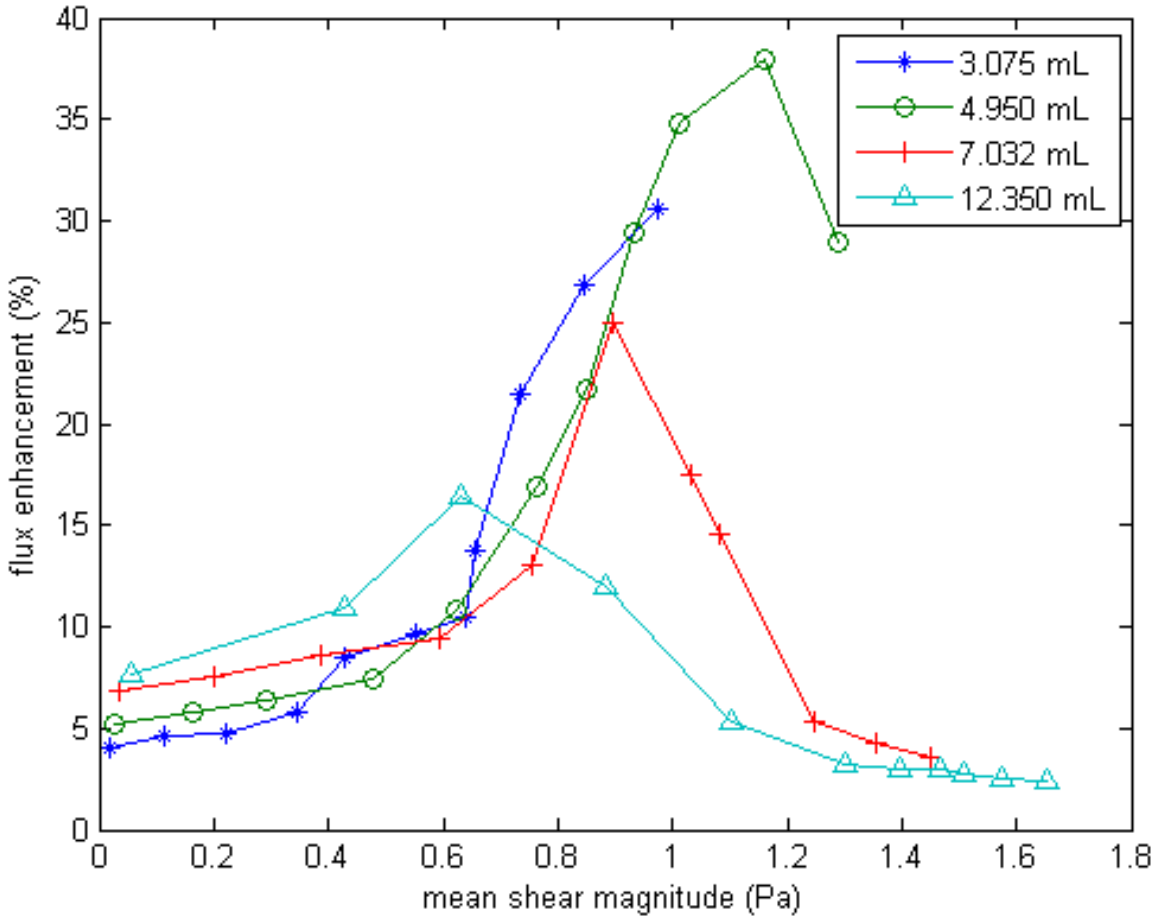

Figure 4.8: In the low shear region, where the bubble width is sufficiently small compare to the flow width, there is strong correlation with flux. However, in the higher mean shear region, the flow constriction become more significant and there is no correlation.

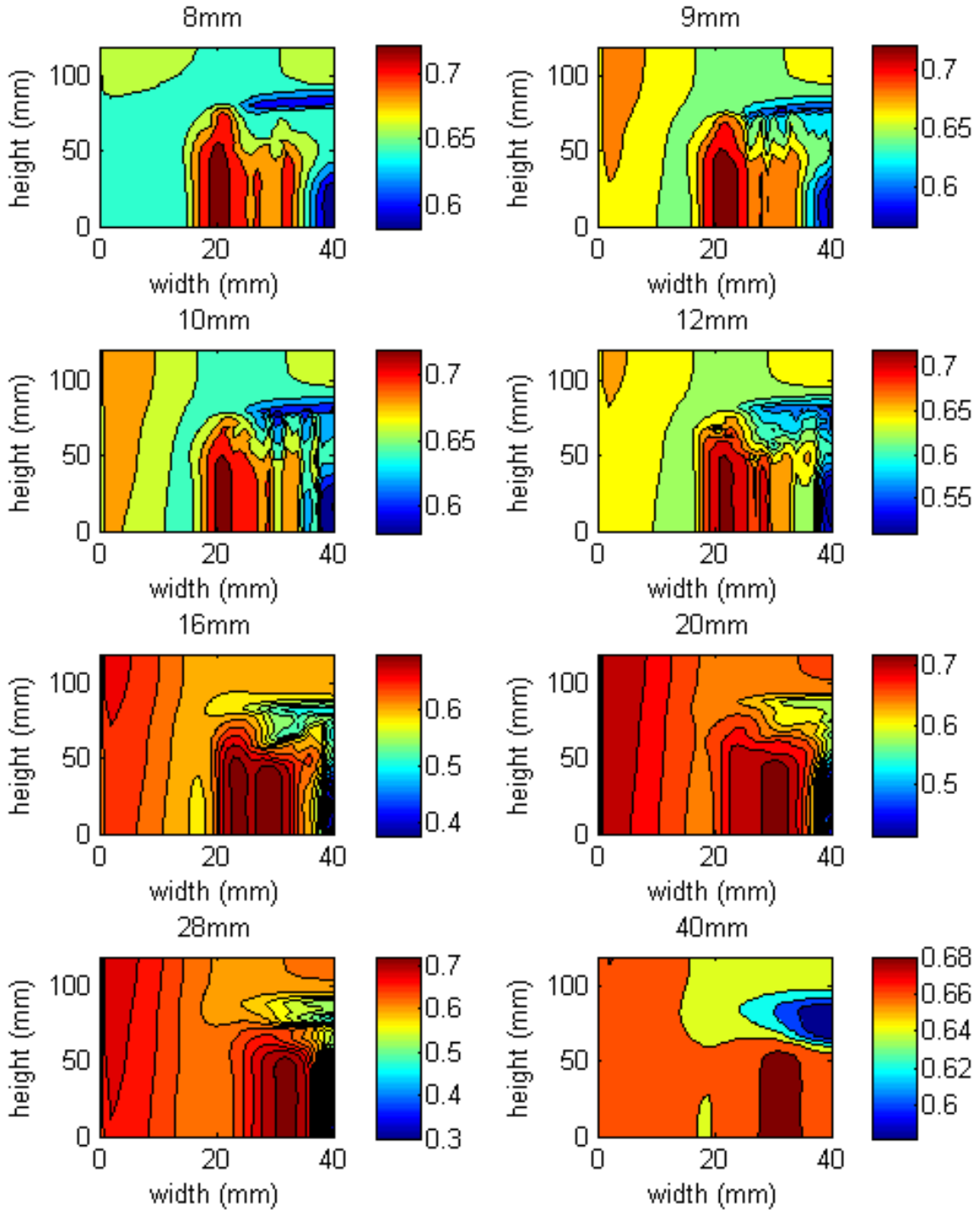

Figure 4.9: The particle concentration on the membrane for a 3.075 mL bubble by gap depth.

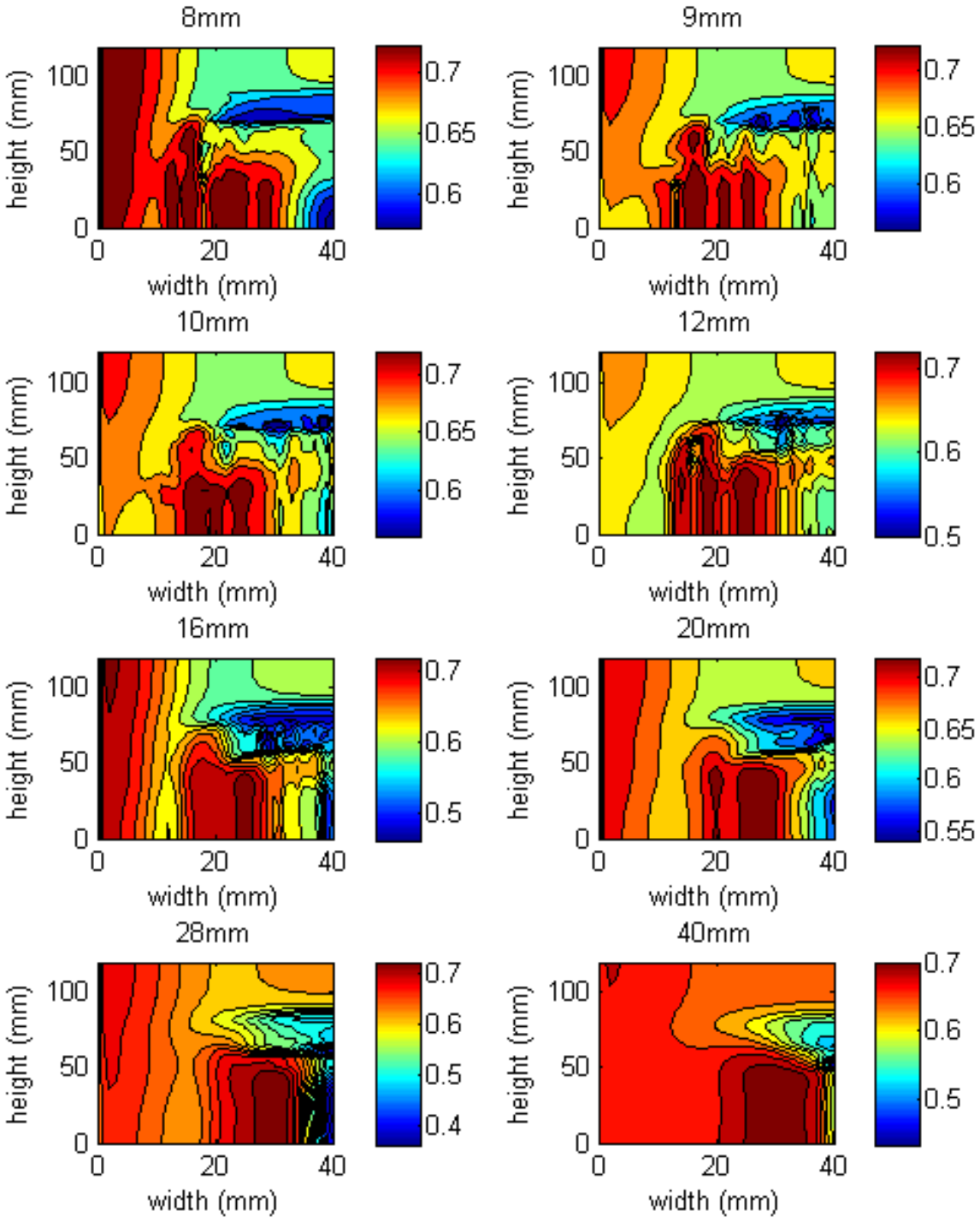

Figure 4.10: The particle concentration on the membrane for a 7.032 mL bubble by gap depth.

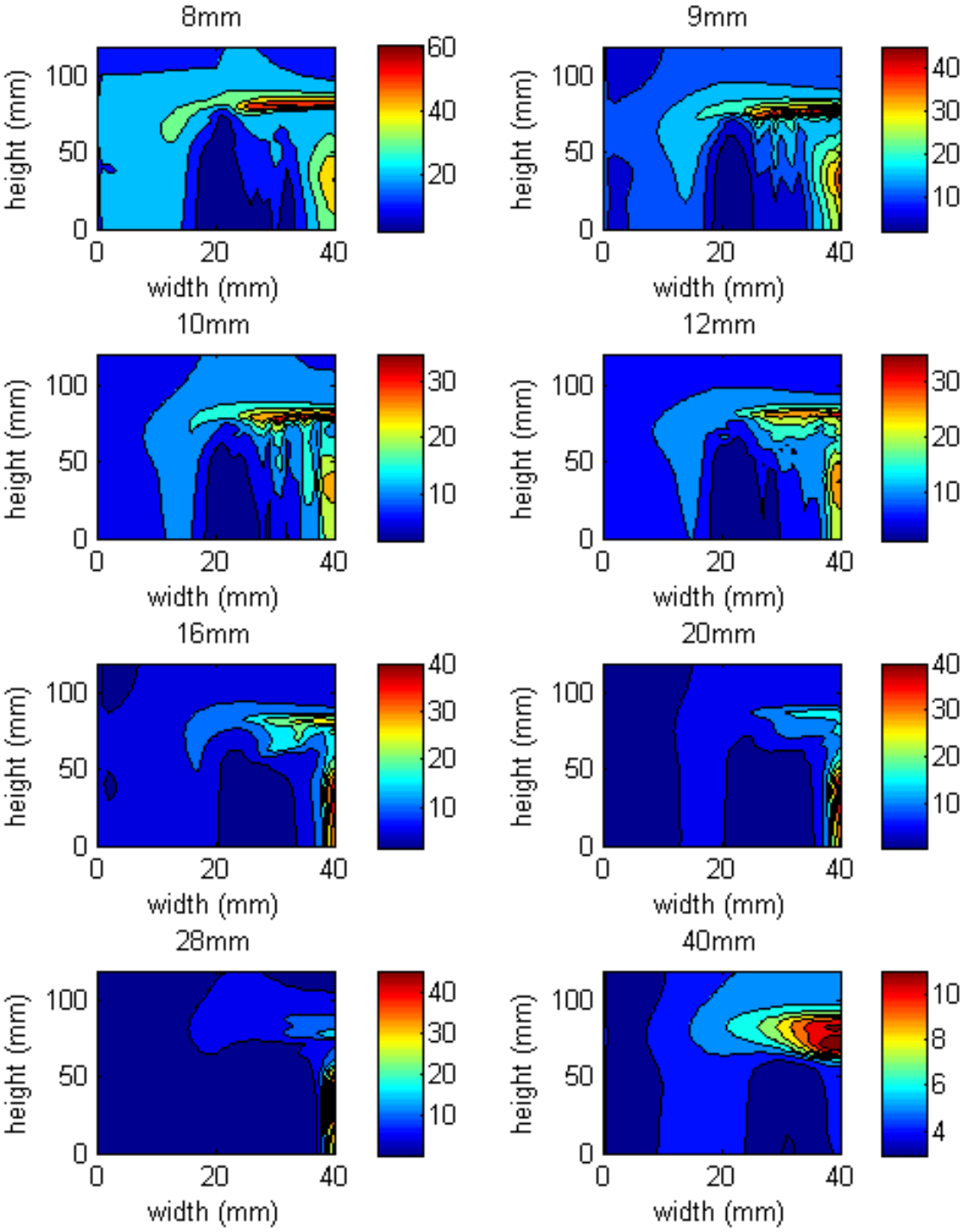

Figure 4.11: The flux enhancement (%) through the membrane for a 3.075 mL bubble by gap depth.

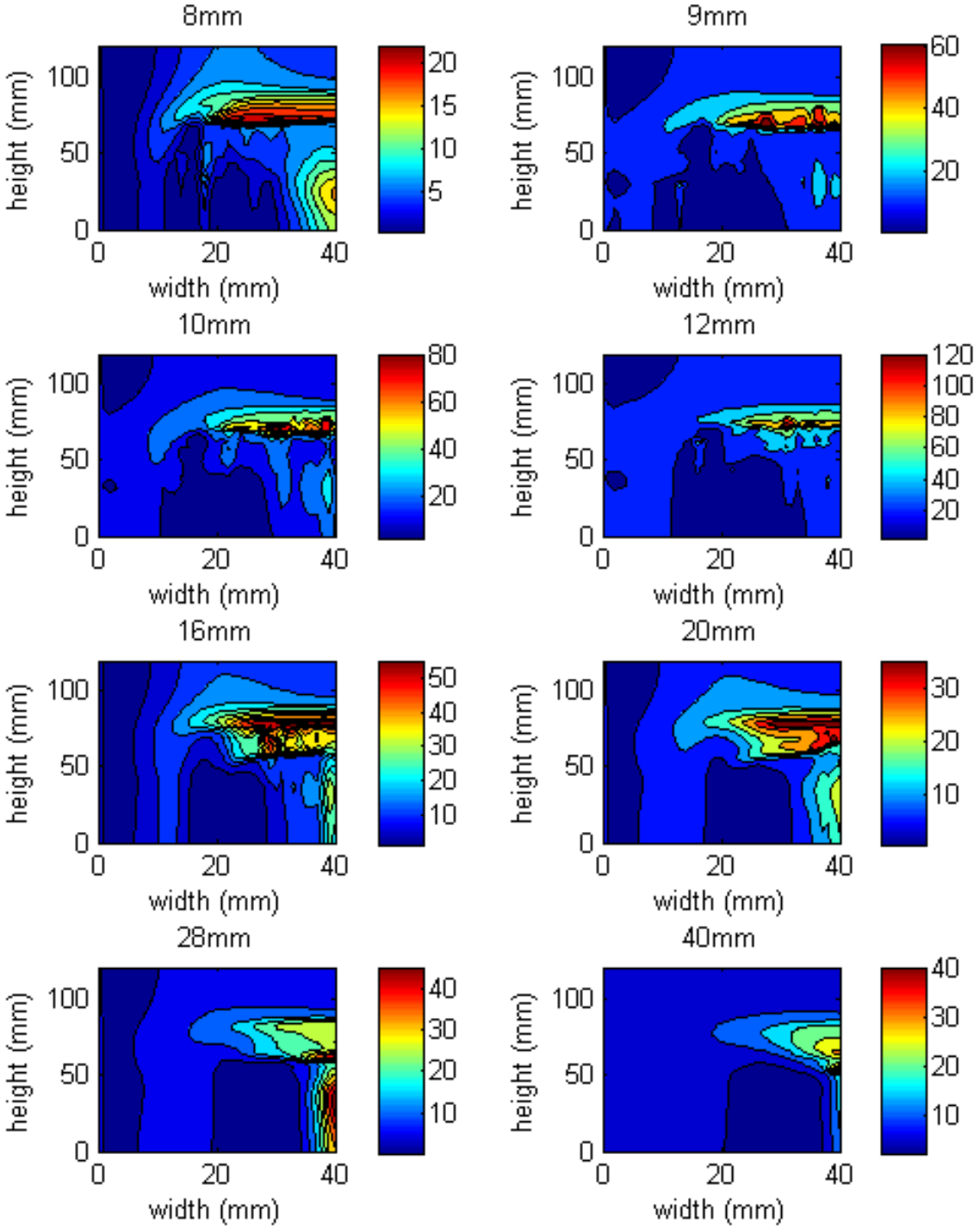

Figure 4.12: The flux enhancement (%) through the membrane for a 7.032 mL bubble by gap depth.

4.4 Flux Optimisation Design

For different bubble sizes, the peak in flux occurs at different gaps. Figure 4.13 compares the fraction of bubble width to domain width, in x, with the flux enhancement. The peaks in flux all occur in the region where the width of the bubble is between 58% and 65% of the domain width.

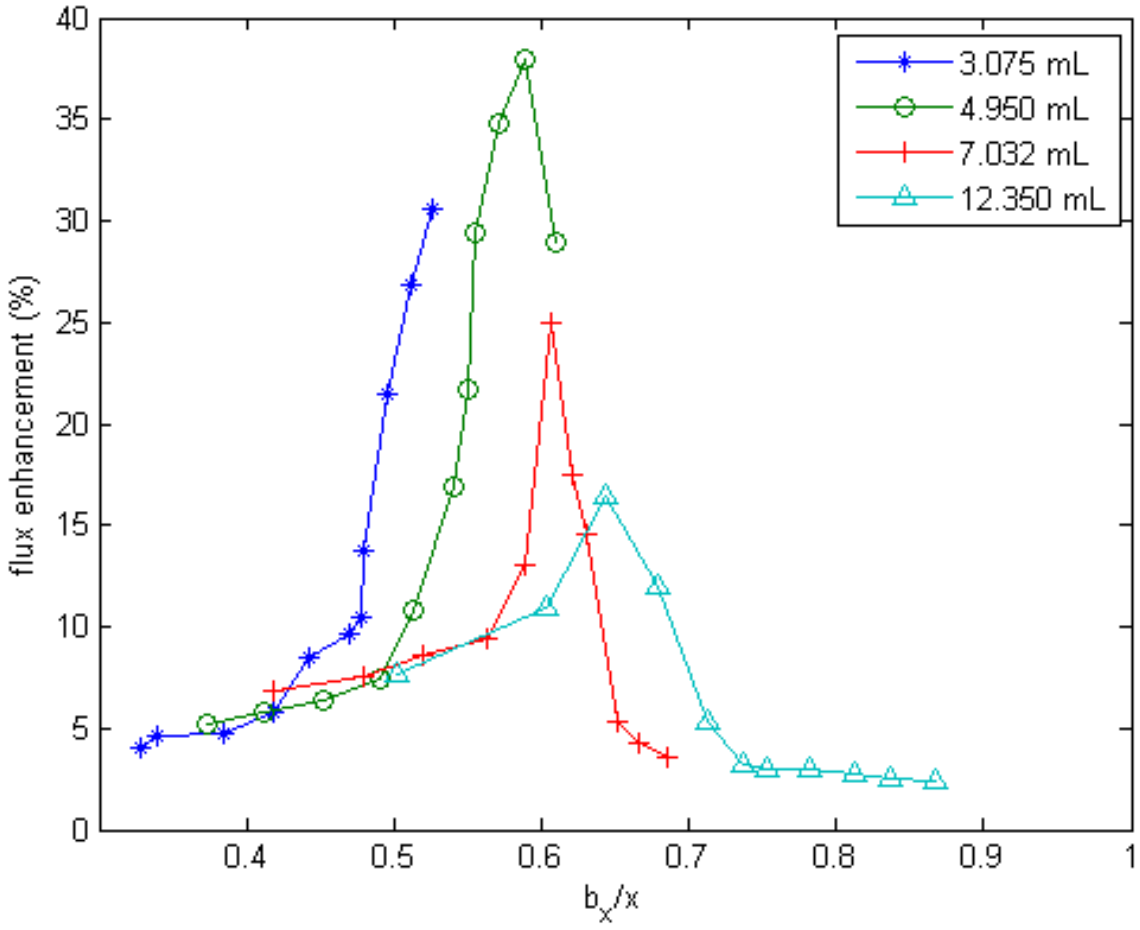

Figure 4.13: For each bubble volume, the peak in flux enhancement is grouped around the region where the bubble width is 60% of the flow width (b_x/X). Experimental results for flat sheet filtration focus on bubble volume and sparging frequency without recording the bubble width. As such no experimental confirmation of this result currently exists.

Figure 4.14 shows the influence of the fraction of bubble depth in z direction on flux enhancement. Here the data is less clear, as the higher flux regions are all in the region where the bubble depth is greater than 90%.

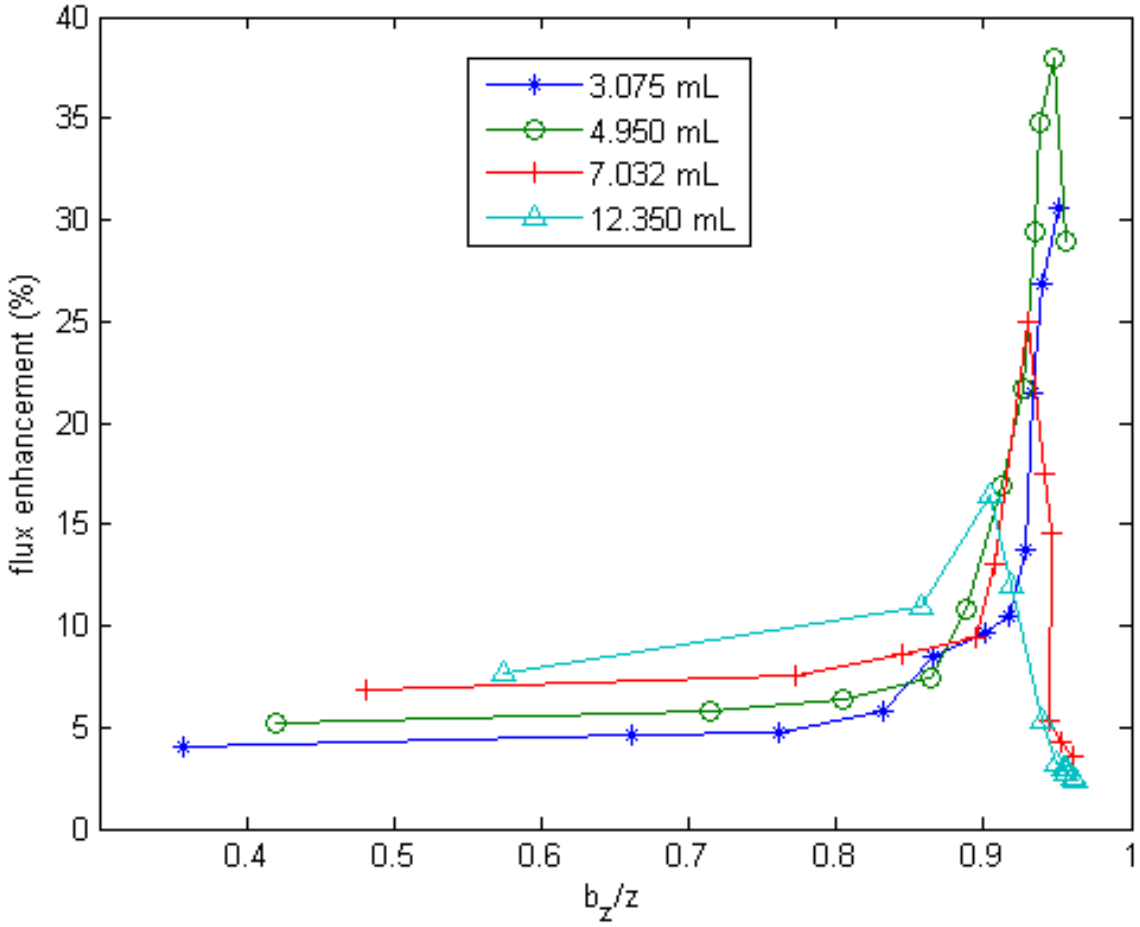

Figure 4.14: Notable flux enhancement only occurs, for each bubble volume, after the depth of the bubble exceeds 85% of the gap (b_z/z).

Figure 4.15 combines the above two approaches by comparing the ratio of the product of bubble width by depth to flow area. As in the case of the bubble width in x, there is a clear agglomeration of peak performance where the fraction is around 60%. It is important to note that this is for bubble which are slugged in the z direction, i.e. occupy over 90% of the gap in z. For the domain sizes and bubble volumes investigated the it is clearly desirable to ensure the system will run in this region. This proportion appears to be the optimum for the balancing of flux and flow considerations. The domain width in this work is 80mm. Wider

systems would likely benefit from multiple gas sparging locations along its base. Indeed it may be that for this domain would also benefit from mulitple smaller bubbles, but this work is restricted to single bubble analysis only.

Given the weak horizontal interaction shown in the above section on CFD, it is considered that one may scale up these results to larger systems. For example a system with a width of 160mm would be well served with two sparging points evenly separating bubbles whose width occupies 30% of the membrane width each. In addition the height of the membrane is chosen to be sufficient to allow the exit flow to be largely independent of the bubble but not so large as to mask the effect of the bubble, one may scale up to taller membranes in a similar way.

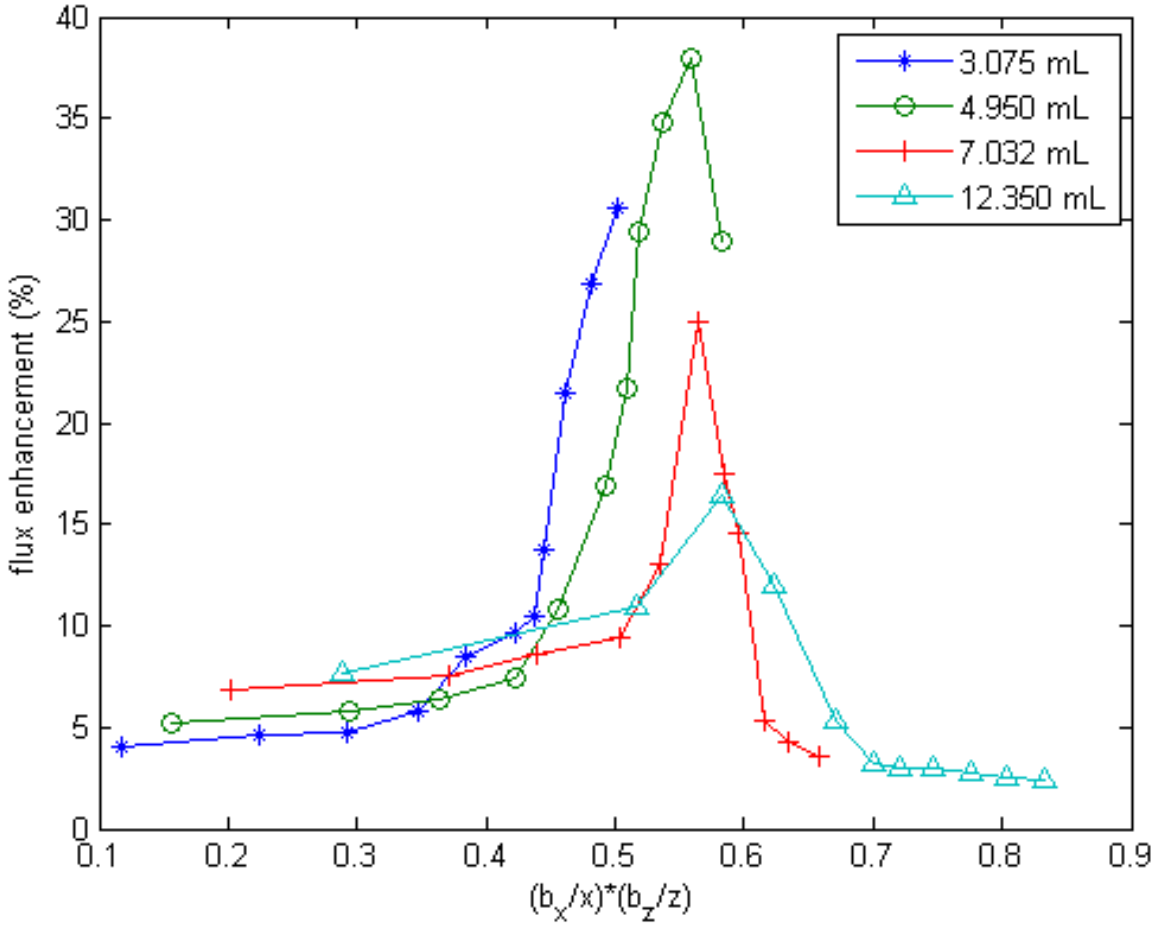

Figure 4.15: A strong correlation occurs between the peaks in flux and the region where the product of the relative bubble depths and widths, $\frac{b_x b_z}{XZ}$, is 55%.

To ensure the bubble width is around the desirable 60% of the membrane width, the designer can refer to the earlier figures showing the bubble shape compared to a hemisphere and hemicylinder. For a given gap, the resultant bubble width can be calculated for a given bubble volume. This will require some iteration to find the optimal volume as no analytical solution is apparent. First estimate the volume, V, of the desired bubble then convert this to the equivalent diameter for a hemisphere, d_x. Then divide this by the desired bubble width, $b_x = 0.6X$, to get the shape factor. Then read off the fraction of the bubble depth to gap, b_z/Z, from Figure 3.23, this will give the bubble depth, b_z, and aspect ratio, b_x/b_z. If this conforms to the results in Figure 3.24 then the bubble volume will give the desired result. In the likelihood that the first estimate will be incorrect, adjust the initial estimate then check again until the desired bubble geometry is achieved. The method for designing the desired bubble width (60%) is detailed below.

1. Estimate the desired bubble volume, V.
2. Calculate the equivalent hemisphere diameter, $d_x = (12V/\pi)^{1/3}$
3. Calculate the shape factor, SF $= d_x/b_x = d_x/(0.6X)$.
4. Read off the fraction of the bubble depth to gap, b_z/Z, from Figure 3.23.
5. Calculate b_z and hence b_x/b_z from result of 4.
6. If b_z and b_x/b_z match the results given in Figure 3.24 then V is correct. If not adjust initial guess for V and repeat process.

5 Conclusions and Future Work

5.1 Conclusions

5.1.1 Particle and Flux Model

In this work, a flux model was developed based on particle behaviour that can calculate the beneficial effects of bubbling in membrane filtration. The flux-convection-diffusion model was first tested against single phase crossflow to provide validation with known theory. Strong correlation was found with respect to crossflow velocity. The model's close attention to the interaction between the boundary layer and cake layer provides a more sophisticated view of the particle behaviour. In established theory, when the particle concentration at the membrane reaches maximum the flux will be independant of transmembrane pressure. However, the model has shown that the concentration polarisation boundary layer is not constant for all transmembrane pressures when the maximum concentration has been obtained. Once the max concentration has been reached, further pressure increases result in a thickening of the boundary layer. This retards the growth of the cake layer resulting in a more even distribution of the particle concentration. This is significant as an even distribution has a lower resistance than one where the particle concentration is more densely packed, as the relationship between resistance and concentration is non-linear. This results in a higher flux in the transitional region between negligible resistance and cake dominated resistance. As the pressure is increased further however, the boundary layer reaches a maximum and actually reduces slightly in size. This promotes growth of the cake layer and the flux reduces to that predicted using old theory. When the particle size is varied the significance of the boundary layer is strongly affected. For the smaller particle sizes, the boundary layer resistance becomes more significant as there is greater surface area per volume contributing to the resistive drag. Smaller particle sizes actually promote a thicker boundary layer as the development of the cake layer is retarded, as shown in Figure 2.16.

5.1.2 Gas-Liquid Flow Between Two Parallel Flat Sheets

The shape and rise velocity of the bubbles between two flat sheets was calculated using the volume of fluid method. The bubble shape predicted showed good correlation with that seen from experiment between two bubbles of a similar Eotvos number. The overall shape of the

bubble was evaluated by comparing the calculated bubble width with the width of a perfect hemisphere and hemicylinder of the same volume. For the large gap widths where the depth of the bubble in z was relatively small, less than 80% of the total depth, Z, the correlation between the bubble width and the hemisphere width was strong. Likewise the correlation between the hemicylinder and the bubble was strong when the depth of the bubble in z exceeded 90% of the gap width Z . The bubble width was typically higher than both the hemisphere and hemicylinder indicating a more concave shape. However, for small values of Z, less than 8mm, the width was less indicating the bubble shape had become convex. This is a result of the increased significance of surface tension effect which occurs for smaller length scales. Compare, for example, the spherical bubble for very small gas volumes, where surface tension is dominant.

The bubble rise velocity was described in three regions. For larger gap widths the bubble rise velocity was highest as it is unconstrained and drag on the walls in insignificant. A reduction in gap width in this region causes a reduction in the bubble rise velocity due to the increased influence of drag on the walls. However, as the gap width continues to decrease the bubble rise velocity moves into another characteristic region. Once the film width between bubble and wall is largely steady the shape of the bubble undergoes significant change. The result is a more streamlined shape which actually causes an increase in the bubble rise velocity as the liqud phase can flow around the bubble more easily. From this region further gap constriction results in the bubble width becoming significant in the x direction compared to the width of the flat sheets. This moves the velocity into a the third region where the bubble rise velocity starts to decrease again with reduction in gap width. This is due to the drag now exerted by the side walls containing the flow in the x-direction. The rise velocity is now characterised by the width of the bubble in the x-direction not the z-direction as before. For the larger gap widths the results conform well to experimental results for unconstrained flow and similarly for small gap widths they conform well to results for 2D or very narrow gap results. In between there is a general shift between the two results as the gap width is decreased. However, this is not continuous as the streamlining effect increases the velocity when the reduction in gap width would indicate a reduction in velocity due to the greater restriction in x. Given the analysis was done for a given bubble volume and varying gap widths in z, it was useful to define the dimensionless diameter based on a cylinder of depth equal to Z.

5.1.3 Flux Enhancement for Bubbling Membrane Filtration

The particle - flux model and the CFD calculation work is combined to find the flux enhancement due to the presence of the bubble between two flat sheet membranes. The particle concentration near the membrane is a result of the hydrodynamics of the gas-liquid flow. In the film between the slugged bubble and the membrane there is a low concentration due to the higher shear in this region. Likewise the wake region also enjoys low particle concentration. The downward flow around the bubble results in a high concentration region below the outer edge of the bubble. The particles must move around the bubble and are channelled into this region. The flux enhancement is highest in the region of low concentration.

As the gap width is reduced the associated increase in shear results in higher flux enhancement. However, for a given bubble size if the gap is reduced too small then the enhancement starts to decrease. When the width of the bubble becomes too significant compared to the width of the domain there is little room for the particles to flow around the side of the bubble. As a result high concentrations build up by the side walls and into the bulk. This decreases the flux enhancement. For each bubble volume the flux enhancement was shown to deteriorate when the bubble width exceeded 60% of the membrane width. This clearly shows the limitation of relying solely on the induced shear to calculate the flux enhancement. Only when the bubble width is sufficiently small is their strong correlation between shear and flux.

A design method is proposed to ensure the optimal flux for a given gap and geometry. Correlations for bubble sphericity and aspect ratio found in the CFD calculation are used. These correlations can be employed to find the bubble volume that will give the desired bubble characteristics and maximise flux performance.

5.2 Future Work

The results here suggest that bubble sizes beyond the scope of this investigation may achieve even better flux enhancement. In particular, smaller bubble volumes in smaller bubble widths. Further work to calculate the hydrodynamics and resulting flux using the same techniques would provide greater insight into the potential benefits to flux enhancement. When calculating the flux this work uses a Lagrangian method for a single bubble. Difficulties arise when multiple bubbles are calculated in the CFD method. This is due to their interaction which will prevent a steady state being formed until they have coalesced or no longer interact. To

consider transient effects for multiple bubble systems a time averaged approach may prove revealing. For a given frequency of bubbling the period could be found, and the average flux taken over that time calculated. These calculations for bubble interaction are performed in this work two dimensionally but no flux calculation can be obtained as there can be no mass transfer in the direction of the flux as this dimension is not included. To perform a fully three dimensional transient multi-bubble system could be done using the techniques developed here providing greater insight. However, this would be exceptionally demanding computationally and would require significant time and resources.

If however the multiple bubble CFD calculations were carried out using an Eulerian method this would allow for much quicker computation time. This however relies on simplifications to the bubble type and geometry. For example the bubble diameters are fixed and no interface calculations are undertaken to investigate bubble shape. This approach has been attempted by Ndnisa [75]. The resulting flow field could then be used for calculating the flux in a system with many bubbles, the bubble size would necessarily be much smaller. In the literature review examples of using control theory in the frequency domain for bubbling systems are given [80]. The sparger introducing the gas was controlled this way to match some desired pressure requirement. Again this would be very expensive to use a Lagrangian system but a eulerian approach would be possible. The shear at the membrane surface can be measured for a given bubbling system and then analysed in the frequency domain to find the transfer function. A controller transfer function for the gas input can then be employed to achieve a desired shear response, although the energy cost of this control system would have to be taken into account.

More experimental work to link bubble behaviour and flux in flat sheet membrane systems is required. Current results either focus on bubble behaviour and the flow it induces but not the flux [10], or calculates flux but only for a given gas flow rate not the bubble size [67, 8]. The energy cost associated with the bubbling should also be recorded to determine whether the benefit to flux from the gas sparging is achieved at a lower energy cost than alternative methods of increasing flux.

References

[1] Zhiqiang Zhao. Cfd study on hydraulic characteristics of the submerged mebrane bioreactor process. Transfer Report.

[2] H. Shino, K. Nishimori, S. Kawakami, T. Uesaka, and K. Izumi. Introduction to submerged flat sheet membrane applications and its future direction. Kubota Corporation.

[3] Richard W. Baker. *Membrane Technology and Applications*. Wiley, second edition, 2004.

[4] R. Ghosh and Z. F. Cui. Mass transfer in gas-sparged ultrafiltration: upward slug flow in tubular membranes. *Journal of Membrane Science*, 162:91–102, 1999.

[5] E. Tardieu, A. Grasmick, V. Geaugey, and J. Manem. Hydrodynamic control of bioparticle deposition in a mbr applied to wastewater treatment. *Journal of Membrane Science*, 147:1–12, 1998.

[6] P. B. Whalley. *Boiling Condensation and GasLiquid Flow*. Clarendon Press, Oxford, 1987.

[7] Z. F. Cui, S. Chang, and A. G. Fane. The use of gas bubbling to enhance membrane processes. *Journal of Membrane Science*, 221:1–35, 2003.

[8] K. Essemiani, G. Ducom, C. Cabassud, and A. Line. Spherical cap bubbles in a flat sheet nanofiltration module: experiments and numerical simulation. *Chemical Engineering Science*, 56:6321–6327, 2001.

[9] R. Clift, J. R. Grace, and M. E. Weber. *Bubbles, Drops and Particles*. Academic Press, New York, 1978.

[10] Kaisong Zhang, R. W. Field, and Z. F. Cui. Hydrodynamic characteristics in flat sheet mbr system: 1.effect of bubble size and frequency. Unpublished.

[11] K. Zhang, Z.F. Cui, and R.W. Field. Effect of the bubbling regimes on the performance and energy cost of flat sheet mbrs. *Desalination*, 332(1-2):30–37, 2011.

[12] R. Krishna, J. M. van Baten, M. I. Urseanu, and J. Ellenberger. Rise velocity of single circular–cap bubbles in two–dimensional beds of powders and liquids. *Chemical Engineering and Processing*, 39:433–440, 2000.

[13] A. Jonsson and G. Tragardh. Fundamental principles of ultrafiltration. *Chemical Engineering and Processing*, 27:67–81, 1990.

[14] C. J. D. Fell, K. J. Kim, V. Chen, D. E. Wiley, and A. G. Fane. Factors determining flux and rejection of ultrafiltration membranes. *Chemical Engineering and Processing*, 27:165–173, 1990.

[15] Z. F. Cui. Experimental investigation on enhancement of crossflow ultrafiltration with air sparging. In R. Paterson, editor, *Effective Membrane Processes – New Perspectives*, page 237, London, 1993. Mechanical Engineering.

[16] Z. F. Cui and K. I. T. Wright. Gas-liquid two-phase cross-flow ultrafiltration of bsa and dextran solutions. *Journal of Membrane Science*, 90:183–189, 1994.

[17] A. R. Da Costa, A. G. Fane, C. J. D. Fell, and A. C. M. Franken. Optimal channel spacer design for ultrafiltration. *Journal of Membrane Science*, 62:275–291, 1991.

[18] Z. Cao, D. E. Wiley, and A. G. Fane. Cfd simulations of net-type turbulent promoters in a narrow channel. *Journal of Membrane Science*, 185:157–176, 2001.

[19] S. Judd. Submerged membrane bioreactors: flat plate or hollow fibre? *Filtration & Separation*, 39(5):30–31, 2002.

[20] G. Tchobanoglous, F. L. Burton, and H. D. Stensel. *Wastewater engineering treatment and reuse*. McGraw–Hill, fourth edition, 2003.

[21] B. Gunder and K. Krauth. Replacement of secondary clarification by membrane separation - results with plate and hollow fibre modules. *Water Science and Technology*, 38(4):383–393, 1998.

[22] N. F. Gray. *Biology of wastewater treatment*. Oxford University Press, New York, 1989.

[23] K. Yamamoto, M. Hiasa, T. Mahmood, and T. Matsuo. Direct solid–liquid separation using hollow fibre membrane in an activated sludge aeration tank. *Water Science Technology*, 21:43–54, 1989.

[24] C. Visvanathan, R. Ben Aim, and K. Parameshwaran. Membrane separation bioreactors for wastewater treatment. *Critical Reviews in Environmental Science and Technology*, 30(1):1–48, 2000.

[25] S. Chang, A. Fane, and S. Vigneswaran. Modeling and optimizing submerged hollow fiber membrane modules. *AIChE Journal*, 48(10):2203–2212, 2002.

[26] K. Fujita and S. Takizawa. Study on hydraulics of backwashing and air-scrubbing in hollow fiber filtration. *Journal of Japan Water Works Association*, 63(3):94–101, 1994.

[27] Z. F. Cui, S. R. Bellara, and P. Homewood. Airlift crossflow membrane filtration - a feasibility study with dextran ultrafiltration. *Journal of Membrane Science*, 128:83–91, 1997.

[28] G. L. Morrison, T. I. Zeineddine, M. Henriksen, and G. B. Tatterson. Experimental analysis of the mechanics of reverse circulation air lift pump. *Ind. Eng. Chem. Res.*, 26:387–391, 1987.

[29] Y. Lee and M. M. Clark. Modeling of flux decline during crossflow ultrafiltration of colloidal suspensions. *Journal of Membrane Science*, 149:181–202, 1998.

[30] Y. Lee and M. M. Clark. A numerical model of steady-state permeate flux during cross-flow ultrafiltration. *Desalination*, 199:241–251, 1997.

[31] R. H. Davis and D. T. Leighton. Shear induced transport of a particle layer along a porous wall. *Chemical Engineering Science*, 42(2):275–281, 1987.

[32] G. Belfort. Fluid mechanics in membrane filtration: Recent developments. *Journal of Membrane Science*, 40(2):123 – 147, 1989.

[33] G. Segre and A.J. Silbergerg. *J. Fluid Mech.*, 14(192):116.

[34] G. Green and G. Belfort. Fouling of ultrafiltration membranes: Lateral migration and the particle trajectory model. *Desalination*, 35(1 -2-3):129–147, 1980.

[35] M. C. Porter. Concentration polarization with membrane ultrafiltration. *Ind. Eng. Chem. Prod. Res. Develop.*, 11(3):234–248, 1972.

[36] Vassilis Gekas and Bengt Hallstrm. Mass transfer in the membrane concentration polarization layer under turbulent cross flow : I. critical literature review and adaptation of existing sherwood correlations to membrane operations. *Journal of Membrane Science*, 30(2):153 – 170, 1987.

[37] WH McAdams. *Heat TransmissioN*. McGraw-Hill, New York, 1954.

[38] T. Taha and Z. F. Cui. Hydrodynamic analysis of upward slug flow in tubular membranes. *Desalination*, 145:179–182, 2002.

[39] T. Taha and Z. F. Cui. Cfd modelling of gas-sparged ultrafiltration in tubular membranes. *Journal of Membrane Science*, 210:13–27, 2002.

[40] T. Taha and Z. F. Cui. Hydrodynamics of slug flow inside capillaries. *Chemical Engineering Science*, 59:1181–1190, 2004.

[41] T. Taha. *CFD Modelling of Slug Flow Enhanced Membrane Filtration.* PhD thesis, University of Oxford, 2003.

[42] R. F. Probstein. *Physicochemical Hydrodynamics: An Introduction.* John Wiley & Sons, 1994.

[43] S.S. Vasan and R.W. Field. On maintaining consistency between the film model and the profile of the concentration polarisation layer. *Journal of Membrane Science*, 279(1-2):434 – 438, 2006.

[44] R. W. Field, D. Wu, J. A. Howell, and B. B. Gupta. Critical flux concept for microfiltration fouling. *Journal of Membrane Science*, 100:259–272, 1995.

[45] P. Bacchin, P. Aimar, and R. W. Field. Critical and sustainable fluxes: theory, experiments and applications. *Journal of Membrane Science*, 281:42–69, 2006.

[46] B. D. Cho and A. G. Fane. Fouling transients in nominally sub-critical flux operation of a membrane bioreactor. *Journal of Membrane Science*, 209:391–403, 2002.

[47] H. Nagaoka, S. Ueda, and A. Miya. Influence of bacterial extracellular polymers on the membrane separation activated sludge process,. *Water Sci. Technol.*, 34(9):165–172, 1996.

[48] B-K Hwang, W-N Lee, K-Y Yeon, P-K Park, C-H Lee, I-S Chang, A Drews, and M Kraume. Correlating tmp increases with microbial characteristics in the bio-cake on the membrane surface in a membrane bioreactor. *Environmental Science and Technology*, 42:3963–3968, 2008.

[49] A. L. Lim and Renbi Bai. Membrane fouling and cleaning in microfiltration of activated sludge wastewater. *Journal of Membrane Science*, 216:279–290, 2003.

[50] B. Van der Bruggen, L. Braeken, and C. Vandecasteele. Flux decline in nanofiltration due to adsorption of organic compounds. *Separation and Purification Technology*, 29:23–31, 2002.

[51] V. G. J. Rodgers and R. E. Sparks. Effect of transmembrane pressure pulsing on concentration polarization. *Journal of Membrane Science*, 68:149–168, 1992.

[52] Tatsuki Ueda, Kenji Hata, Yasuto Kikuoka, and Osamu Seino. Effects of aeration on suction pressure in a submerged membrane bioreactor. *Water Research*, 31:489–494, 1997.

[53] M.R. Wiesner and S. Chellam. The promise of membrane technologies. *Environ. Sci. Technol.*, 33(17):360A–366A, 1999.

[54] J. A. Howell, R. W. Field, and D. Wu. Yeast cell microfiltration: flux enhancement in baffled and pulsatile flow system. *Journal of Membrane Science*, 80:59–71, 1993.

[55] B. B. Gupta, J. A. Howell, D. Wu, and R. W. Field. A helical baffle for cross-flow microfiltration. *Journal of Membrane Science*, 99:31–42, 1995.

[56] F. Li, W. Meindersma, A. B. de Haan, and T. Reith. Optimization of commercial net spacers in spiral wound membrane modules. *Journal of Membrane Science*, 208:289–302, 2003.

[57] S. Chang and A. Fane. Characteristics of microfiltration of suspensions with inter-fiber two-phase flow. *J. Chem. Technol. Biotechnol.*, 75:533–540, 2000.

[58] S. R. Bellara, Z. F. Cui, and D. S. Pepper. Gas sparging to enhance permeate flux in ultrafiltration using hollow fibre membranes. *Journal of Membrane Science*, 121:175–184, 1996.

[59] C. Cabassud, S. Laboriea, L. Durand-Bourlierb, and J. M. Lain. Air sparging in ultrafiltration hollow fibers: relationship between flux enhancement, cake characteristics and hydrodynamic parameters. *Journal of Membrane Science*, 181:57–69, 2001.

[60] Z. F. Cui and K. I. T. Wright. Flux enhancements with gas sparging in downwards crossflow ultrafiltration: performance and mechanism. *Journal of Membrane Science*, 117:109–116, 1996.

[61] M. Mercier, C. Fonade, and C. Lafforgue-Delorme. How slug flow can enhance the ultrafiltration flux in mineral tubular membranes. *Journal of Membrane Science*, 128:103–113, 1997.

[62] M. Mercier, C. Fonade, and C. Lafforgue-Delorme. Influence of the flow regime on the efficiency of a gas-liquid two-phase flow medium. *Biotechnology Techniques*, 9:853–858, 1995.

[63] J. Fabre and A. Line. Modelling two–phase slug flow. *Ann. Rev. Fluid Mech.*, 24:21–46, 1992.

[64] M. E. Weber, A. Alarie, and M. E. Ryan. Velocities of extended bubbles in inclined tubes. *Chemical Engineering Science*, 41(9):2235–2240, 1986.

[65] P. L. Spedding and V. T. Nguyen. Bubble rise and liquid content in horizontal and inclined tubes. *Chemical Engineering Science*, 33:987–994, 1978.

[66] Q. Y. Li, Z. F. Cui, and D. S. Pepper. Effect of bubble size and frequency on the permeate flux of gas sparged ultrafiltration with tubular membranes. *Journal of Membrane Science*, 67:71–75, 1997.

[67] Q. Y. Li, R. Ghosh, S. R. Bellara, Z. F. Cui, and D. S. Pepper. Enhancement of ultrafiltration by gas sparging with flat sheet membrane modules. *Separation and Purification Technology*, 14:79–83, 1998.

[68] R. M. Davies and G. Taylor. The mechanics of large bubbles rising through extended liquids and through liquids in tubes. *Proc. Roy. Soc.*, 200:375, 1950.

[69] J. H. C. Coppus, K. Rietema, and S. P. P. Ottengraf. Wake phenomena behind spherical-cap bubbles and spherical-cap bodies. *Trans. I. Chem. E.*, 55:122–129, 1977.

[70] J. H. Hills. The two-dimensional elliptical cap bubble. *J. Fluid Mech.*, 68:503–512, 1975.

[71] L. S. Fan and K. Tsuchiya. *Bubble wake dynamics in liquids and liquid–solid suspensions*. Butterworth–Heinemann, Boston, 1990.

[72] K. Lunde and J. Perkins. A method for the detailed study of bubble motion and deformation. *Advances in Multiphase Flow*, 1995.

[73] R. Lindken and W. Merzkirch. A novel piv technique for measurements in multiphase flows and its application to two-phase bubbly flows. *Experiments in Fluids*, 33(6):814–825, 2002.

[74] A. Tokuhiroa, M. Maekawab, K. Iizukab, K. Hishidab, and M. Maedab. Turbulent flow past a bubble and an ellipsoid using shadow-image and piv techniques. *International Journal of Multiphase Flow*, 24:1383–1406, 1998.

[75] N. V. Ndinisa and A. G. Fane D. E. Wiley. Fouling control in a submerged flat sheet membrane system: Part i - bubbling and hydrodynamic effects. *Separation Science and Technology*, 41(7):1383–1409, 2006.

[76] N. V. Ndinisa, A. G. Fane D. E. Wiley, and D. F. Fletcher. Fouling control in a submerged flat sheet membrane system: Part ii - two-phase flow characterization and cfd simulations. *Separation Science and Technology*, 41(7):1411–1445, 2006.

[77] P. J. Roache. *Computational Fluid Dynamics*. Albuquerque: Hermosa, 1976.

[78] R. Krishna and J. M. van Baten. Rise characteristics of gas bubbles in 2d rectangular columns: Vof simulations vs experiments. *Int. Comm. Heat Mass Transfer*, 26(7):965–974, 1999.

[79] P. R. Spalart. Strategies for turbulence modeling and simulations. *Int. J. Heat Fluid Flow*, 21:252–263, 2000.

[80] C. N. Lim, M. A. Gilbertson, and A. J. L. Harrison. Bubble distribution and behaviour in bubbling fluidised beds. *Chemical Engineering Science*, 62:56–69, 2007.

[81] C. N. Lim, M. A. Gilbertson, and A. J. L. Harrison. Measurement and simulation of bubbling fluidised beds. *Powder Technology*, 170:167–177, 2006.

[82] A. J. Croxford and M. A. Gilbertson. Control of the state of a bubbling fluidised bed. *Chemical Engineering Science*, 61:6302–6315, 2006.

[83] J. T. Edward. Molecular volumes and the stokes-einstein equation. *J. Chem. Ed.*, 47(4):261–270, 1970.

[84] S. Chellam and M. R. Weisner. A first principles approach towards understanding concentration polarization. pages 675–689. AWWA, 1991.

[85] A. S. Berman. Laminar flow in channels with porous walls. *Journal of Applied Physics*, 24(9):1232–1235, 1953.

[86] Fluent Incorporated, Lebanon, New Hampshire. *FLUENT 6.1 Users Guide*, 2003.

[87] C. W. Hirt and B. D. Nichols. Volume of fluid (vof) method for the dynamics of free boundaries. *Journal of Computational Physics*, 39:201–225, 1981.

[88] D. L. Youngs. *Time-dependent multi-material flow with large fluid distortion*. Academic Press, New York, 1982.

[89] W. F. Noh and P. R. Woodward. Slic (simple line interface method). *Lecture Notes in Physics*, 59:330–340, 1976.

[90] William J. Rider and Douglas B. Kothe. Reconstructing volume tracking. *J. Comput. Phys.*, 141(2):112–152, 1998.

[91] J. U. Brackbill, D. B. Kothe, and C. Zemach. A continuum method for modeling surface tension. *Journal of Computational Physics*, 100:335–354, 1992.

[92] Eiichi Kojima, Takashi Akehata, and Takashi Shirai. Behavior of single air bubbles held stationary in downward flows. *Journal of Chemical Engineering of Japan*, 8(2):108–113, 1975.

[93] G. B. Wallis. *One-dimensional two-phase flow*. McGraw-Hill, New York, 1969.

[94] J. G. Hnat and J. D. Buckmaster. Spherical cap bubbles and skirt formation. *The Physics of Fluids*, 19(2):182–194, 1976.

[95] J. M. Boulton-Stone, P. B. Robinson, and J. R. Blake. A note on the axisymmetric interaction of pairs of rising, deforming gas bubbles. *Journal of Multiphase Flow*, 21:1237–1241, 1995.

[96] S. Polonsky, L. Shemer, and D. Barnea. The relation between the taylor bubble motion and the velocity field ahead of it. *International Journal of Multiphase Flow*, 25:957–975, 1999.

[97] D. T. Dumitrescu. Stromung an einer luftblase im senkrechten rohr. *Z. Angew. Math. Mech.*, 23:139–149, 1943.

[98] R. Collins. A simple model of the plane gas bubble in a finite liquid. *Journal of Fluid Mechanics*, 22:763–771, 1965.

[99] G. Ducom, F. P. Puech, and C. Cabassud. Air sparging with flat sheet nanofiltration: a link between wall shear stresses and flux enhancement. *Desalination*, 145:97–102, 2002.

[100] L. P. Reiss and T. J. Hanratty. Measurement of instantaneous rates of mass transfer to a small sink on a wall. *A. I. Ch. E. Journal*, 8(2):245–247, 1962.

[101] G. Cognet, M. Lebouche, and M. Souhar. Wall shear measurements by electrochemical probe for gas-liquid two-phase flow in vertical duct. *A. I. Ch. E. Journal*, 30(2):338–341, 1984.

[102] A. Drews, H. Prieske, E-L. Meyer, G. Senger, and M. Kraume. Advantageous and detrimental effects of air sparging in membrane filtration: Bubble movement, exerted shear and particle classification. *Desalination*, 250:1083–1086, 2010.